

**NASA CONTRACTOR
REPORT**



NASA CR-

C.1

0099834



TECH LIBRARY KAFB, NM

NASA CR-714

**FURTHER EXPERIMENTAL INVESTIGATIONS
OF DELTA AND DOUBLE-DELTA WING
FLOW FIELDS AT LOW SPEEDS**

by William H. Wentz, Jr., and Michael C. McMahon

Prepared by

WICHITA STATE UNIVERSITY

Wichita, Kans.

for



FURTHER EXPERIMENTAL INVESTIGATIONS OF DELTA
AND DOUBLE-DELTA WING FLOW FIELDS
AT LOW SPEEDS

By William H. Wentz, Jr., and Michael C. McMahon

Distribution of this report is provided in the interest of
information exchange. Responsibility for the contents
resides in the author or organization that prepared it.

Prepared under Grant No. NGR 17-003-003 by
WICHITA STATE UNIVERSITY
Wichita, Kans.

for

NATIONAL AERONAUTICS AND SPACE ADMINISTRATION

SUMMARY

Low speed wind tunnel investigations were conducted to determine the nature of the flow fields about delta and double-delta wings at low speeds and their relationship to aerodynamic forces. A semi-span double-delta model consisting of a forward panel having an 80° swept leading edge and a 62° swept main panel was tested at a Reynolds number per foot of 1.0×10^6 . Detailed velocity vector measurements were made in the flow fields around the wing. Results are compared with flow field measurements about a 62° delta and a $75^\circ/62^\circ$ double-delta wing, some of which were reported previously. Three-component force data, pressure distributions, and surface-tuft and oil-streak patterns are presented. Leading edge vortex sheet measurements are presented and compared with free streamline theory. Circulation integrals derived from the flow field maps are presented.

Results indicate that vortex core breakdown is the source of the principal discrepancy between measured and theoretical lift. The lift prediction method of Poisson-Quinton accounts for the breakdown and seems to be the most satisfactory method of lift prediction available presently. Better definition of vortex core breakdown boundaries for non-delta slender wings and the effects of breakdown on lift will be required before lifting prediction for slender sharp-edged wings is entirely satisfactory.

SYMBOLS

A	aspect ratio, $\frac{(\text{span})^2}{(\text{wing area})}$
a	wing semi-span at any chordwise station x
b	wing maximum semi-span
c	wing chord
\bar{c}	wing mean geometric chord, $\frac{\int_0^b c^2 dy}{\int_0^b c dy}$
C_L	lift coefficient, $\frac{L}{qS}$
C_{L_α}	lift curve slope, $dC_L/d\alpha$ (per degree)
C_D	drag coefficient, $\frac{D}{qS}$
C_M	pitching moment coefficient, $\frac{M}{qS\bar{c}}$
C_N	normal force coefficient, $\frac{N}{qS}$
C_p	pressure coefficient, $\frac{p-p_\infty}{q}$
D	drag force
L	lift force
l	length
M	pitching moment
N	normal force
p	pressure
q	dynamic pressure, $\frac{1}{2}\rho V_\infty^2$
S	wing area
t	time
V	velocity

x	coordinate in chordwise direction
x'	coordinate in streamwise direction
y	coordinate in spanwise direction
z	coordinate perpendicular to wing chord plane
z'	coordinate perpendicular to free stream direction
α	angle of attack
Δ	increment
Γ	circulation
γ	vortex sheet strength per unit length, $d\Gamma/dx$
ρ	air density

SUBSCRIPTS

∞	free stream conditions
0	remote conditions in cross-flow plane
1	position outside vortex sheet
2	position inside vortex sheet
s	pertaining to vortex sheet
62	pertaining to 62° delta wing
i	induced
v	pertaining to vortex

SUPERSCRIPTS

-	denotes vector
---	----------------

INTRODUCTION

One of the current disparities in low speed aerodynamics is that between the theoretical and the measured force characteristics of slender wings at high angles of attack. Linearized lifting theories such as DeYoung and Harper (ref. 1) have been developed to a high degree to treat arbitrary planforms at small angles. These theories are inherently restricted to unseparated flows and cannot, therefore, account for the leading edge vortex systems generated by sharp-edged delta wings at high angles of attack. Various theories for predicting the non-linear lift associated with a separated leading edge vortex system (ref. 2, 3) have not yet approached the degree of precision attained for unseparated flows.

Recent designs for a supersonic transport aircraft have incorporated multiple sweep or double-delta type planforms. The advent of these designs has generated renewed interest in leading edge vortex phenomena and in possible interactions between the vortex systems associated with the various panels.

The present investigation was undertaken as an experimental project to determine the actual flow patterns associated with a sharp-edged delta so that discrepancies between the mathematical and physical models might be isolated. A further purpose was to explore carefully the influence of leading edge strakes (or double-delta panels)

on the basic delta wing flow fields to gain an appreciation of possible interactions between the vortex systems of the strake and of the main wing panel.

Results of flow field investigations about a delta wing having 62° sweep and a double-delta wing having 75° and 62° swept panels have been reported in reference 4. The present report includes the results of flow field measurements using an $80^\circ/62^\circ$ double-delta wing as well as some additional flow field measurements about the $75^\circ/62^\circ$ double-delta and 62° delta wings. Comparisons of all three configurations are presented. Experimental circulation integral results for the three wings are presented and discussed. Leading-edge vortex sheet measurements for the three sweep angles are also included and compared with free streamline theory.

WIND TUNNEL MODELS AND INSTRUMENTATION

MODELS

Three half-models consisting of wing and fuselage were tested (figs. 1a, 1b, 1c): a 62° delta configuration, a $75^\circ/62^\circ$ double-delta and an $80^\circ/62^\circ$ double-delta. The basic delta has a 62° leading edge sweep, straight trailing edge, and the wing tip is cropped slightly. Wing sections of the basic delta are biconvex with a maximum thickness of 2.5% of the chord. The resultant leading and trailing edges are sharp, each having angles of only 6° . The wings have no camber or twist.

The double-delta wings are derived from the basic wing by the addition of inboard strakes which fair into the basic wing contours at the 50% root chord location. All wing panels were machined from solid aluminum plate. All three wing configurations utilize the same aft panel. The fuselage is a simple body of revolution constructed of mahogany. Wings are mounted $1/4$ diameter below the fuselage centerline. The wing-fuselage juncture was sealed without a fillet.

The semi-span models were installed vertically on a 10- by 10-ft reflection plane which was mounted 3 inches above the wind tunnel floor in order to minimize reflection plane boundary layer. During force data runs, clearance between the reflection plane and fuselage centerline

was maintained at 0.05 inch to minimize leakage and to eliminate mechanical interference. During flow field runs the gap was sealed.

INSTRUMENTATION

Flow field velocity vectors were obtained using the five-tube velocity probe developed during the first phase of this research. This probe (fig. 3c) is mounted on a stand with provisions for remote control of rotation about one axis and linear positioning perpendicular to the wing (z-direction). (Note: coordinate system is shown in figure 2) The stand permits the manual positioning of the probe in a plane parallel to the wing (x-y plane). Through calibration data the probe system makes possible the determination of all three components of an unknown velocity vector for a range of sidewash angles of $\pm 180^\circ$ and upwash angles of $\pm 45^\circ$. Overall accuracies are estimated to be $\pm 2^\circ$ for upwash and sidewash angles and $\pm 2\%$ for velocity. Data were recorded directly onto punch cards, and data reduction was carried out on an IBM 1620 computer.

A special velocity probe was constructed for detailed surveys of the leading edge vortex sheet. This probe (fig. 3d) utilized the same type five-hole tip used for other velocity field measurements. The stem was shortened, however, so that the overall probe length was only 2.5

inches. This modification was necessary in order to mount the probe on the very short span of the 80° strake. Because of these space limitations, the probe rotation motor could not be used, and it was necessary to manually rotate the probe into the local flow plane for each measurement.

TESTS AND CORRECTIONS

Testing was conducted in the Wichita State University 7- by 10-ft wind tunnel, a low speed, closed circuit facility. Testing was conducted at a dynamic pressure of 40 psf which corresponds to a Reynolds number per foot of 1.0×10^6 .

Lift, drag, and pitching moment data were obtained from all models utilizing the tunnel main balance system. Since this information is utilized primarily in conjunction with measured pressure and flow field data, jet boundary corrections were not applied to the bulk of the force data. The following boundary correction was applied to the data presented in figures 6 and 7 which compare measured forces with results from other tests, and with theory:

$$\Delta\alpha_i = 0.756 C_L \text{ (degrees)}$$

This correction was also applied to the theoretical induced drag data ($C_{D_i} = C_L \tan \alpha$) as indicated in figure 7e. The blockage correction was negligible.

Upper surface static pressure distributions were obtained at angles of attack from -10° to +40° in 5°

increments. Upper surface tuft and oil streak patterns were obtained at the same angles.

Flow field upper surface velocity distributions were obtained at 5° , 10° , and 20° angles of attack, using the five-tube probe. The 5° and 10° angles were selected to bracket the angle of attack at which strake and aft panel vortex systems interact. (See page 11 for a discussion of this phenomenon.) The 20° angle was selected as being a practical upper limit from the standpoint of landing gear design.

Additional leading edge flow field measurements were made at one station on each wing panel to determine the detailed structure of the leading edge vortex sheet. These measurements were made at angles of attack from 0° to 40° in 5° increments using a modified five-tube probe.

DISCUSSION OF TEST RESULTS

FORCE CHARACTERISTICS

Conventional aerodynamic force coefficient data for the $80^\circ/62^\circ$ double-delta wing are shown in figures 4a, 4b, and 4c. This wing exhibits a sharp step or "kink" in the C_L vs. α curve (fig. 4a) that did not appear with either the 62° delta or $75^\circ/62^\circ$ double-delta wing. This kink was first observed in the range of 22° to 24° angle of attack. Data taken at one degree increments in angle of attack confirmed the trend, and an additional run with dynamic

pressure reduced by one-half produced identical coefficients. Increasing and decreasing angle of attack series established that hysteresis was not present. The kink is also clearly shown in the drag data (fig. 4b), but surprisingly, does not appear in the pitching moment data (fig. 4c).

COMPARISONS WITH OTHER TEST RESULTS

In order to compare force measurements of double-delta wings having various size strake (forward) panels, it is necessary to refer all coefficients to a common reference area. According to Jones' theory (ref. 5), the lift developed by a slender wing or body is dependent only upon the maximum span and is independent of planform area. If the maximum span is selected as the characteristic dimension, the non-dimensional coefficient will be $\frac{L}{q(\text{span})^2}$ which is exactly equal to C_L/A . The corresponding drag parameter is C_D/A and the pitching moment parameter is $\frac{C_M \bar{c}}{A \bar{c}_{62}}$

The data in this form are compared with the 62° delta and 75°/62° double-delta in figures 5a, 5b, and 5c. Figure 5a shows that all wings have the same lift curve slope up to 7° or 8°, confirming Jones' theory. At large angles the double-delta wings begin to develop more lift. The 80°/62° wing appears to drop from almost the same lift level as the 75°/62° wing to slightly more lift than the

62° wing at the critical angle of attack of 22°. The drag polar for the 80°/62° double-delta shows the kink clearly as a sharp increase in drag level for a given lift, shifting from approximately that of the 75°/62° curve to nearly match the 62° delta wing polar.

The pitching characteristics of the three wings are compared in figure 5c. For this purpose all data have been referred to a common area (span^2) and a common chord (\bar{c}_{62}), as noted above. In addition, all configurations have the pitching moments referred to a point which gives them the same stability level at zero lift. Again, the 62° delta is taken as a baseline. As strake area is added, the wings experience an increasing nose up pitching moment (pitch-up) at high angles of attack. The 80°/62° double-delta has values of pitching moment between the 62° delta and the 75°/62° double-delta but no distinct kink or break point appears.

A comparison of the 80°/62° double-delta with an 83°/65° double-delta wing (from ref. 15) is presented in figure 6a, 6b, and 6c. The lift curves show more non-linear lift for the 83°/65° wing, but this wing exhibits a similar kink in the curve at the same effective angle of attack. Note that the 83°/65° wing curve has been corrected for camber by shifting to the same angle of zero lift as the 80°/62° wing. The drag polar for the

83°/65° wing (fig. 6b) does not extend to angles of attack large enough to show the kink. Comparison of pitching moment data (fig. 6c) shows that the 83°/65° wing has greatly delayed pitch-up characteristics. This delay may be due to the forward sweep of the trailing edge on this wing.

COMPARISONS WITH THEORY

Normal force developed by the 80°/62° wing is compared with that predicted by the theories of Jones (ref. 5), Brown and Michael (ref. 2), Mangler and Smith (ref. 3), and Poisson-Quinton (ref. 6) in figure 7a. These theories (except Jones) predict considerably more non-linear lift than was obtained experimentally. A more detailed comparison of the Poisson-Quinton theory with experimental results is presented in figures 7b, 7c, and 7d. Here the Poisson-Quinton theory has been used to generate theoretical lift curve slope (C_{L_α}) characteristic curves for the three wings tested.

Poisson-Quinton has suggested that maximum non-linear lift is reached when C_{L_α} reaches a value of 0.05 per degree, as shown in the figures. All three wings tested attained maximum C_{L_α} values greater than 0.05, but none exceeded 0.06. The shapes of the experimental C_{L_α} curves roughly correspond to the C_{L_α} curves obtained by the Poisson-Quinton method, but further refinement appears to

be required before accurate lift predictions are obtained. Poisson-Quinton introduces an experimental coefficient to make the final match between theory and experiment. This is illustrated by the equation given by Poisson-Quinton:

$$C_{L\alpha} = k \frac{4.9}{4.9+A} \left[\frac{\pi A}{2} \alpha + \pi A^{1/3} \alpha^{5/3} \right]$$

This equation is restricted to the range of angles of attack for which $C_{L\alpha}$ is less than 0.05, as noted above. The empirical coefficient k is described as being a function of thickness, airfoil section, etc., and as having a magnitude less than unity. In one example given by Poisson-Quinton, k was 0.915. Unfortunately, a rational method for estimating k is apparently not yet available.

The drag data (fig. 7d) shows excellent agreement with $C_{D_i} = C_L \tan \alpha$, demonstrating the lack of leading edge suction with sharp leading edges. Drag polar comparisons of the three wings tested show that the strakes improve the lift-drag ratio at higher angles of attack. This result is a direct consequence of the improved C_L vs. α characteristics previously described.

PRESSURE DISTRIBUTIONS

Upper surface static pressure distributions for the 80°/62° wing are shown in figures 8a through 8i. Lower surface pressures were not measured, as they are known to

be relatively uniform for wings of this type. (See figure 8j.) At 0° angle of attack, the pressure distribution reflects only the thickness distribution of the wing. At 5° angle of attack, two negative pressure ridges are present indicating two distinct vortices; one streams aft from the strake, and the second follows the edge of the main wing panel. At angles from 10° to 40° only a single ridge is present, indicating the presence of a single vortex over the aft panel. These same trends were observed with the $75^\circ/62^\circ$ double-delta wing, as reported in reference 4.

At 15° angle of attack, a valley or wedge of increased pressure appears to propagate forward from the trailing edge, just outboard of the minimum pressure ridge. At 25° this wedge has moved forward nearly to the strake, and at higher angles of attack pressure distributions are characterized as having a broad, rounded minimum rather than the sharp crested peaks present at lower angles. The magnitudes of the peaks are actually reduced as the angle of attack is increased above 30° .

Figure 8j shows the effects of strake area on wing pressure distributions.

OIL STREAK AND TUFT PATTERNS

The oil streak patterns for the $80^\circ/62^\circ$ wing at all angles of attack clearly mark the secondary separation line which occurs just outboard of the upper surface vortex

characteristic of delta wing flow fields. Tuft patterns show the vortex position and size as the region of tufts having strong spanwise components. Figures 9b and 9c show the double vortex pattern which is also apparent in the pressure and flow field maps at 5° angle of attack. A streak photo at $6\frac{1}{2}^\circ$ shows the interaction of strake and aft panel vortex systems progressing forward from the trailing edge. At angles above 7° the strake and aft panel vortices roll together in the immediate vicinity of the strake and aft panel juncture.

At moderate angles of attack, the flow in the region outboard of the secondary separation line is apparently steady, and in a direction essentially parallel to the leading edge. At 20° angle of attack both the oil streak and tuft photos (figures 9n and 9o) show an unsteady reversed flow region near the wing tip. This region appears in the pressure data as a wedge propagating forward from the trailing edge.

At 25° angle of attack both the streak and tuft photos indicate a considerable increase in effective vortex diameter. The secondary separation line has apparently moved outboard, but there is a great deal of unsteadiness evident in the patterns. At higher angles this unsteadiness progressively increases.

VELOCITY FIELD MAPS

Velocity field maps in the cross-flow (y-z) plane for the $80^\circ/62^\circ$ double-delta wing are shown in figures 10a

through 12f. These measurements include four stations over the wing and two stations aft of the trailing edge at angles of attack of 5° , 10° , and 20° . Similar data from the 62° delta wing and $75^\circ/62^\circ$ double-delta wing are shown in figures 13a through 17e. These maps include the data from reference 4 with additional new measurements beyond the wing tip and new measurements behind the trailing edge. For stations behind the trailing edge, components have been resolved using a co-ordinate system perpendicular to the free stream (y-z' plane) rather than perpendicular to the wing chord plane. This system is more appropriate since the vortex behind the wing assumes a nearly stream-wise direction.

At 5° angle of attack, the flow field is characterized by an outboard panel elongated vortex and a separate distinct aft panel vortex. At higher angles of attack only a single vortex is present. These same characteristics were previously observed on the $75^\circ/62^\circ$ double-delta wing (ref. 4).

Close comparison of the $80^\circ/62^\circ$ wing flow field near the trailing edge at a high angle of attack condition ($x/b = 0.027$, $\alpha = 20^\circ$, fig. 12d) with corresponding flow field maps for the 62° (fig. 15c) and $75^\circ/62^\circ$ (fig. 17c) wings illustrates some interesting features of the flow fields. The primary vortex locations are quite similar for the three wings. The secondary reversed vortex observed by previous investigators (refs. 7 and 8) is

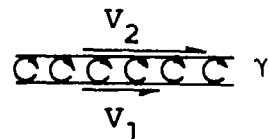
visible on all three wings. Velocity directions are very similar for the wings although the magnitudes increase with addition of strake area. A more detailed comparison of vortex locations and magnitudes is given in the section of this report entitled "CIRCULATION."

LEADING EDGE VORTICITY

BACKGROUND AND THEORY

One of the most promising of the techniques for calculating the characteristics of arbitrary wings with separated leading edges is that developed by Sacks, Neilsen, and Goodwin (ref. 9). This method involves assuming that discrete vortex filaments are shed along the leading edge of highly swept planforms. Calculations of the trajectories of these filaments have shown rollup patterns similar to those observed from experimental smoke patterns. As the number of vortex filaments is increased, the array approaches a continuous vortex sheet. The strength or magnitude of the vortex sheet may be measured as the vorticity shed per unit time. An analytic technique for calculating the vorticity shed per unit time is given by the free streamline method applied to a thin two-dimensional flat plate normal to the stream (Kirchoff flow).

For a simple vortex sheet (infinitely thin velocity discontinuity), the vortex sheet strength is the vorticity per unit length:

$$\gamma = \frac{d\Gamma}{d\ell}$$


The vorticity shed per unit time is given by:

$$\frac{d\Gamma}{d\ell} = \gamma = v_2 - v_1$$

and

$$v_s = \frac{v_2 + v_1}{2}$$

therefore;

$$\frac{d\Gamma}{dt} = \frac{v_2^2 - v_1^2}{2}$$

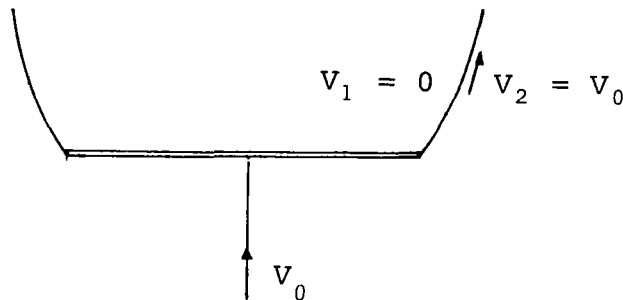
In non-dimensional form:

$$\text{Eq. (1)} \quad \frac{1}{v_\infty^2} \frac{d\Gamma}{dt} = \frac{(v_2/v_\infty)^2 - (v_1/v_\infty)^2}{2}$$

Vorticity generated per unit time by a thin vortex sheet.

FREE STREAMLINE THEORY

Consider the flow normal to a thin flat plate:



From free streamline theory, the velocity just outside the free streamline is equal to the remote velocity.

The velocity inside the region bounded by the free streamline is zero. Thus the vorticity per unit time becomes

$$\frac{d\Gamma}{dt} = \frac{v_0^2}{2}$$

For the case of the cross flow past a thin sharp-edged wing, v_0 is the normal component of the free stream velocity,

$V_{\infty} \sin \alpha$:

$$\frac{d\Gamma}{dt} = \frac{V_{\infty}^2 \sin^2 \alpha}{2}$$

In non-dimensional form:

Eq. (2) $\frac{1}{V_{\infty}^2} \frac{d\Gamma}{dt} = \frac{\sin^2 \alpha}{2}$

EXPERIMENTAL MEASUREMENTS

Measurements of the leading edge vorticity generation rate were made using a specially constructed velocity probe attached directly to the upper surface of the wing panels. Measurements were made at one position on each wing panel so that data were obtained for the three sweep angles of 62°, 75°, and 80°. Data were obtained from 0.5 inch inboard from the leading edge to 1.0 inch beyond the leading edge at 0.25 inch intervals in order to span the complete vortex sheet. Vorticity rates were calculated using equation (1) above. These results (fig. 18) show some lack of consistency. It is believed that smaller measurement intervals across the vortex sheet would improve the quality. For example, V_s could be determined from a velocity profile integration rather than as a simple average. The results do clearly show that the experimental vorticity rates are much larger than predicted by simple free streamline theory. This was demonstrated some years ago by the measurements of Fage and Johansen (refs. 10 and 11) for a

flat plate perpendicular to the stream. The Fage and Johansen data point is included in figure 18 for reference. An interesting feature of the present data is that all three panels demonstrated a maximum vorticity rate at angles between 25° and 30°. These angles correspond to the range of angles of attack at which the lift forces were maximum. It would appear that there is a maximum or stalling value of vortex sheet strength. Flow conditions near the tip, however, are most certainly influenced by the primary vortex position and strength, so that the reduction in vortex sheet strength may be merely a result of a change in the primary vortex. The primary vortex, on the other hand, is made up of the coiled up vortex sheet generated at the leading edge. These arguments lead to a "chicken versus egg" dilemma. The question as to whether the vortex sheet or the wing "stalls" first remains unanswered for the present.

CIRCULATION

THEORY

The lift generated by an aerodynamic lifting surface is related to the circulation by the classical Kutta-Joukowski Law

$$L = \rho V_{\infty} \Gamma b_v$$

where Γ is circulation and b_v is the vortex span. Since delta wings generally have not developed theoretical lift values, it is of interest to examine the circulation actually developed by delta-type wings and to compare this information

with the circulation information in readily discernible form: the theories of Jones and of Brown and Michael.

Jones' theory (ref. 5) predicts only the linear lift which would appear with unseparated leading edges. For this theory the non-dimensional circulation is given by

$$\frac{\Gamma}{2aV_{\infty}} = \sin \alpha$$

where a is the local semi-span. If the circulation is referred to the wing maximum span, the equation becomes

$$\frac{\Gamma}{2bV_{\infty}} = \frac{a}{b} \sin \alpha$$

Using this relationship, the $\frac{\Gamma}{2bV}$ distributions can be developed for any slender planform. This was the technique used to generate the lines labeled "Jones" in figures 19a through 19e.

Brown and Michael (ref. 2) present a universal relationship for non-dimensional circulation of simple deltas as a function of sweep angle and angle of attack:

$$\frac{\Gamma}{2bV_{\infty}} = f(\alpha, \Lambda)$$

This relationship was used to generate the lines labeled "Brown and Michael" in figures 19a through 19e.

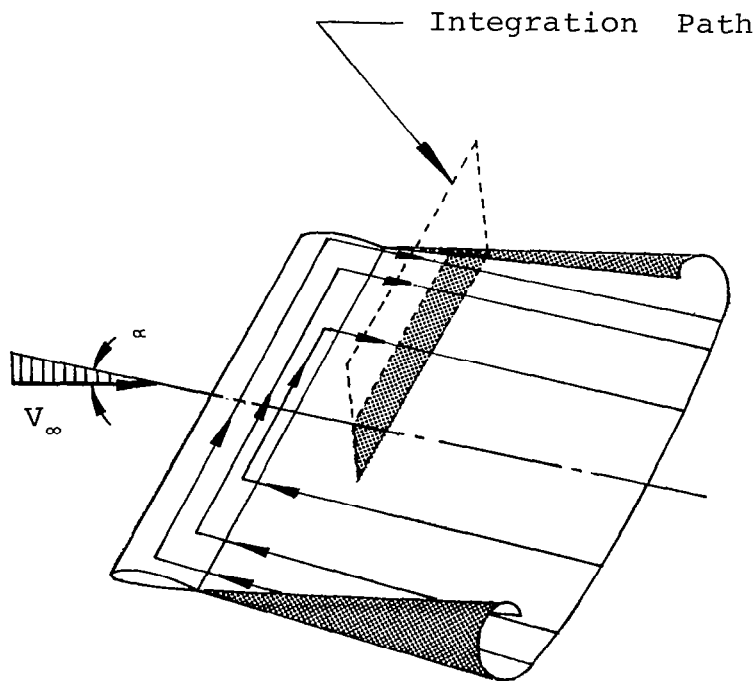
EFFECT OF FUSELAGE

The forebody of the fuselage used with each wing was assumed to generate the same total circulation as an equal span of extended delta would have given in each case. This method of analysis results in the fuselage forebody being charged with different amounts of

circulation, depending upon the wing configuration. Spreiter (ref. 16) has shown that the effect of the body on total wing lift is less than 3% for a body radius to maximum semi-span ratio of 0.10. This value indicates that the approach described above should not introduce serious errors.

INTEGRATION PATHS

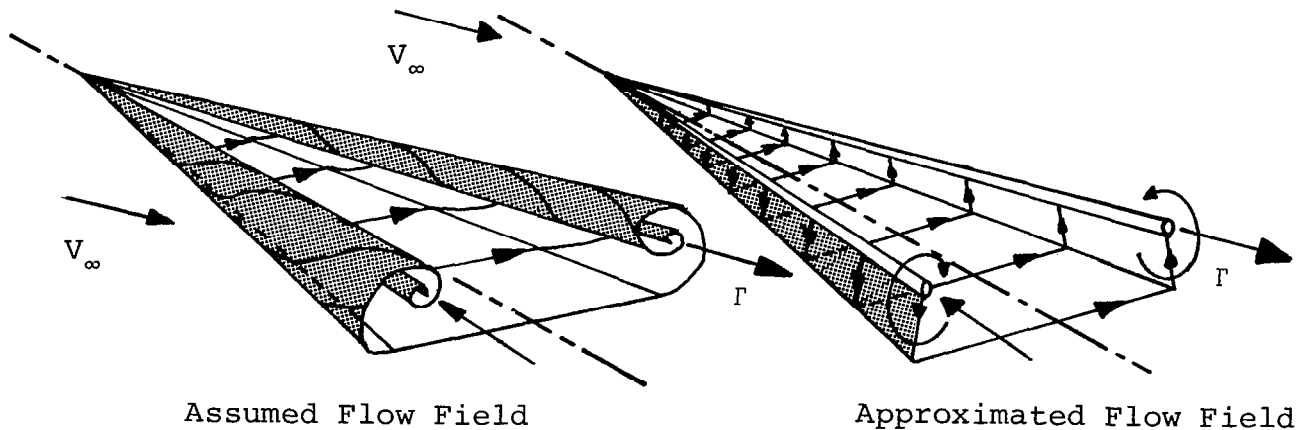
In obtaining experimental circulation integrals, the question arises as to an appropriate path around which to integrate. For moderate to high aspect ratio wings, the circulation distribution approaches that predicted by Prandtl; the path might be one of relatively small vertical height--only a small fraction of a chord above the trailing edge and extending a similar distance below the trailing edge, as indicated below.



Since chordwise growth of circulation is small, the

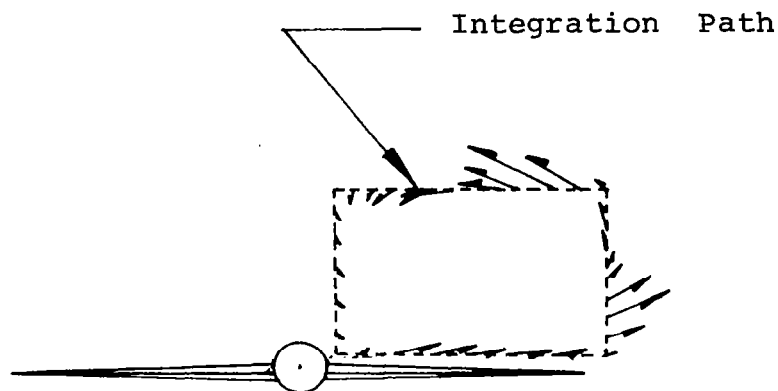
integration path would probably be taken behind the trailing edge.

The mathematical model of Brown and Michael illustrates the circulation distribution associated with slender delta wings.



Since the circulation variation here is principally in the chordwise direction, it is appropriate to choose paths at several chordwise stations. Further, it is not necessary to include the wing chord plane within the integration path. Since the shed vorticity lies above the wing upper surface, it is important to select a path of sufficient height to enclose the apparent center of the vortex with some allowance for portions of the coiled up vortex sheet which might lie above the center. It is also important that the path extend beyond the local wing tip in order to include the portion of the vortex sheet which moves outboard as it is shed from the edge.

This point was not appreciated fully during the initial testing, as reported in reference 4, and flow field measurements were not taken beyond the local wing tip. In the present investigation, measurements beyond the wing tip are included. The sketch below indicates a typical integration path:



Integration Path For Delta Wings

METHOD OF CALCULATING CIRCULATION

Circulation values were obtained from velocity field measurements by performing line integrals of the form:

$$\Gamma = \oint_l \vec{v} \cdot d\vec{l}$$

along the paths chosen. Rectangular paths were selected in each case to simplify the calculation procedure.

Integrals were obtained by measuring areas under faired curves of velocity component versus distance rather than simply averaging velocity components over an interval.

Circulation values could also be obtained by using Stokes Theorem which relates line integral around a path

to area integral of the curl:

$$\oint_{\lambda} \bar{v} \cdot d\bar{l} = \int_A (\nabla \times \bar{v}) \cdot d\bar{A}$$

Determining curl distributions from the velocity maps would require differentiation (taking slopes) of the experimental results and this would probably lead to considerable inaccuracy as well as being very laborious.

From a standpoint of determining vortex sheet coil-up patterns, as well as vortex sheet strength, it would be desirable to measure the vorticity or curl field directly. Such measurements could be made with a vorticity meter, suitably calibrated. Preliminary design of a non-rotating vorticity meter was carried out as a Master of Science thesis project by McMahon, and the results are reported by Snyder in reference 12.

EXPERIMENTAL RESULTS

Experimental circulation values by the present method are shown in figures 19a through 19e. The data points labeled "largest path" refer to the value of circulation obtained by integrating through the points on the extremities of the appropriate flow field map. At aft positions on the wings, a secondary reversed vortex appears at the higher angles of attack. Circulation integrals around the "largest path" included these regions. If the region of the secondary vortex is not included, a greater value of circulation may be calculated. This is the

technique which was used to obtain the values labeled "maximum Γ ". The incremental circulation between the points labeled "largest path" and "maximum Γ " represents the magnitude of this secondary vortex. The "largest path" circulation is the value related to net lift in every case.

It is seen that virtually all measured circulation values lie between the Jones and the Brown and Michael theories, as do the measured normal forces (figure 7a). The theoretically predicted increase of circulation with span is generally confirmed. The secondary vortex, which is not included in any present wing theory, is seen to cause a significant reduction in net circulation and, therefore, net lift.

Vortex core center locations, as determined from the velocity field maps, are presented in figures 20a, 20b, and 20c. At 5° angle of attack the vortex sheet pattern mentioned previously appears over the main wing panel on all configurations. This sheet (shaded area on the figures) coils up to form a nearly circular pattern one semi-span behind the trailing edge. Addition of strake area seems to have little influence on vortex core positions near the trailing edge at the higher angles of attack.

VORTEX CORE BREAKDOWN

Vortex "breakdown" or "explosion" is the name given to an observed sudden increase in diameter, or flaring,

of the rotational core associated with a real fluid vortex. Since the phenomenon is usually observed using smoke or water vapor tracers in the fluid, the increased mixing and reduced velocities associated with the increase in diameter frequently obscure the core altogether. The term "breakdown" should not be presumed to mean that a vortex is no longer present, even though it may no longer be visible. The breakdown of a fluid vortex core is similar to the phenomena of transition from laminar to turbulent flow in viscous boundary layers in that it occurs quite suddenly. (See references 13 and 14.) The breakdown of wing-generated vortex cores progresses forward from a position aft of the wing. As the vortex core breakdown position moves forward across the trailing edge, it begins to influence wing lift since upper surface induced velocities and pressures are affected.

Poisson-Quinton has related the onset of vortex breakdown on delta wings to a decrease in the non-linear lift force. He presents an experimental correlation which shows the dependence of breakdown on angle of attack and wing sweep angle. This curve is reproduced in figure 21. Although the curve applies strictly only to simple delta wings, it might give reasonable results for near-delta wings, such as double-delta or ogee configurations, if the aspect ratio were used as a parameter rather than sweep angle. Using aspect ratio as a parameter has the

effect of defining an average sweep angle for non-delta wings. As stated above, vortex breakdown limits non-linear or "vortex" lift. This means that the onset of vortex breakdown is marked by the attainment of a maximum slope in the C_L versus α curve, or a maximum value of C_{L_α} . The table below compares vortex breakdown angle as predicted by Poisson-Quinton and angle for maximum C_{L_α} from the present tests.

Comparison of Vortex Core Breakdown Angle with
Angle for Maximum C_{L_α}

<u>Wing</u>	<u>A</u>	<u>Angle for Vortex Core Breakdown</u>	<u>Angle for Maximum C_{L_α}</u>
62°	1.80	18°	14°
75°/62° Δ^2	1.61	23°	20°
80°/62° Δ^2	1.64	22°	22°

The agreement between the columns is considered quite good. It is especially interesting to note that these figures indicate that at a 20° angle of attack the 62° delta wing should be experiencing vortex core breakdown, while the double-delta wings should not have breakdown.

To determine whether vortex core breakdown had occurred, measurements of vortex core diameter were made from the flow field maps. "Vortex core radius" was taken as the average distance from the apparent center of the vortex to the maximum rotational velocity position. The results of these measurements are shown in figure 22. The double-

delta configurations may be nearing breakdown at the trailing edge, but the breakdown is obviously much further advanced on the 62° delta. These measurements lend additional validity to the Poisson-Quinton curve as a means of predicting breakdown.

We are now in a position to describe more fully some of the apparent anomalies in the flow visualization, pressure and force data. When vortex core breakdown occurs, the ensuing mixing results in greatly increased viscous dissipation which causes reduced circulation. The larger core vortex results in lower, broader negative pressure peaks, increased regions of high sidewash velocities, outboard movement of the secondary separation line, and reduced lift curve slope.

The peculiar kinks in the $80^\circ/62^\circ$ double-delta force data apparently are the result of a sudden forward movement of the vortex core breakdown point to a new, more stable, position. The breakdown point presumably then proceeds forward in a more orderly fashion.

CONCLUDING REMARKS

No adequate technique is available for predicting delta and double-delta wing lift. The semi-empirical method of Poisson-Quinton is the most satisfactory method available at the present time, but additional experimental work and additional correlation of experimental data will be required to define the range of values for the thickness coefficient, k .

Flow field measurements generally confirm the patterns assumed in theoretical models except for the presence of a secondary, reversed vortex. Vortex strength values and vortex spans are considerably less than those predicted by mathematical models. The reversed vortex does not appear to be of sufficient magnitude to account for the discrepancy between theory and experiment. The onset of vortex core breakdown and attendant reduced circulation seem to be responsible for the greatest discrepancy between experiment and theory. Additional work is indicated to better define the onset of breakdown, especially for planforms other than simple deltas.

Vortex sheet measurements show that the vorticity shed per unit time from sharp leading edges is several times larger than that which is predicted by simple cross flow theory. Also, a maximum vorticity rate is reached

at angles of attack roughly corresponding to maximum lift angles. The influence of vortex core breakdown on vortex sheet strength is probably important, but has not yet been explored.

REFERENCES

1. DeYoung, John; and Harper, Charles W.: Theoretical Symmetric Span Loading At Subsonic Speeds For Wings Having Arbitrary Planform. NACA Rept. 921, 1948.
2. Brown, Clinton E.; and Michael, W. H., Jr.: On Slender Wings with Leading Edge Separation. NACA TN 3430, 1955.
3. Mangler, K. W.; and Smith, J. H. B.: A Theory of Slender Wings with Leading Edge Separation. Proc. Royal Soc. London, Series A, Vol. 251, 1959, p. 200.
4. Wentz, W. H., Jr.; and McMahon, M. C.: An Experimental Investigation of the Flow Fields About Delta and Double-Delta Wings at Low Speeds. Wichita State University Aeronautical Report 65-2, September 1965.
5. Jones, R. T.: Properties of Low-Aspect Ratio Pointed Wings at Speeds Below and Above the Speed of Sound. NACA Rept. 835, 1946.
6. Poisson-Quinton, P.; and Erlich, E.: Hyperlift and Balancing of Slender Wings. NASA TT 9523, 1965.
7. Bergesen, A. J.; and Porter, J. D.: An Investigation of the Flow Around Slender Delta Wings with Leading Edge Separation. ONR Report No. 510, Princeton Univ. Press, May 1960.
8. Razak, K.; and Snyder, M. H.: A Review of the Planform Effects on the Low-Speed Aerodynamic Characteristics of Triangular and Modified Triangular Wings. NASA CR-421, 1966.
9. Sacks, A. H.; Neilson, J. N.; and Goodwin, F. K.: A Theory For the Low-Speed Aerodynamics of Straight and Swept Wings With Flow Separation. Vidya Report No. 91, March 31, 1963.
10. Fage, A.; and Johansen, F. C.: The Structure of Vortex Sheets. Phil. Mag., (7) Vol. 5 No. 28, February 1928, pp. 417-441.
11. Goldstein, Sidney: Modern Developments in Fluid Mechanics. Vol II pp. 553-556, Dover Publication Inc.

12. Snyder, M. H.: A Non-Rotating Vorticity Meter. Wichita State University Aeronautical Report 66-3, 1966.
13. Earnshaw, P. B.: Measurements of Vortex-Breakdown Position at Low Speed on a Series of Sharp-Edged Symmetrical Models. British R. A. E. Tech. Rept. 64047, 1964, N65-20733.
14. Werle, H.: Sur l'Eclatement des Tourbillons d'Apex d'Une Aile Delta Aux Faibles Vitesses. La Recherche Aeronautique, No. 74, Jan.-Feb. 1960, pp. 23-30. (Available in translation in Wichita State University Aeronautical Report 66-4, 1966.)
15. Wind tunnel data from Lockheed, Co., California, Report LR 19188, 1965.
16. Spreiter, J. H.: The Aerodynamic Forces on Slender Plane-and Cruciform-Wing and Body Combinations. NACA Rept. 962, 1950.

LIST OF FIGURES

- Figure 1a 62° Delta Wing Configuration
- Figure 1b 75°/62° Double-Delta Wing Configuration
- Figure 1c 80°/62° Double-Delta Wing Configuration
- Figure 2 Coordinate System
- Figure 3a Model Installation
- Figure 3b Model and Probe Installation
- Figure 3c Basic Velocity Probe
- Figure 3d Special Velocity Probe
- Figure 4a Lift Characteristic, 80°/62° Double-Delta Wing
- Figure 4b Lift-Drag Polar, 80°/62° Double-Delta Wing
- Figure 4c Stability Characteristic, 80°/62° Double Delta Wing
- Figure 5a Lift Comparison, Delta and Double-Delta Wings
- Figure 5b Drag Comparison, Delta and Double-Delta Wings
- Figure 5c Stability Comparison, Delta and Double-Delta Wings
- Figure 6a Lift Comparison, 80°/62° Double-Delta Wing and 83°/65° Double-Delta Wing
- Figure 6b Drag Comparison, 80°/62° Double-Delta Wing and 83°/65° Double-Delta Wing
- Figure 6c Stability Comparison, 80°/62° Double-Delta Wing and 83°/65° Double-Delta Wing
- Figure 7a Comparison of Normal Force with Theory, 80°/62° Double-Delta Wing

- Figure 7b Lift Curve Slopes, 62° Delta Wing
- Figure 7c Lift Curve Slopes, 75°/62° Double-Delta Wing
- Figure 7d Lift Curve Slopes, 80°/62° Double-Delta Wing
- Figure 7e Comparison of Induced Drag with Theory, 80°/62°
Double-Delta Wing
- Figure 8a Upper Surface Pressure Distribution $\alpha = 0^\circ$,
80°/62° Double-Delta Wing
- Figure 8b Upper Surface Pressure Distribution $\alpha = 5^\circ$,
80°/62° Double-Delta Wing
- Figure 8c Upper Surface Pressure Distribution $\alpha = 10^\circ$,
80°/62° Double-Delta Wing
- Figure 8d Upper Surface Pressure Distribution $\alpha = 15^\circ$,
80°/62° Double-Delta Wing
- Figure 8e Upper Surface Pressure Distribution $\alpha = 20^\circ$,
80°/62° Double-Delta Wing
- Figure 8f Upper Surface Pressure Distribution $\alpha = 25^\circ$,
80°/62° Double-Delta Wing
- Figure 8g Upper Surface Pressure Distribution $\alpha = 30^\circ$,
80°/62° Double-Delta Wing
- Figure 8h Upper Surface Pressure Distribution $\alpha = 35^\circ$,
80°/62° Double-Delta Wing
- Figure 8i Upper Surface Pressure Distribution $\alpha = 40^\circ$,
80°/62° Double-Delta Wing
- Figure 8j Effect of Strake on Pressure Distribution $\alpha = 20^\circ$

- Figure 9a Tuft Pattern $\alpha = 0^\circ, 80^\circ/62^\circ$ Double-Delta Wing
- Figure 9b Tuft and Oil Streak Patterns $\alpha = 5^\circ, 80^\circ/62^\circ$
Double-Delta Wing
- Figure 9c Tuft and Oil Streak Patterns $\alpha = 6^\circ, 80^\circ/62^\circ$
Double-Delta Wing
- Figure 9d Oil Streak Pattern $\alpha = 6 \frac{1}{2}^\circ, 80^\circ/62^\circ$ Double-Delta Wing
- Figure 9e Oil Streak Pattern $\alpha = 7^\circ, 80^\circ/62^\circ$ Double-Delta Wing
- Figure 9f Tuft and Oil Streak Patterns $\alpha = 8^\circ, 80^\circ/62^\circ$
Double-Delta Wing
- Figure 9g Tuft and Oil Streak Patterns $\alpha = 10^\circ, 80^\circ/62^\circ$
Double-Delta Wing
- Figure 9h Tuft and Oil Streak Patterns $\alpha = 15^\circ, 80^\circ/62^\circ$
Double-Delta Wing
- Figure 9i Tuft and Oil Streak Patterns $\alpha = 20^\circ, 80^\circ/62^\circ$
Double-Delta Wing
- Figure 9j Tuft and Oil Streak Patterns $\alpha = 25^\circ, 80^\circ/62^\circ$
Double-Delta Wing
- Figure 9k Tuft and Oil Streak Patterns $\alpha = 30^\circ, 80^\circ/62^\circ$
Double-Delta Wing
- Figure 9l Tuft and Oil Streak Patterns $\alpha = 35^\circ, 80^\circ/62^\circ$
Double-Delta Wing
- Figure 9m Tuft and Oil Streak Patterns $\alpha = 40^\circ, 80^\circ/62^\circ$
Double-Delta Wing

- Figure 10a Upper Surface Flow Field $80^\circ/62^\circ$ Double-Delta
Wing $\alpha = 5^\circ$, $x/b = 1.839$
- Figure 10b Upper Surface Flow Field $80^\circ/62^\circ$ Double-Delta
Wing $\alpha = 5^\circ$, $x/b = 1.326$
- Figure 10c Upper Surface Flow Field $80^\circ/62^\circ$ Double-Delta
Wing $\alpha = 5^\circ$, $x/b = .574$
- Figure 10d Upper Surface Flow Field $80^\circ/62^\circ$ Double-Delta
Wing $\alpha = 5^\circ$, $x/b = .027$
- Figure 10e Upper Surface Flow Field $80^\circ/62^\circ$ Double-Delta
Wing $\alpha = 5^\circ$, $x/b = -1.0$
- Figure 10f Upper Surface Flow Field $80^\circ/62^\circ$ Double-Delta
Wing $\alpha = 5^\circ$, $x/b = -2.0$
- Figure 11a Upper Surface Flow Field $80^\circ/62^\circ$ Double-Delta
Wing $\alpha = 10^\circ$, $x/b = 1.839$
- Figure 11b Upper Surface Flow Field $80^\circ/62^\circ$ Double-Delta
Wing $\alpha = 10^\circ$, $x/b = 1.326$
- Figure 11c Upper Surface Flow Field $80^\circ/62^\circ$ Double-Delta
Wing $\alpha = 10^\circ$, $x/b = .574$
- Figure 11d Upper Surface Flow Field $80^\circ/62^\circ$ Double-Delta
Wing $\alpha = 10^\circ$, $x/b = .027$
- Figure 11e Upper Surface Flow Field $80^\circ/62^\circ$ Double-Delta
Wing $\alpha = 10^\circ$, $x/b = -1.0$
- Figure 11f Upper Surface Flow Field $80^\circ/62^\circ$ Double-Delta
Wing $\alpha = 10^\circ$, $x/b = -2.0$

- Figure 12a Upper Surface Flow Field $80^\circ/62^\circ$ Double-Delta
Wing $\alpha = 20^\circ$, $x/b = 1.839$
- Figure 12b Upper Surface Flow Field $80^\circ/62^\circ$ Double-Delta
Wing $\alpha = 20^\circ$, $x/b = 1.326$
- Figure 12c Upper Surface Flow Field $80^\circ/62^\circ$ Double-Delta
Wing $\alpha = 20^\circ$, $x/b = .574$
- Figure 12d Upper Surface Flow Field $80^\circ/62^\circ$ Double-Delta
Wing $\alpha = 20^\circ$, $x/b = .027$
- Figure 12e Upper Surface Flow Field $80^\circ/62^\circ$ Double-Delta
Wing $\alpha = 20^\circ$, $x/b = -1.0$
- Figure 12f Upper Surface Flow Field $80^\circ/62^\circ$ Double-Delta
Wing $\alpha = 20^\circ$, $x/b = -2.0$
- Figure 13a Upper Surface Flow Field 62° Delta Wing $\alpha = 5^\circ$,
 $x/b = 1.326$
- Figure 13b Upper Surface Flow Field 62° Delta Wing $\alpha = 5^\circ$,
 $x/b = .574$
- Figure 13c Upper Surface Flow Field 62° Delta Wing $\alpha = 5^\circ$,
 $x/b = .027$
- Figure 13d Upper Surface Flow Field 62° Delta Wing $\alpha = 5^\circ$,
 $x/b = -1.0$
- Figure 13e Upper Surface Flow Field 62° Delta Wing $\alpha = 5^\circ$,
 $x/b = -2.0$
- Figure 14a Upper Surface Flow Field 62° Delta Wing $\alpha = 10^\circ$,
 $x/b = 1.326$
- Figure 14b Upper Surface Flow Field 62° Delta Wing $\alpha = 10^\circ$,
 $x/b = .574$

Figure 14c Upper Surface Flow Field 62° Delta Wing $\alpha = 10^\circ$,
 $x/b = .027$

Figure 14d Upper Surface Flow Field 62° Delta Wing $\alpha = 10^\circ$,
 $x/b = -1.0$

Figure 14e Upper Surface Flow Field 62° Delta Wing $\alpha = 10^\circ$,
 $x/b = -2.0$

Figure 15a Upper Surface Flow Field 62° Delta Wing $\alpha = 20^\circ$,
 $x/b = 1.326$

Figure 15b Upper Surface Flow Field 62° Delta Wing $\alpha = 20^\circ$,
 $x/b = .574$

Figure 15c Upper Surface Flow Field 62° Delta Wing $\alpha = 20^\circ$,
 $x/b = .027$

Figure 15d Upper Surface Flow Field 62° Delta Wing $\alpha = 20^\circ$,
 $x/b = -1.0$

Figure 15e Upper Surface Flow Field 62° Delta Wing $\alpha = 20^\circ$,
 $x/b = -2.0$

Figure 16a Upper Surface Flow Field 75°/62° Double-Delta
Wing $\alpha = 5^\circ$, $x/b = -1.0$

Figure 16b Upper Surface Flow Field 75°/62° Double-Delta
Wing $\alpha = 5^\circ$, $x/b = -2.0$

Figure 17a Upper Surface Flow Field 75°/62° Double-Delta
Wing $\alpha = 20^\circ$, $x/b = 1.326$

Figure 17b Upper Surface Flow Field 75°/62° Double-Delta
Wing $\alpha = 20^\circ$, $x/b = .574$

Figure 17c Upper Surface Flow Field 75°/62° Double-Delta
Wing $\alpha = 20^\circ$, $x/b = .027$

- Figure 17d Upper Surface Flow Field 75°/62 Double-Delta
Wing $\alpha = 20^\circ$, $x/b = -1.0$
- Figure 17e Upper Surface Flow Field 75°/62° Double-Delta
Wing $\alpha = 20^\circ$, $x/b = -2.0$
- Figure 18 Effect of Sweep Angle on Vortex Sheet Strength
- Figure 19a Circulation Integrals 62° Delta Wing, $\alpha = 10^\circ$
- Figure 19b Circulation Integrals 62° Delta Wing, $\alpha = 20^\circ$
- Figure 19c Circulation Integrals 75°/62° Double-Delta
Wing, $\alpha = 20^\circ$
- Figure 19d Circulation Integrals 80°/62° Double-Delta
Wing, $\alpha = 10^\circ$
- Figure 19e Circulation Integrals 80°/62° Double-Delta
Wing, $\alpha = 20^\circ$
- Figure 20a Vortex Core Center Locations 62° Delta Wing
- Figure 20b Vortex Core Center Locations 75°/62° Double-
Delta Wing
- Figure 20c Vortex Core Center Locations 80°/62° Double-
Delta Wing
- Figure 21 Vortex Core Breakdown Angle
- Figure 22 Effect of Strakes on Vortex Core Diameter

07

Wing Area 7.39 sq ft
Aspect Ratio 1.61
Mean Aerodynamic Cord 48.75 inches

75°/62° DOUBLE-DELTA

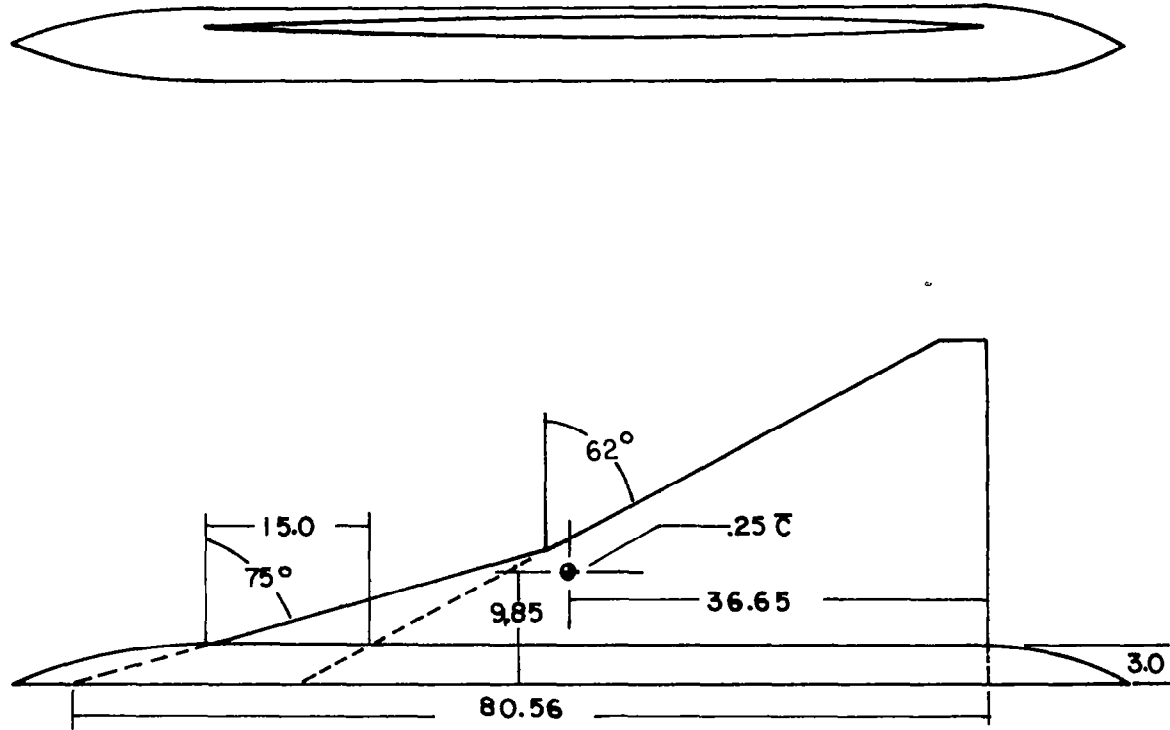


Figure 1b 75°/62° Double-Delta Wing Configuration

Wing Area 7.24 sq ft
Aspect Ratio 1.64
Mean Aerodynamic Cord 47.95

80°/62° DOUBLE DELTA

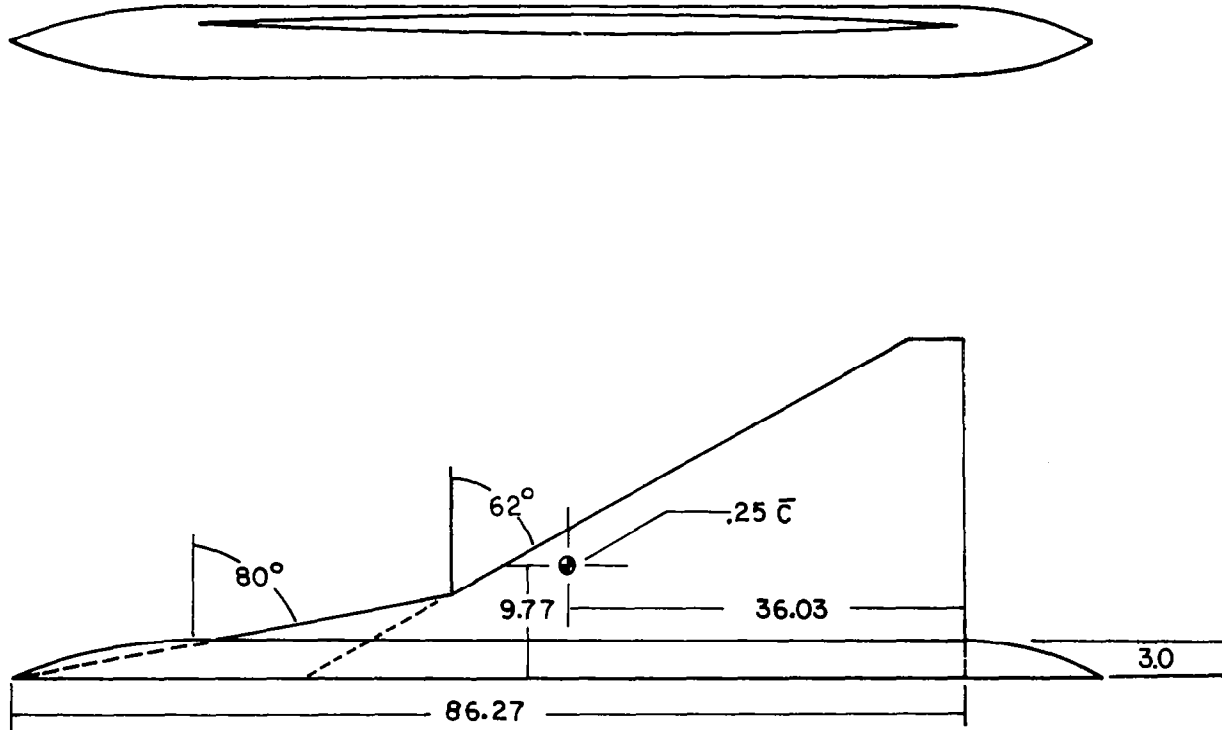


Figure 1c 80°/62° Double-Delta Wing Configuration

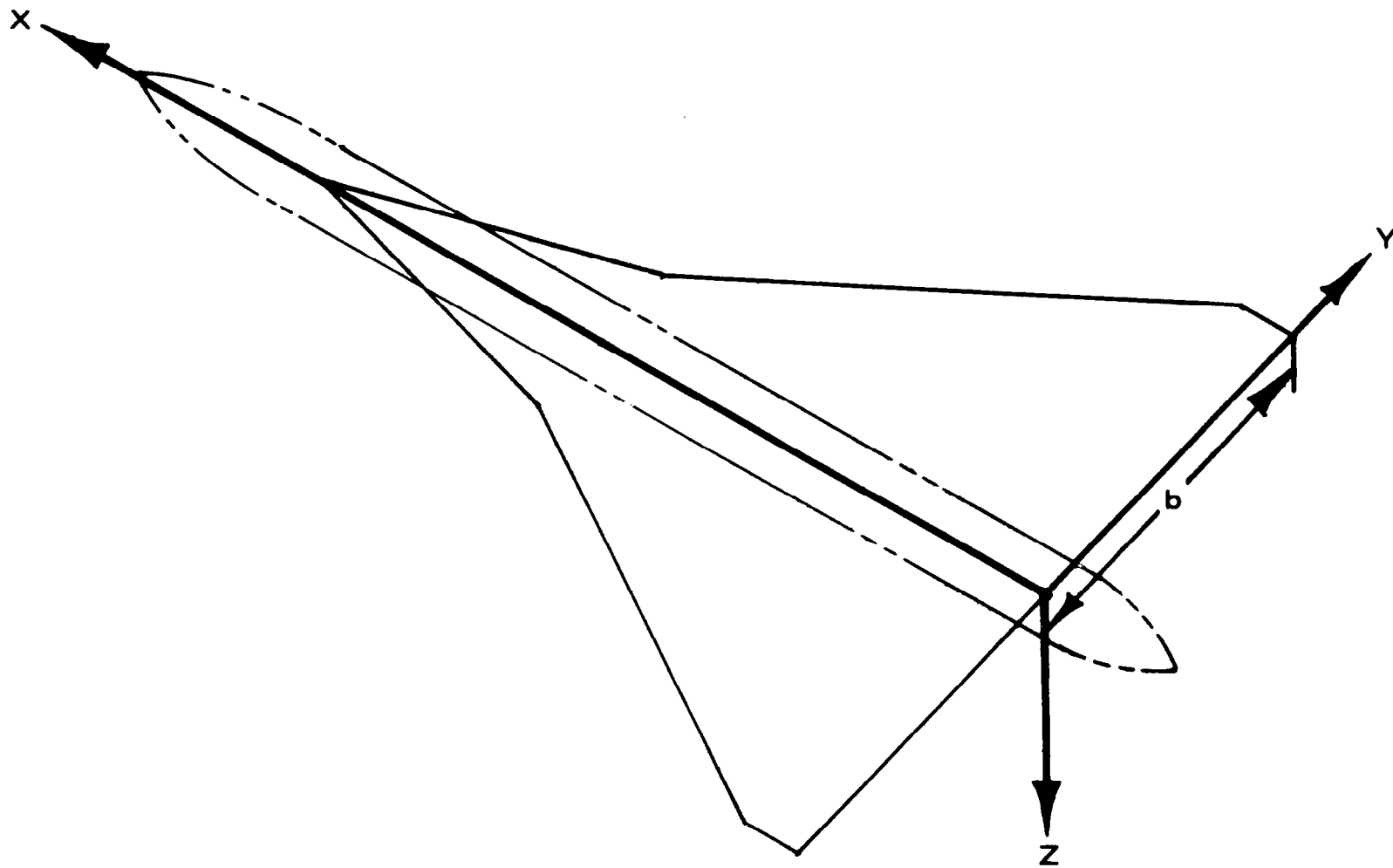


Figure 2 Coordinate System

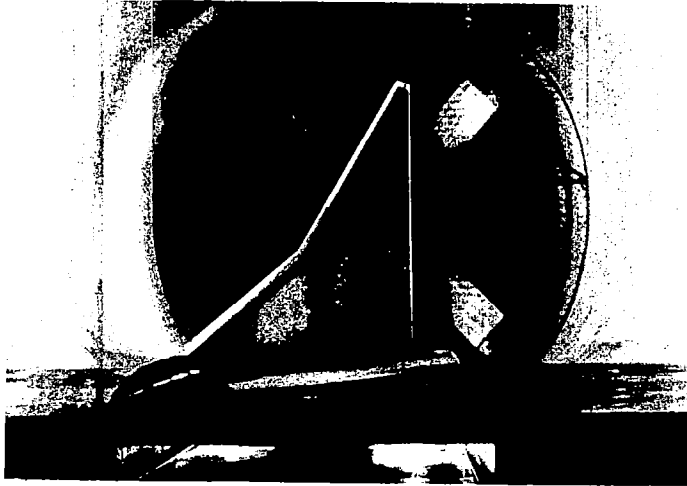


Figure 3a Model Installation

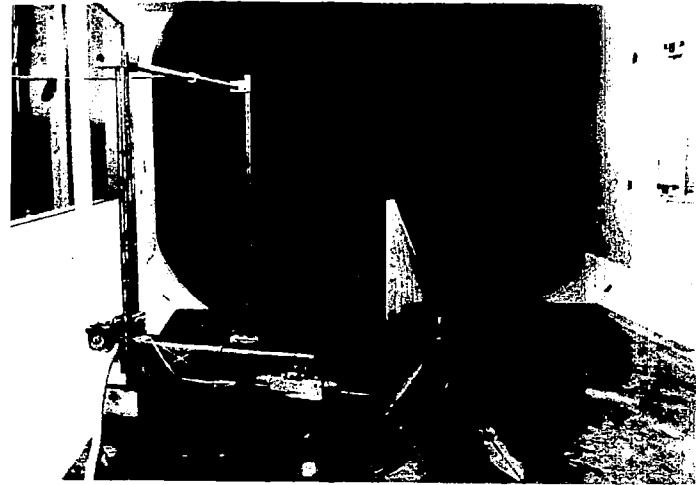


Figure 3b Model and Probe Installation

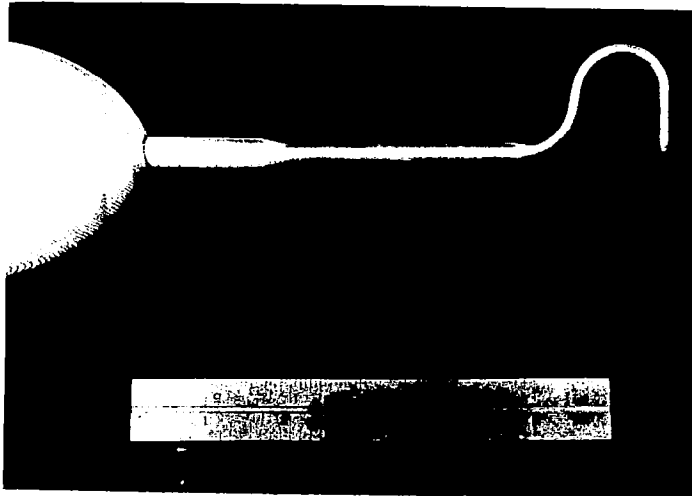


Figure 3c Basic Velocity Probe

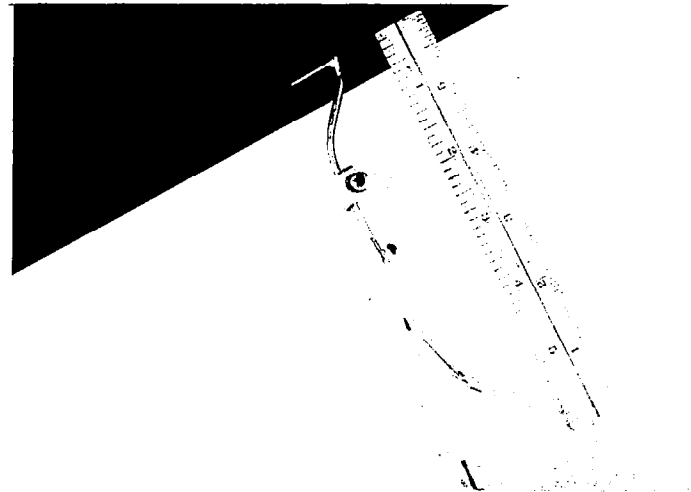


Figure 3d Special Velocity Probe

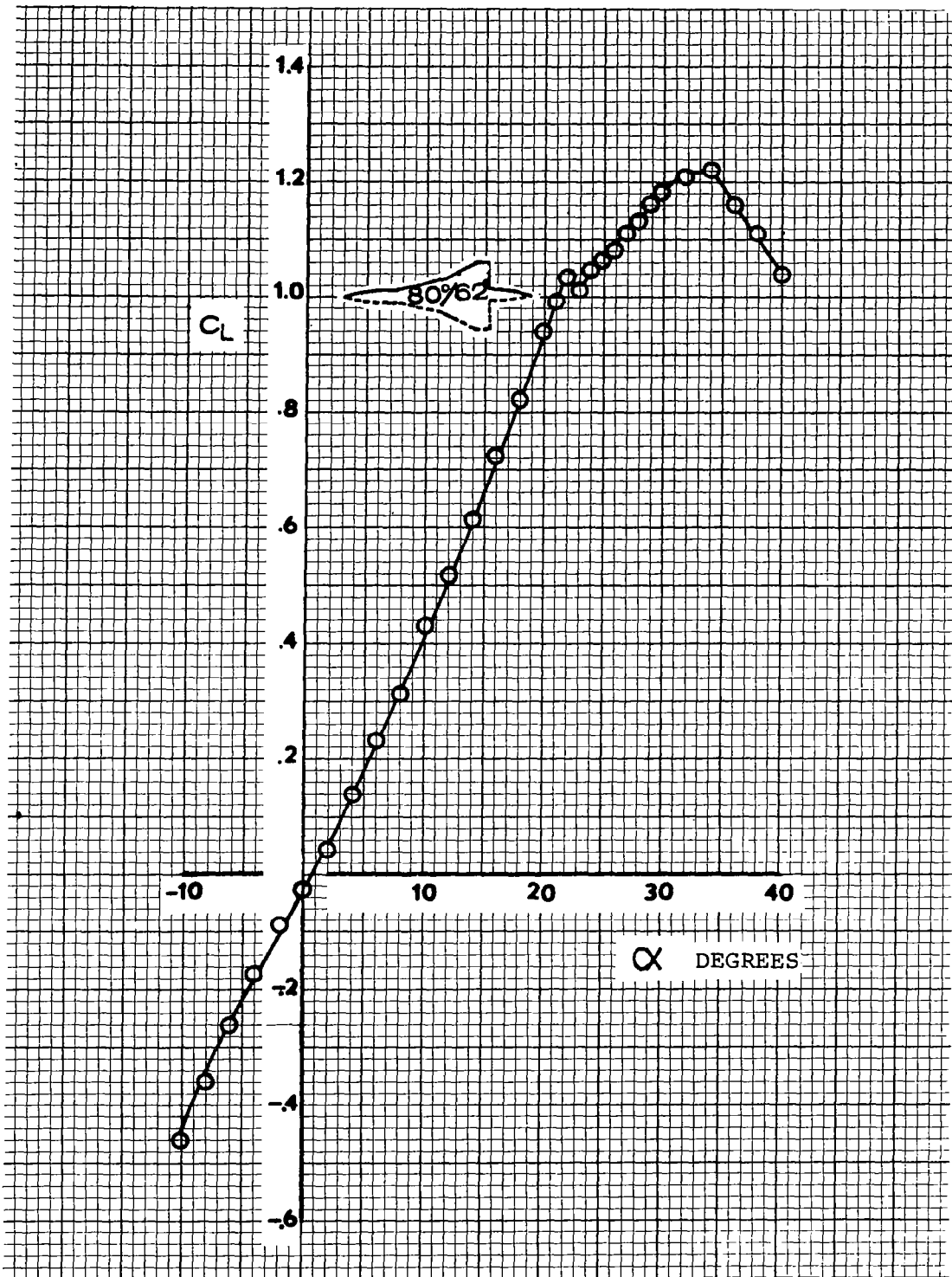


Figure 4a Lift Characteristic, 80°/62° Double-Delta Wing

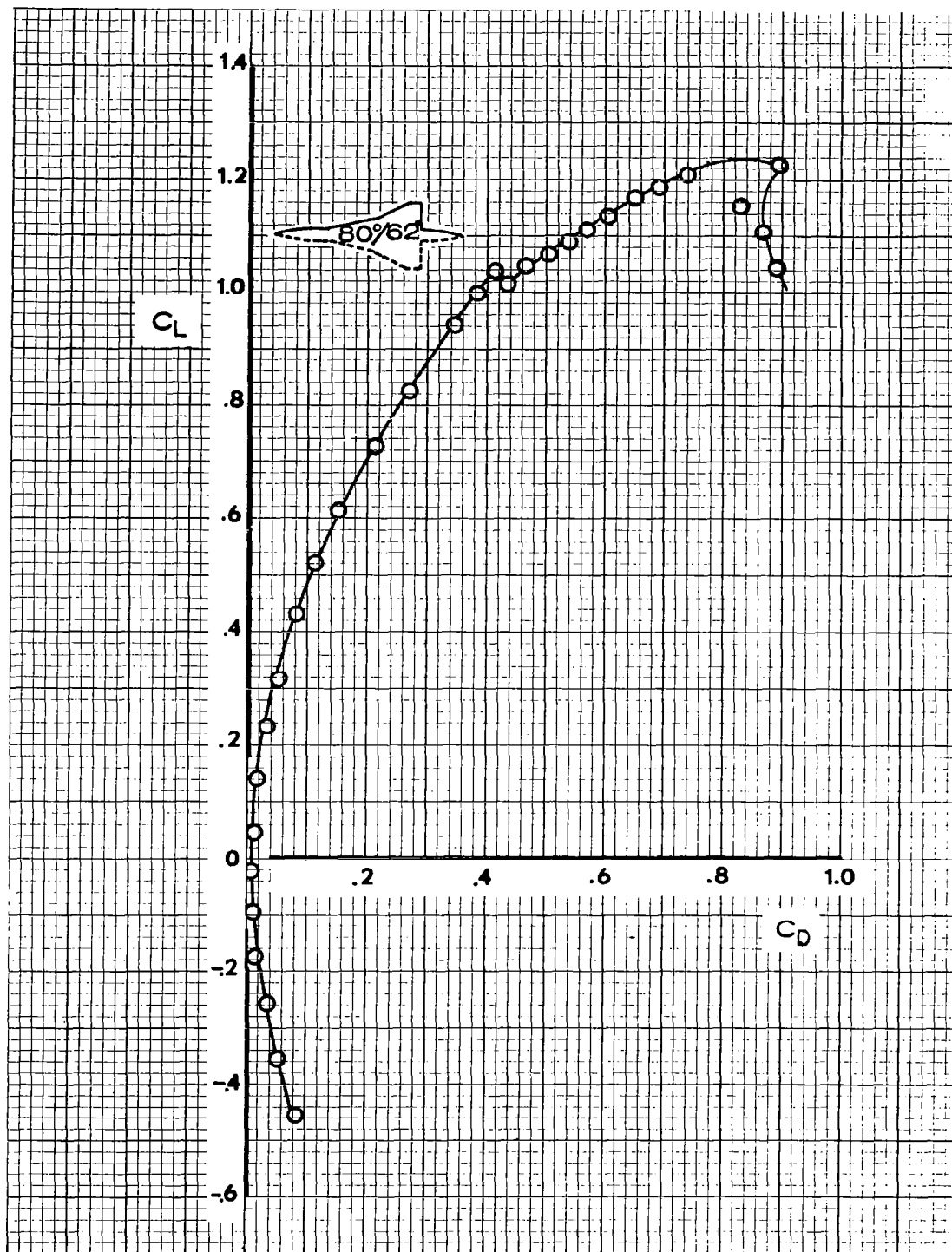


Figure 4b Lift-Drage Polar, 80°/62° Double-Delta Wing

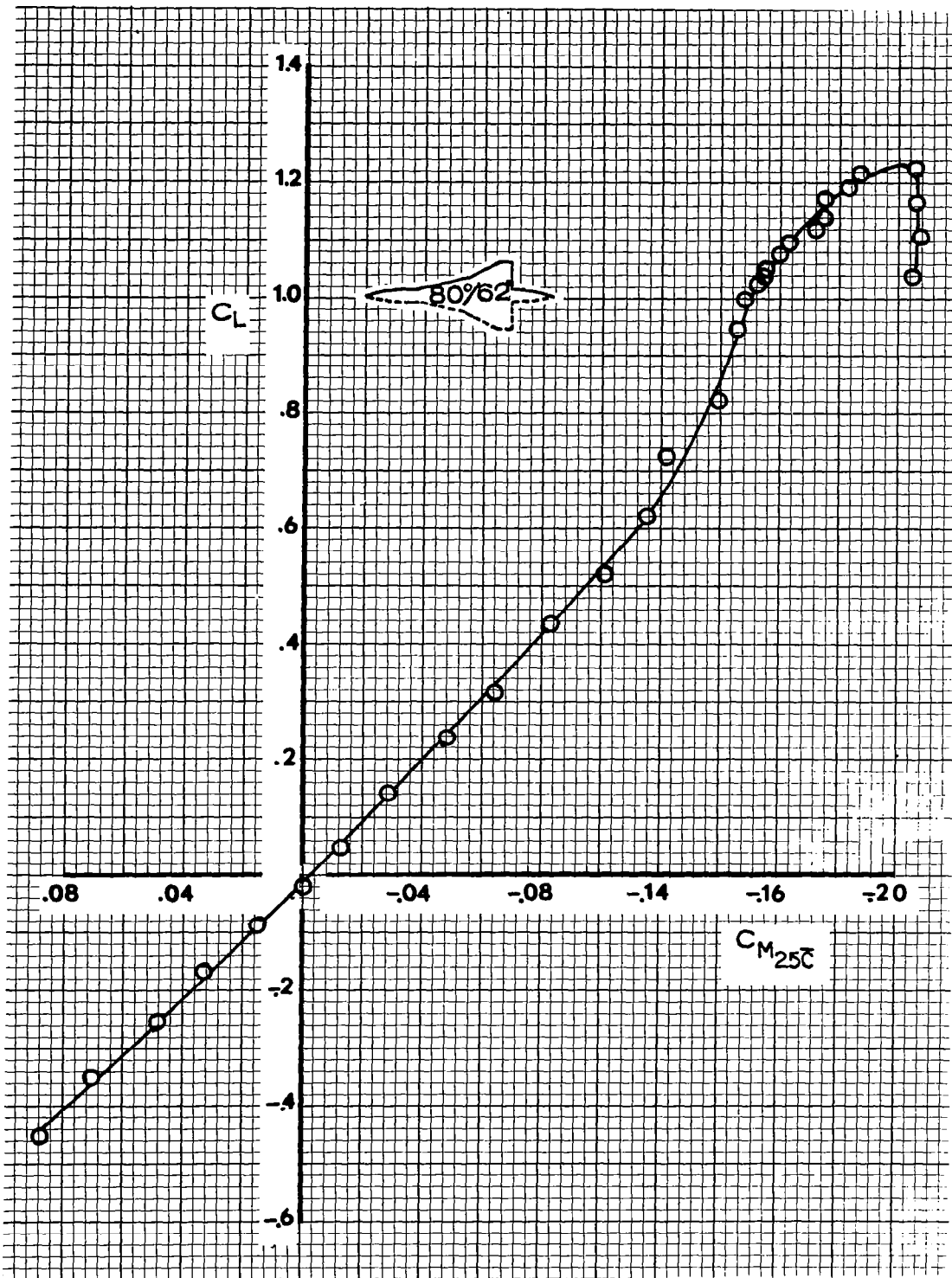


Figure 4c Stability Characteristic, 80°/62° Double-Delta Wing

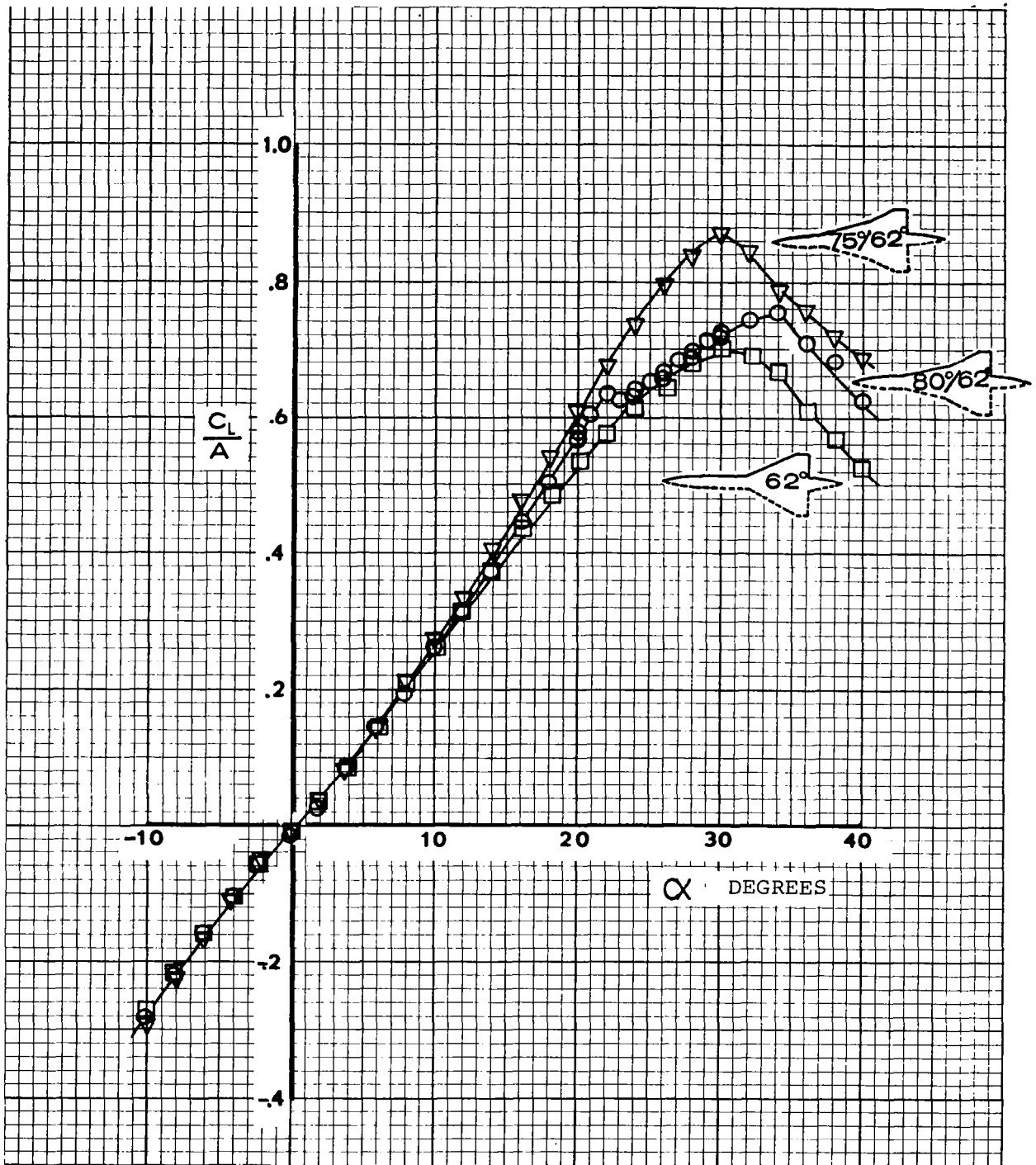


Figure 5a Lift Comparison, Delta and Double-Delta Wings

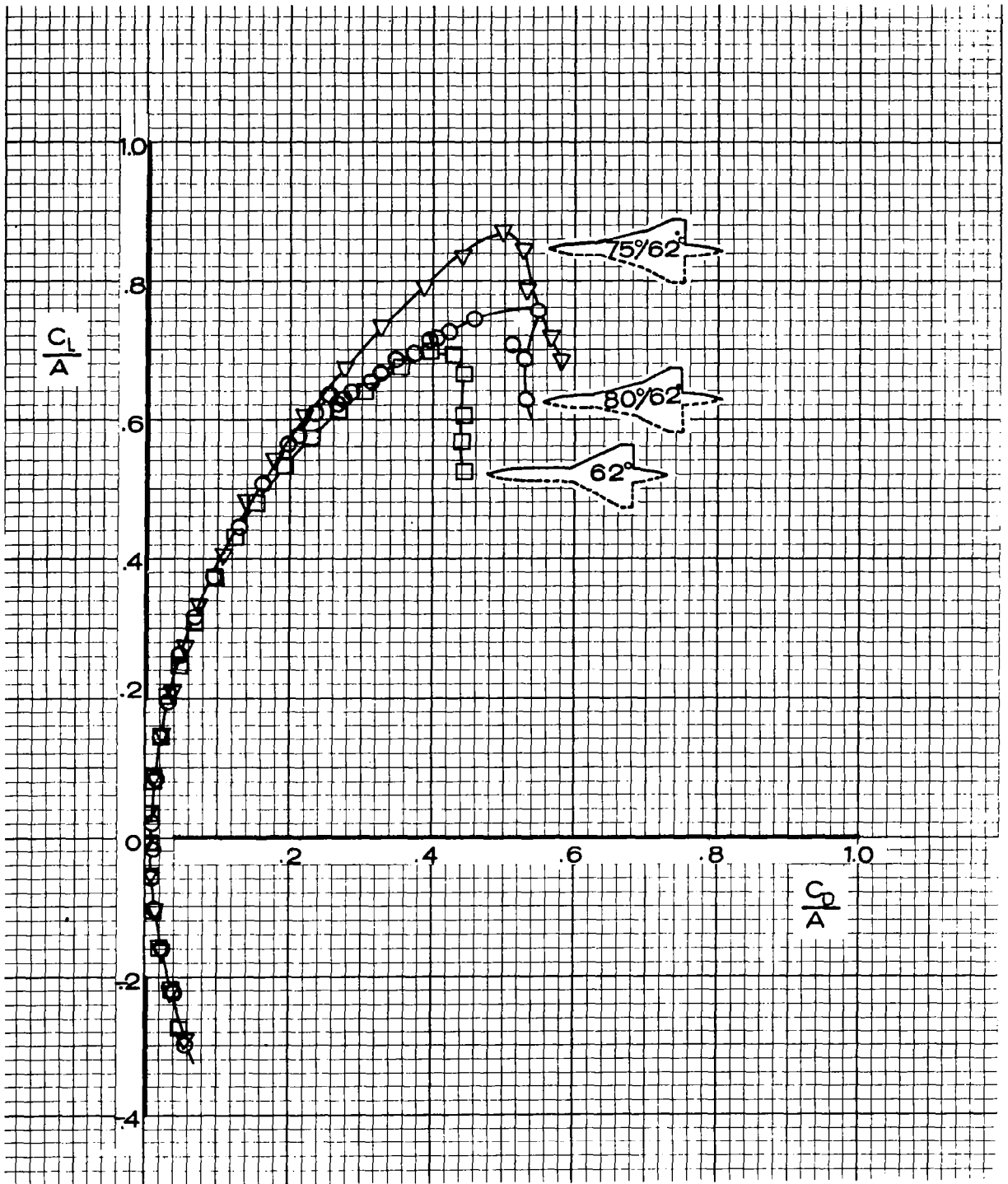


Figure 5b Drag Comparison, Delta and Double-Delta Wings

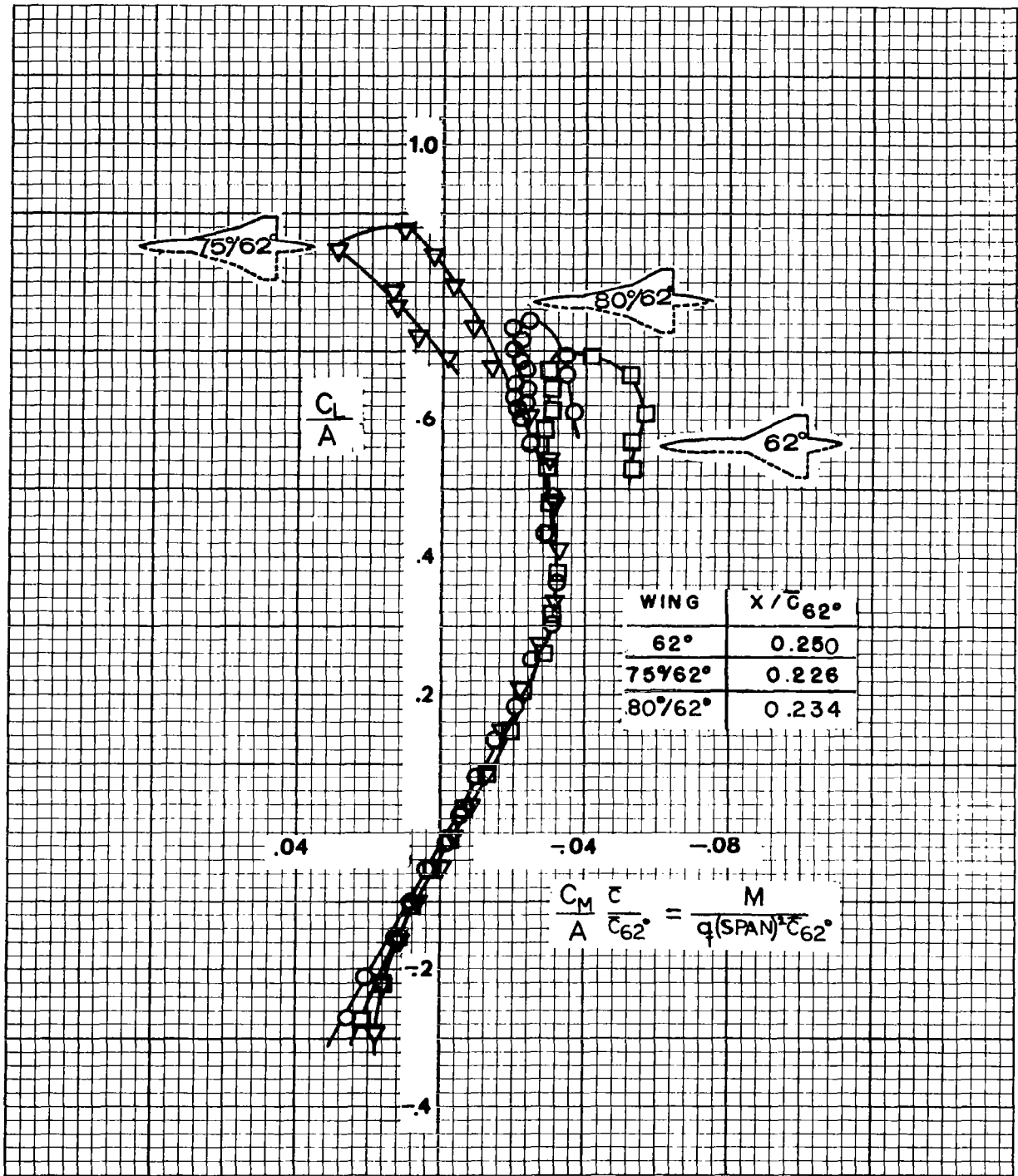


Figure 5c Stability Comparison, Delta and Double-Delta Wings

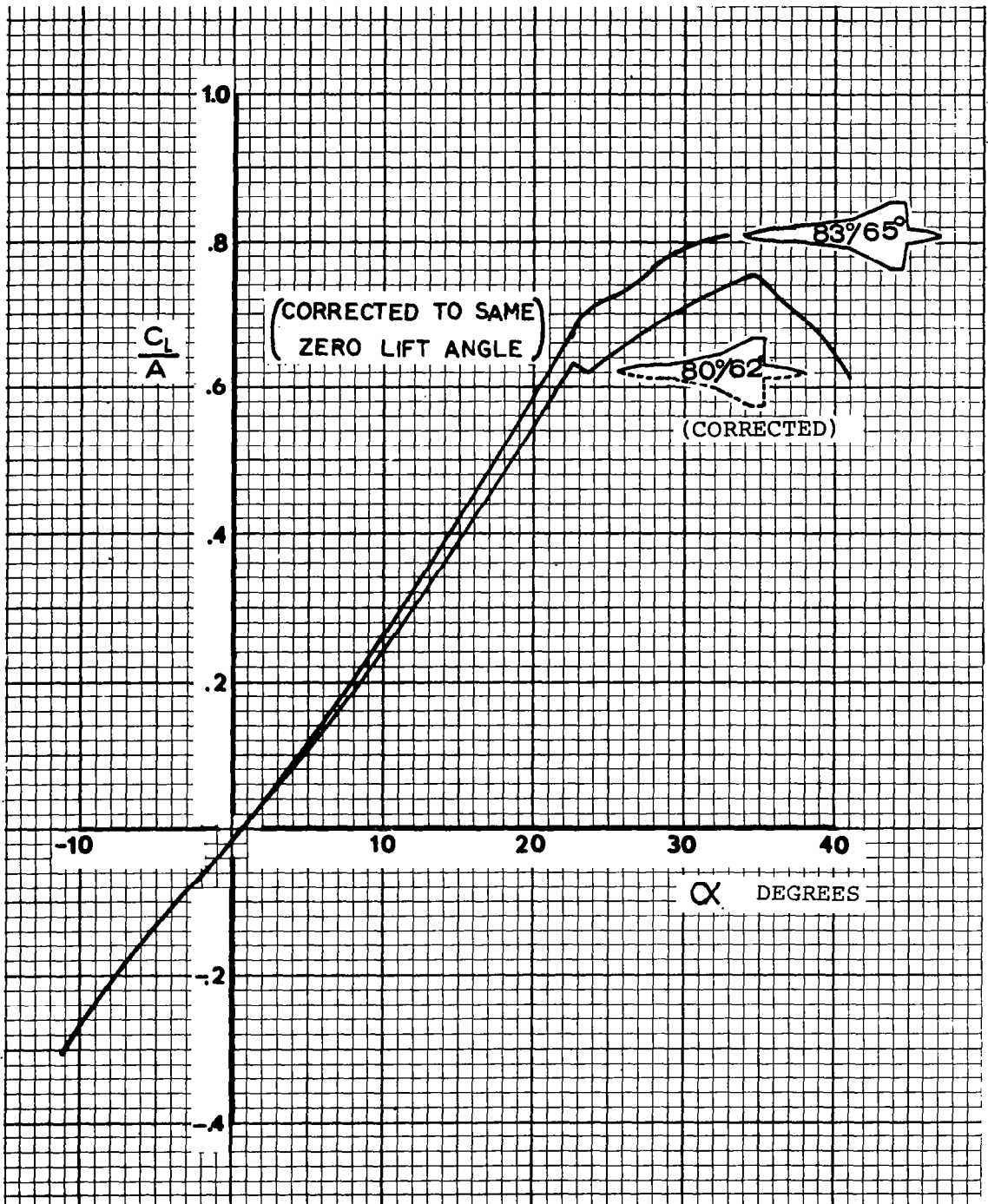


Figure 6a Lift Comparison, 80°/62° Double-Delta Wing and 83°/65° Double-Delta Wing

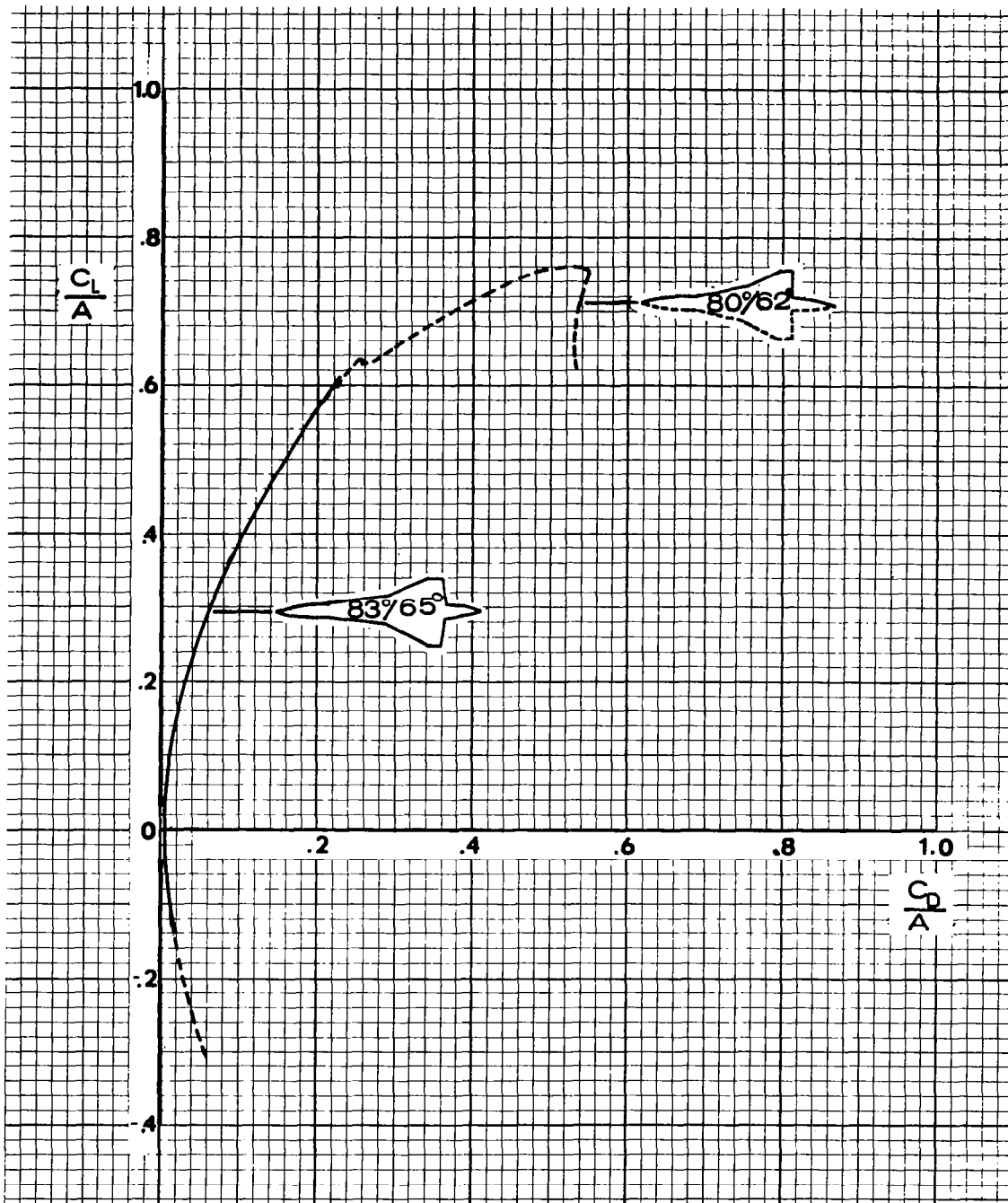


Figure 6b Drag Comparison, 80°/62° Double-Delta Wing and 83°/65° Double-Delta Wing

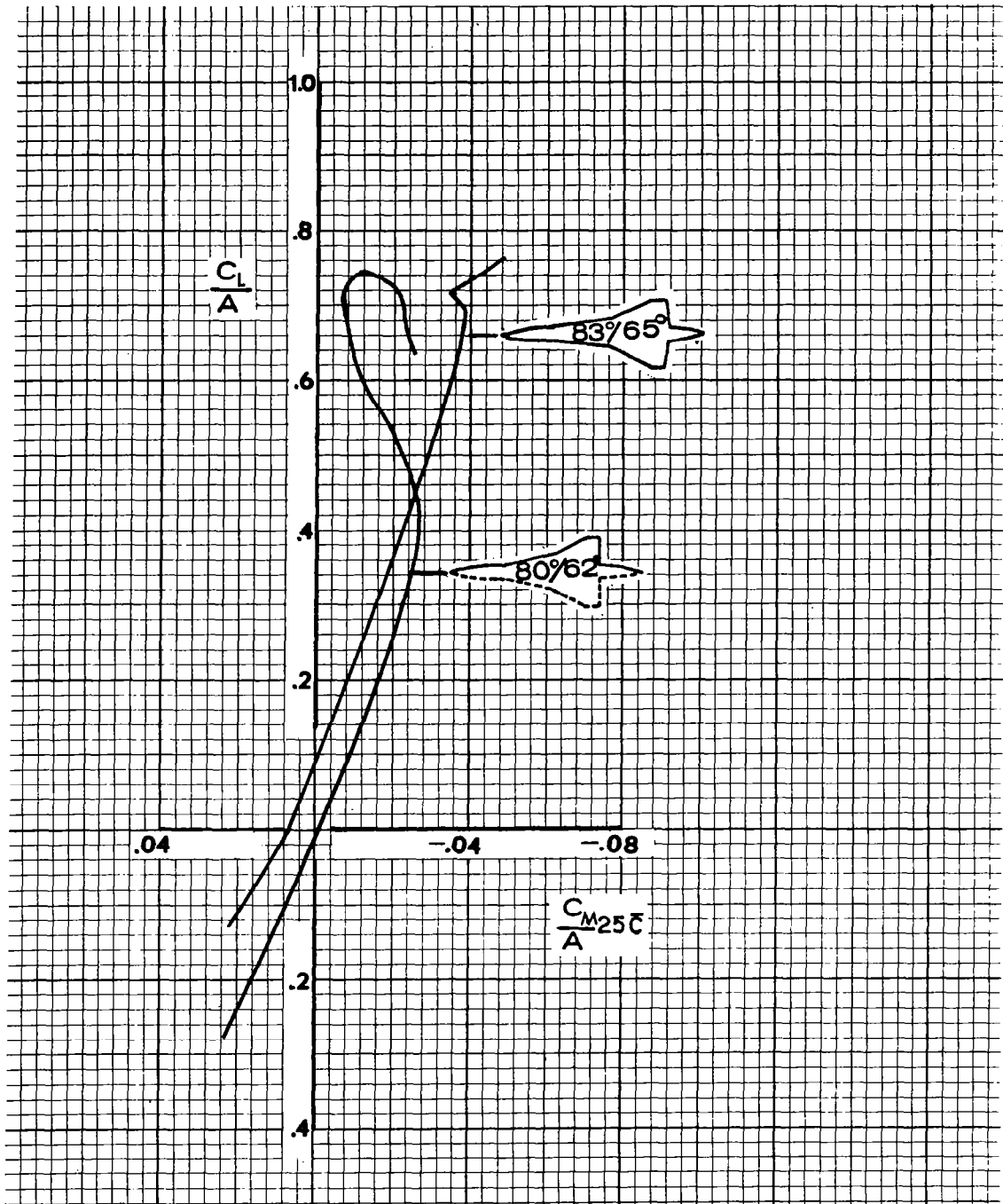


Figure 6c Stability Comparison, 80°/62° Double-Delta Wing and 83°/65° Double-Delta Wing

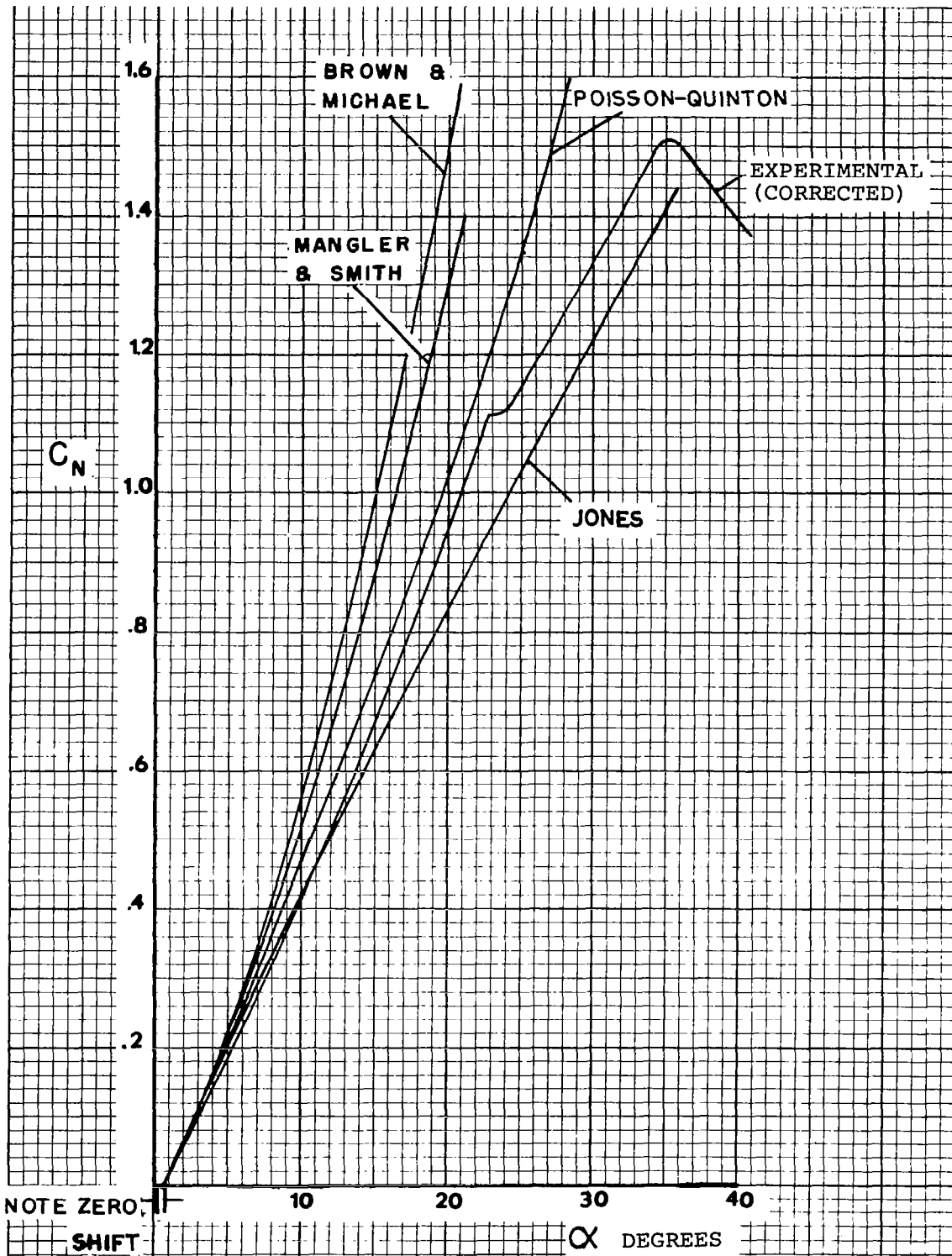


Figure 7a Comparison of Normal Force with Theory, $80^\circ/62^\circ$
Double-Delta Wing

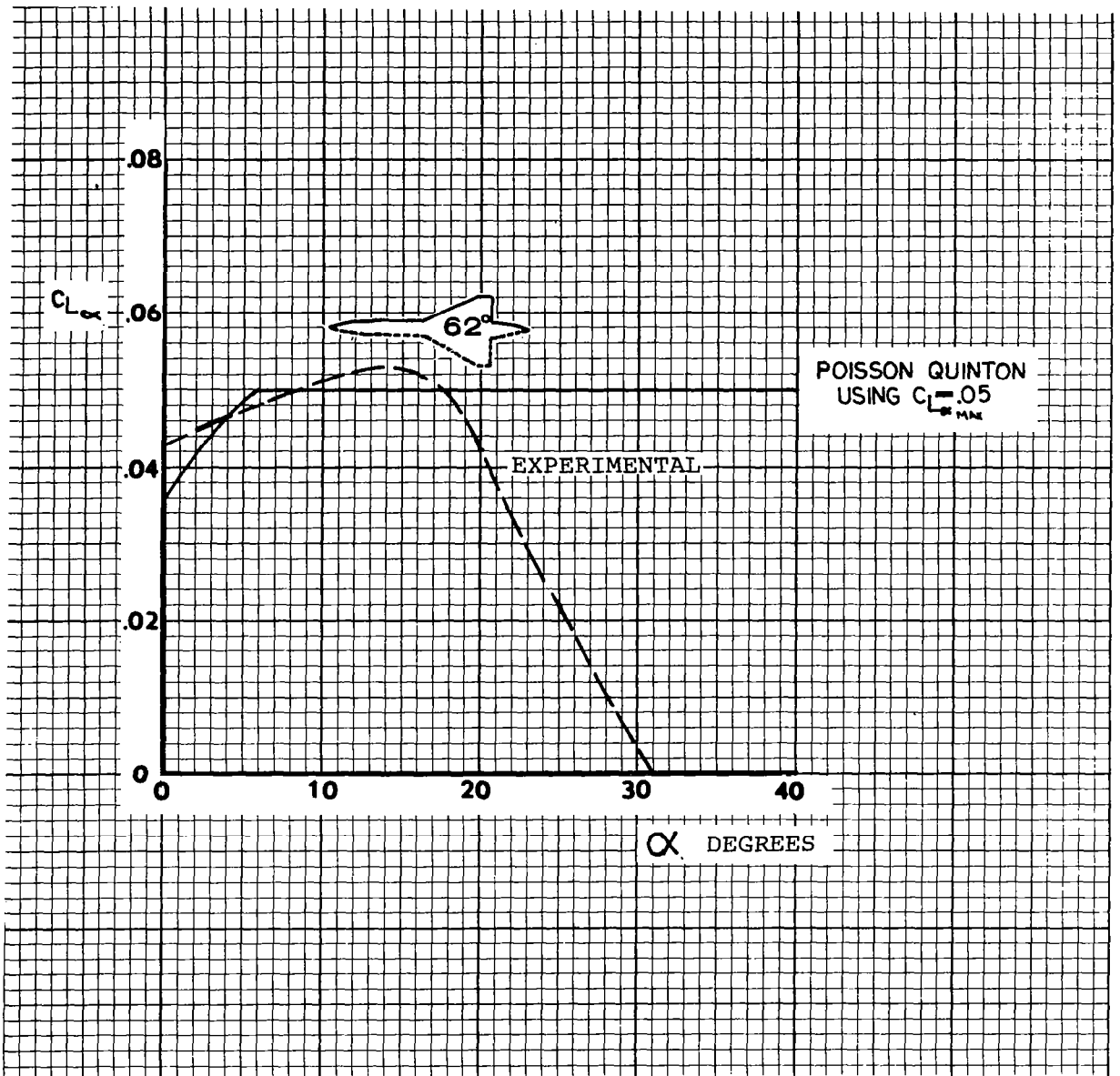


Figure 7b Lift Curve Slopes, 62° Delta Wing

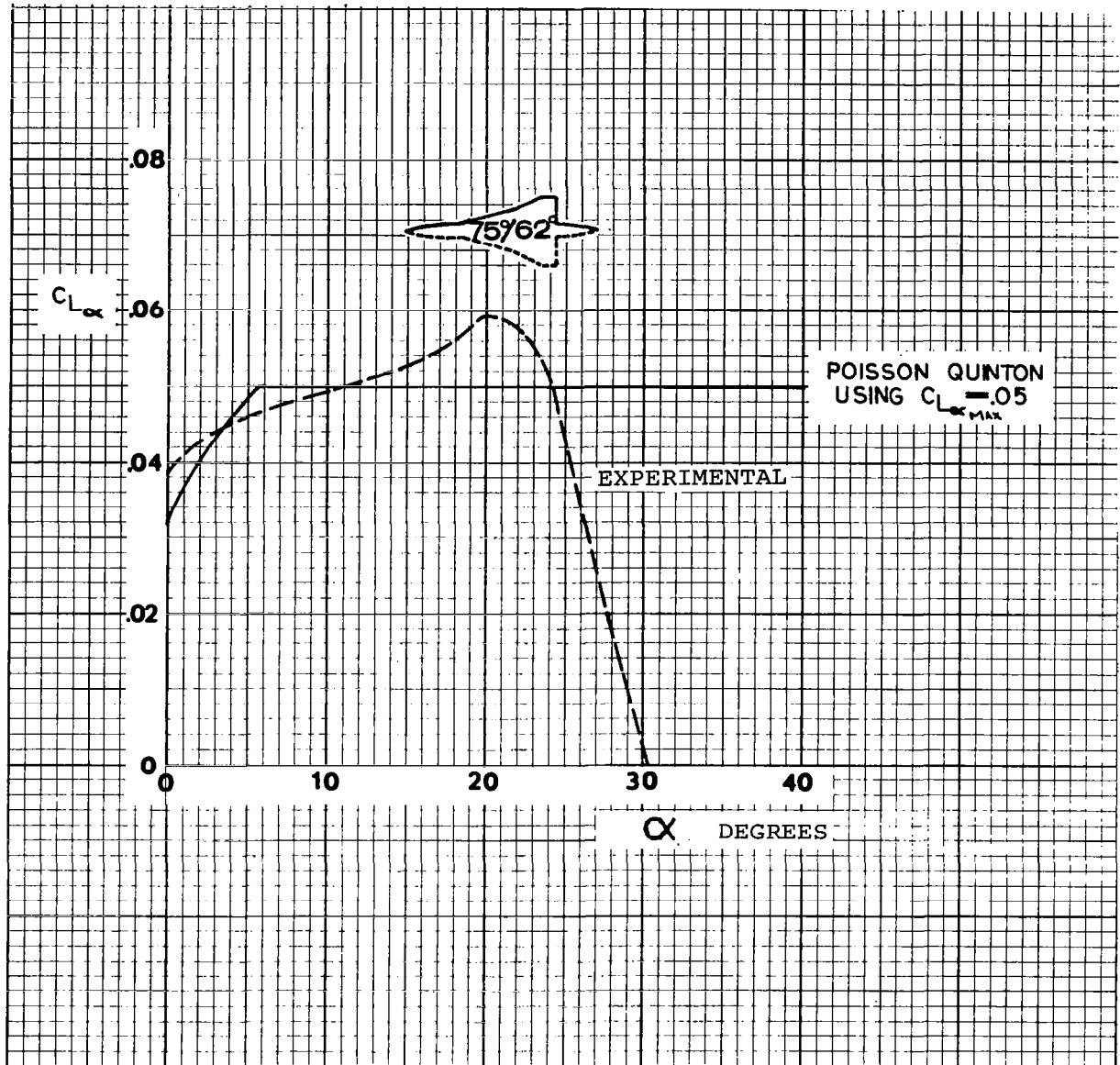


Figure 7c Lift Curve Slopes, 75°/62° Double-Delta Wing

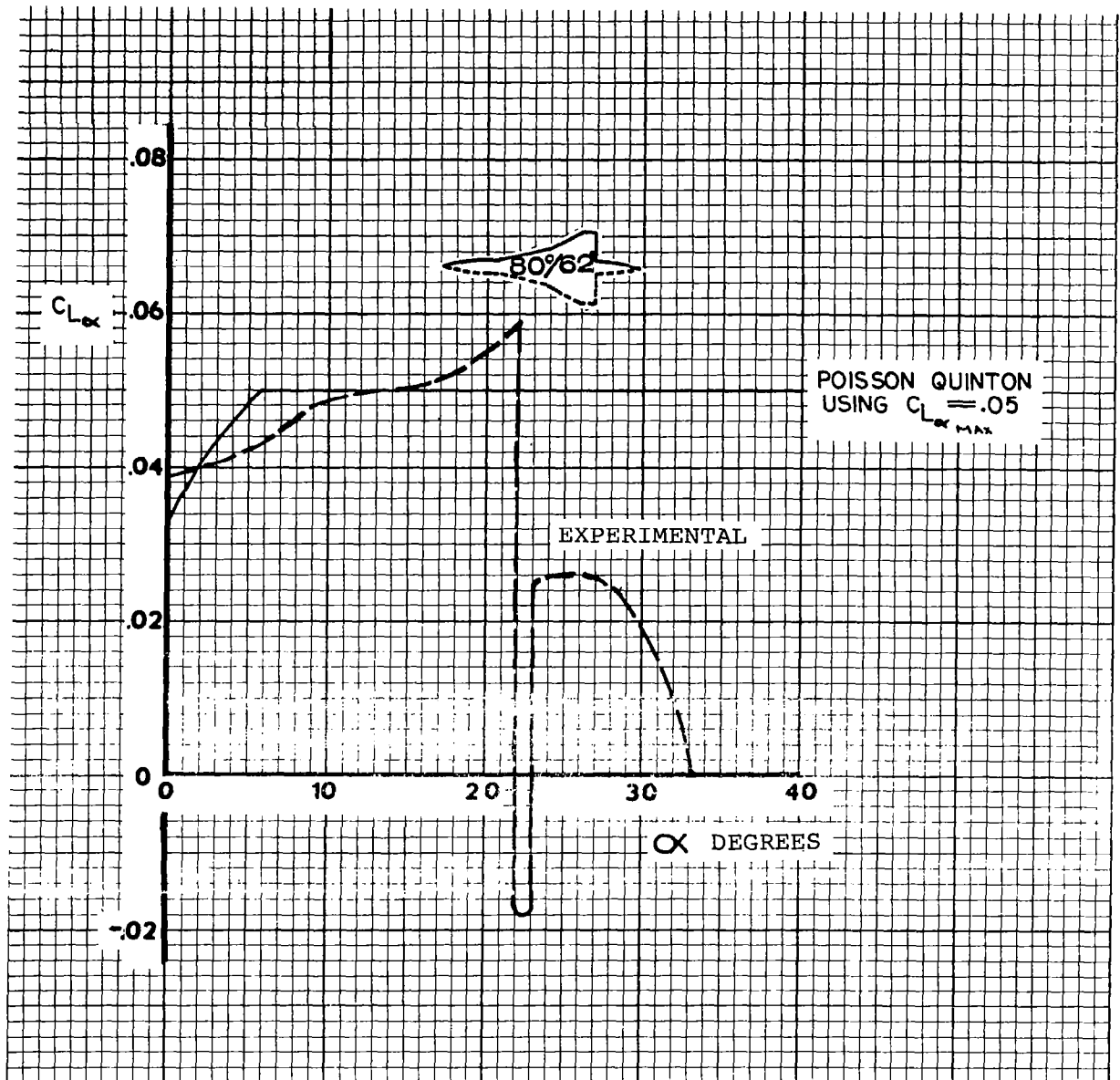


Figure 7d Lift Curve Slopes, 80°/62° Double-Delta Wing

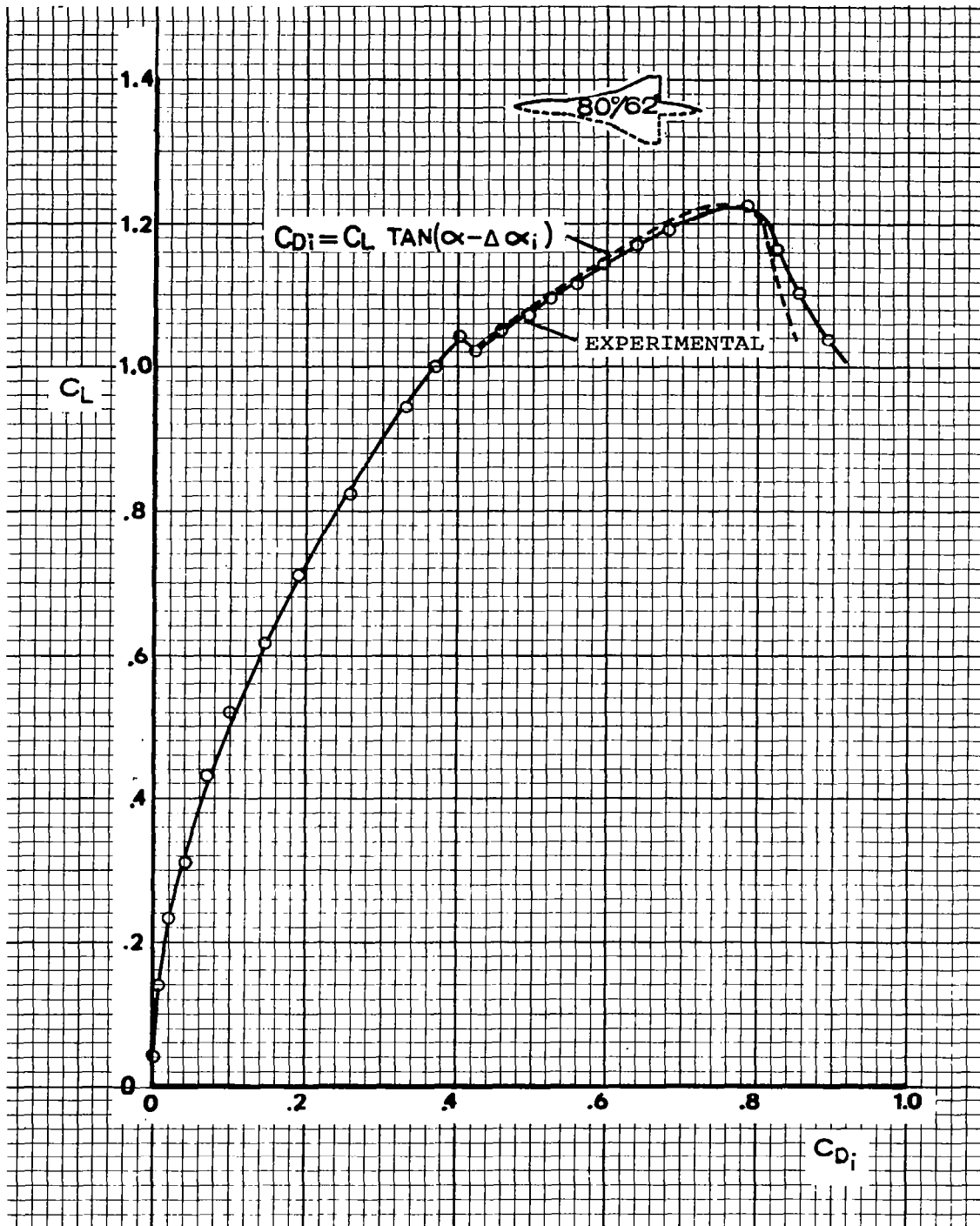
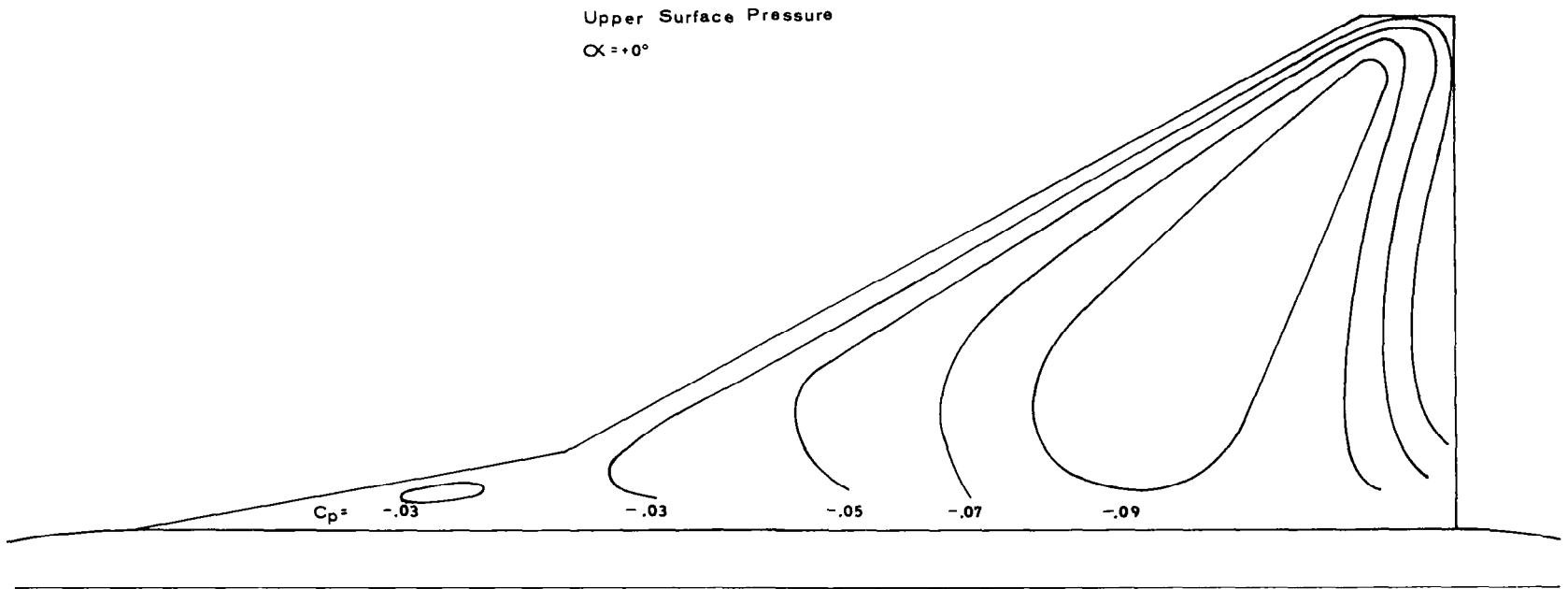


Figure 7e Comparison of Induced Drag with Theory, 80°/62°
 Double-Delta Wing

FIGURE 8a - Pressure Distribution - $\alpha = +0^\circ$

Upper Surface Pressure

$\alpha = +5^\circ$

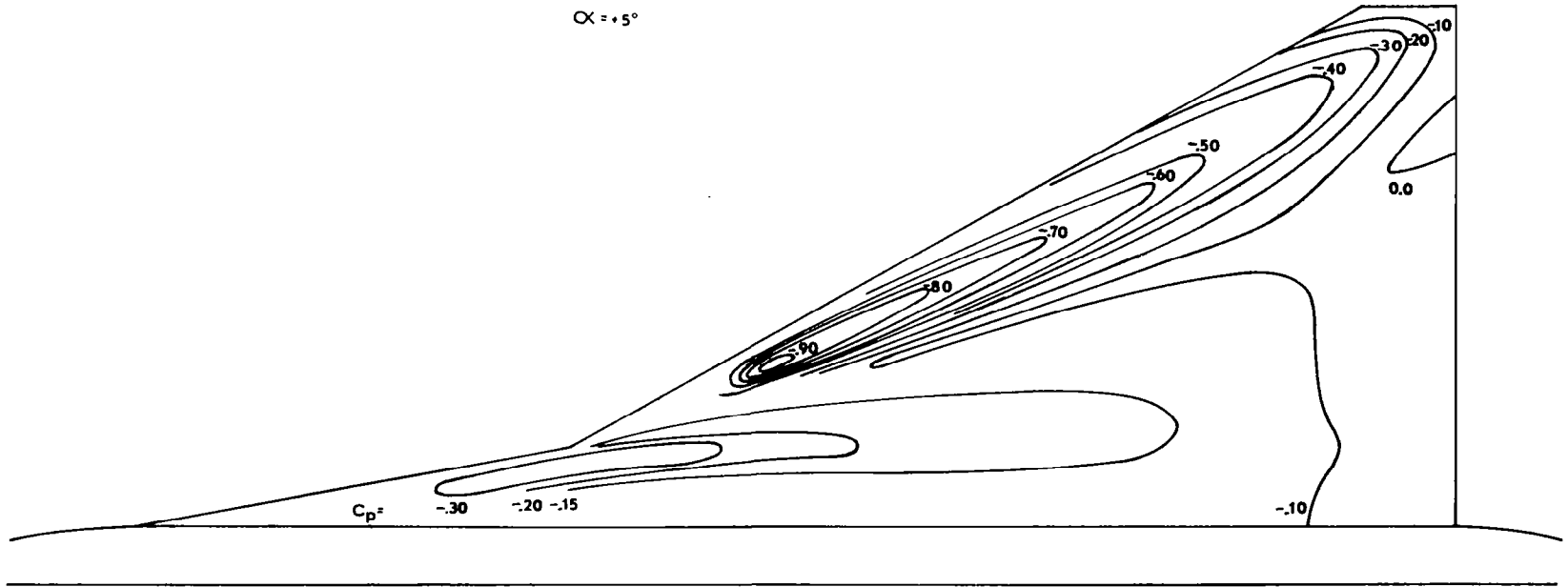


FIGURE 8b - Pressure Distribution - $\alpha = +5^\circ$

Upper Surface Pressure

$\alpha = +10^\circ$

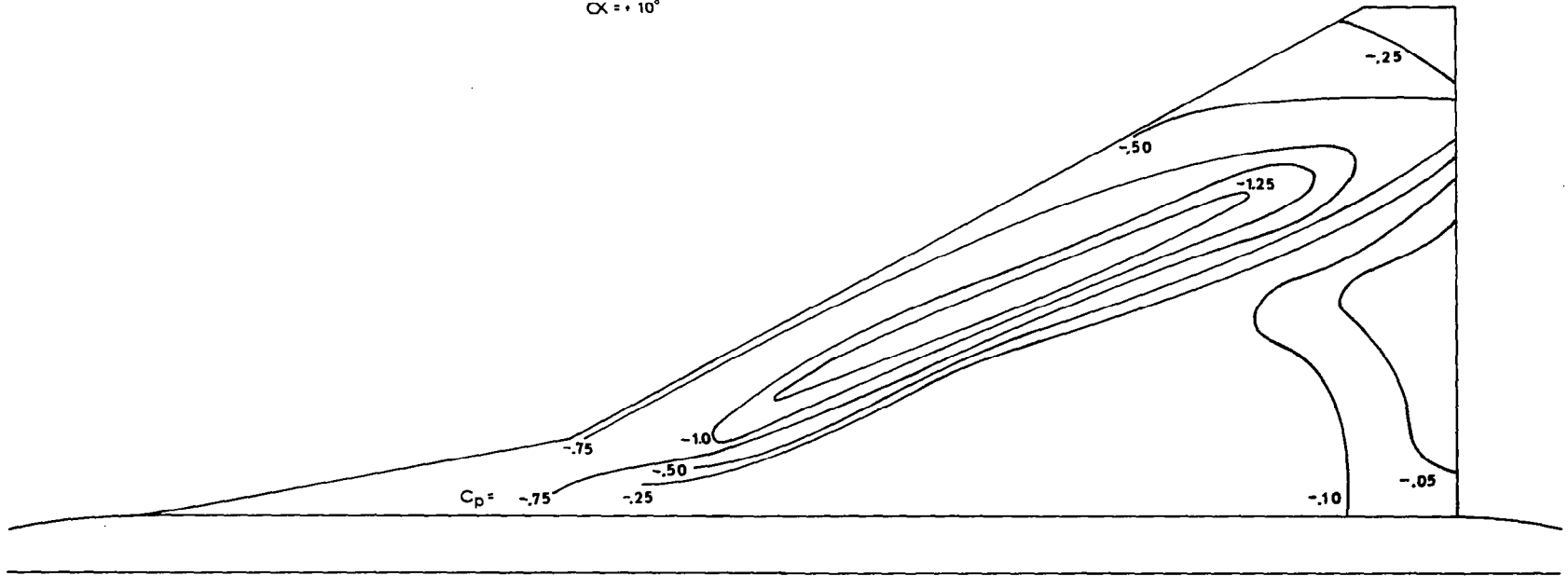


FIGURE 8c - Pressure Distribution - $\alpha = +10^\circ$

Upper Surface Pressure

$\alpha = +15^\circ$

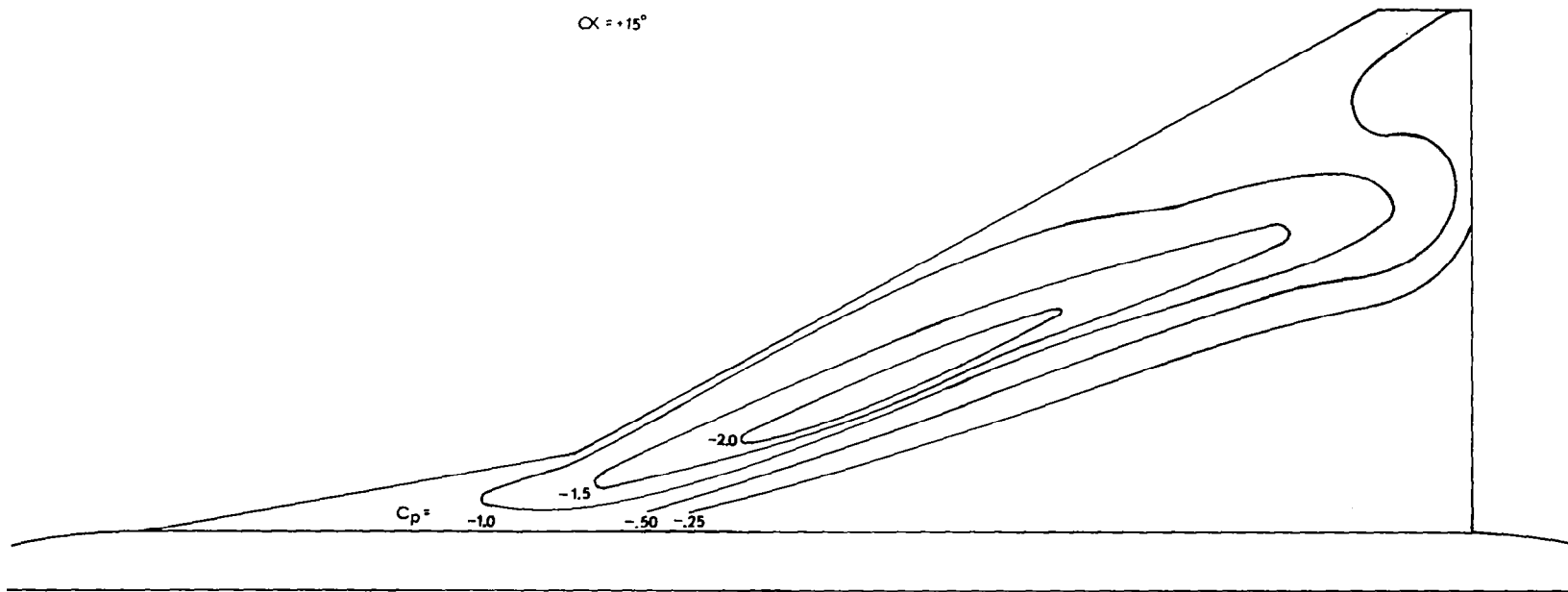


FIGURE 8d - Pressure Distribution - $\alpha = +15^\circ$

Upper Surface Pressure

$\alpha = +20^\circ$

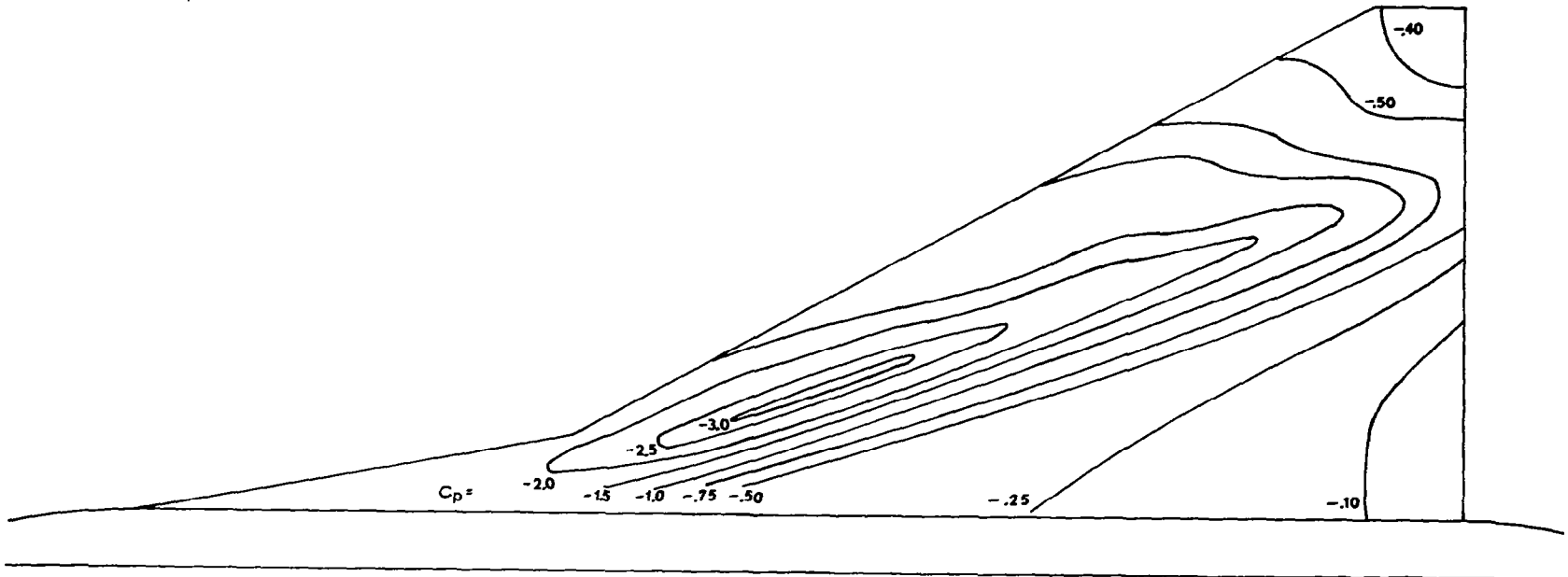


FIGURE 8e- Pressure Distribution - $\alpha = +20^\circ$

Upper Surface Pressure

$\alpha = +25^\circ$

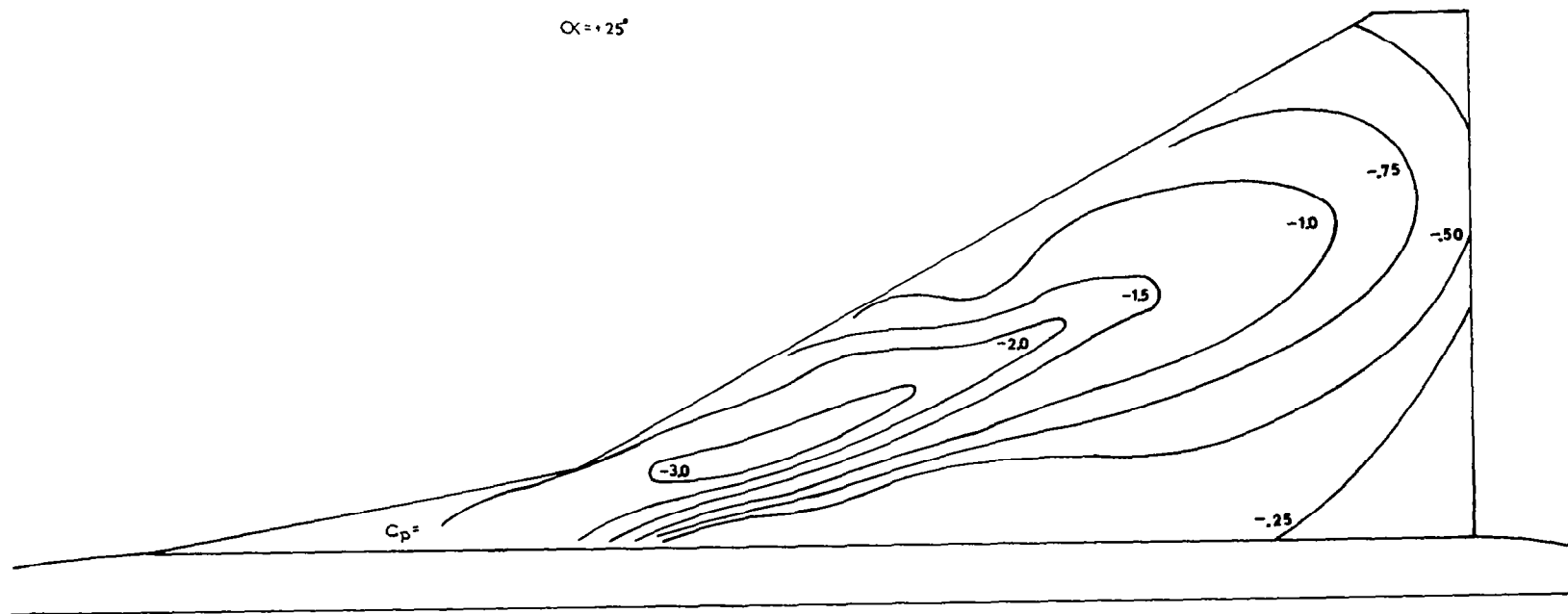


FIGURE 8f - Pressure Distribution - $\alpha = +25^\circ$

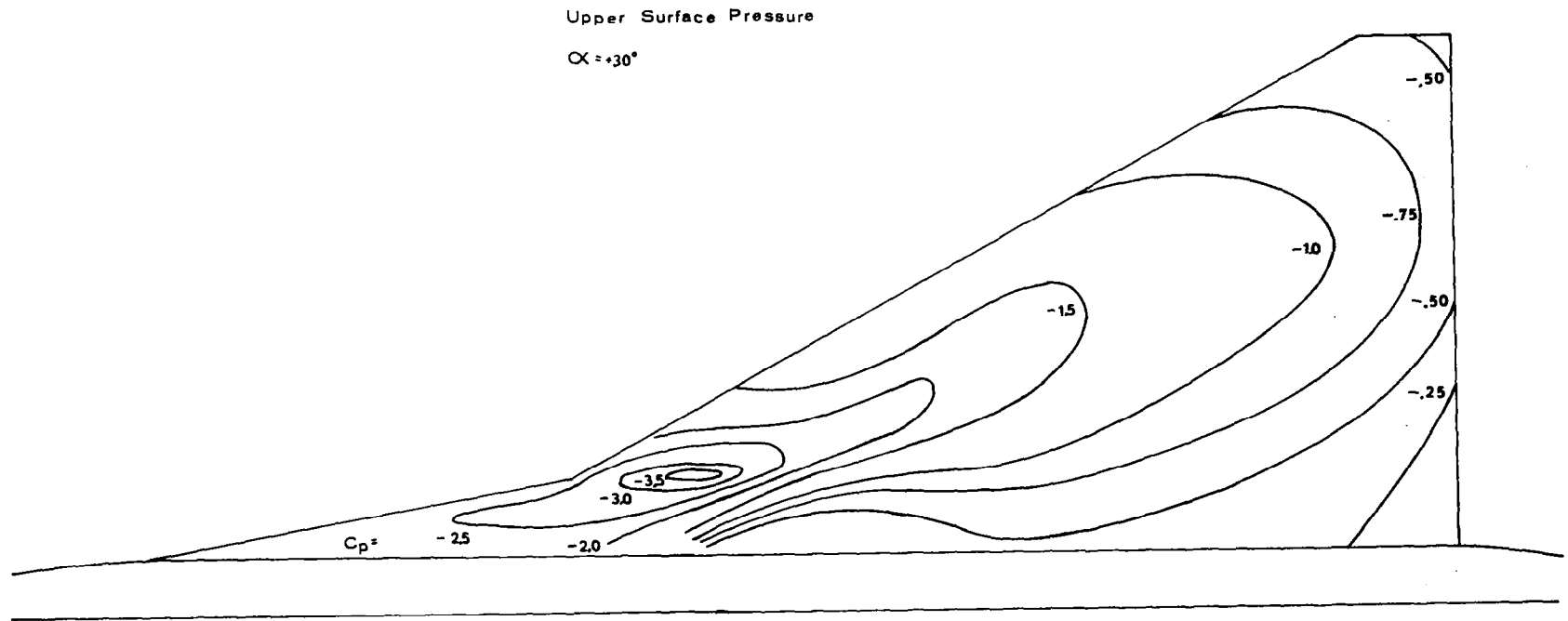


FIGURE 8g - Pressure Distribution - $\alpha = +30^\circ$

Upper Surface Pressure

$\alpha = +35^\circ$

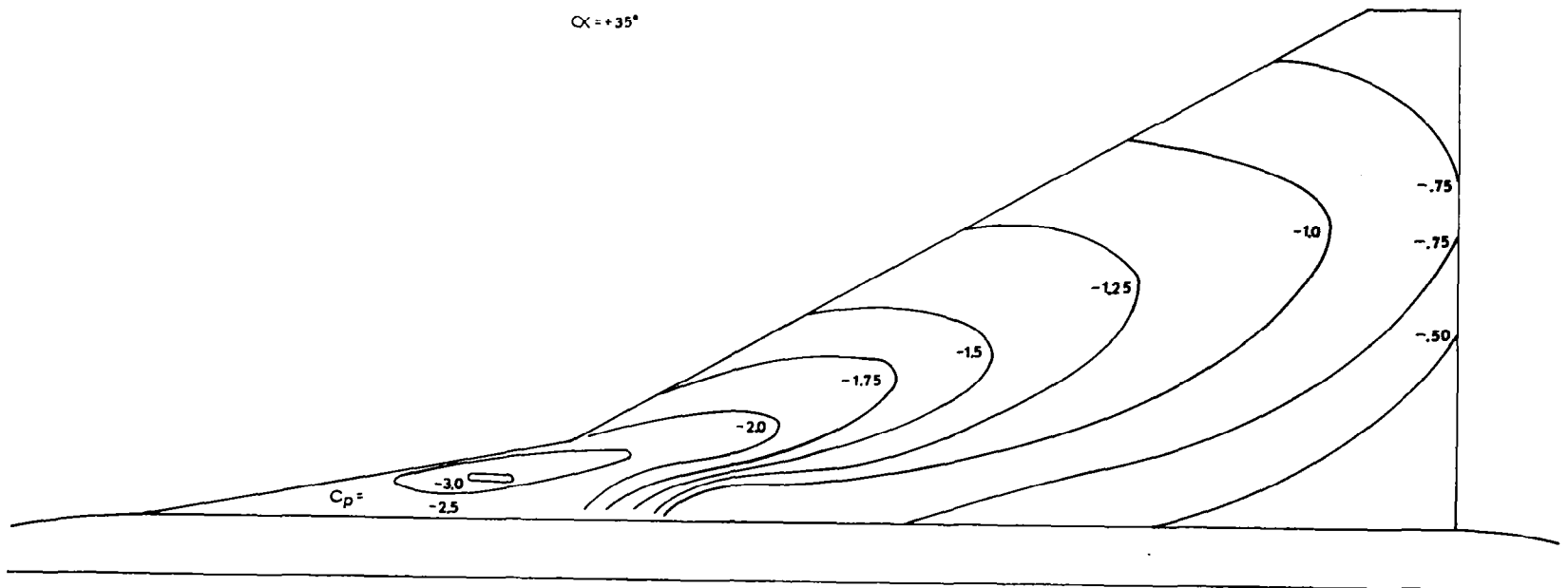


FIGURE 8h- Pressure Distribution - $\alpha = +35^\circ$

Upper Surface Pressure

$\alpha = +40^\circ$

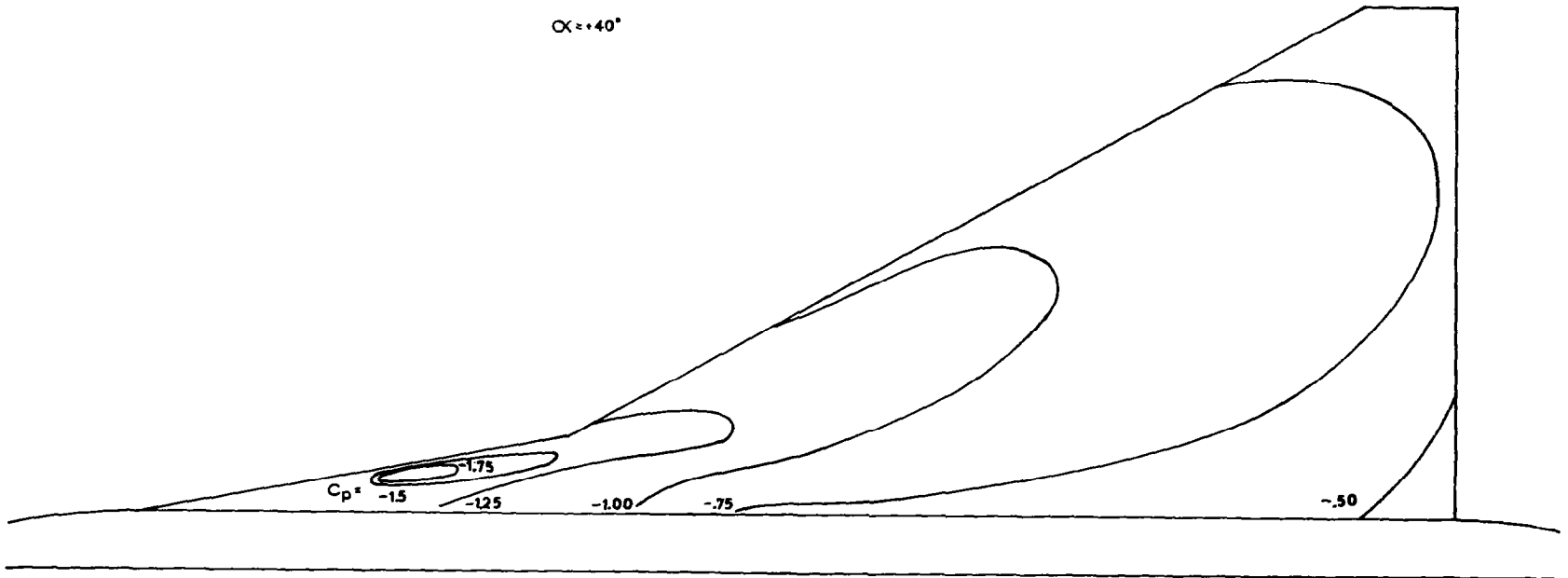


FIGURE 81 - Pressure Distribution - $\alpha = +40^\circ$

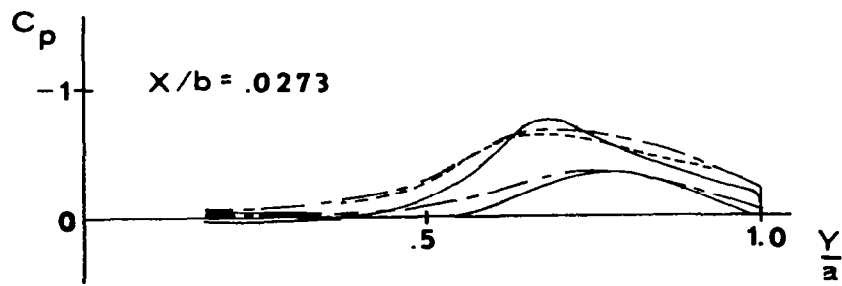
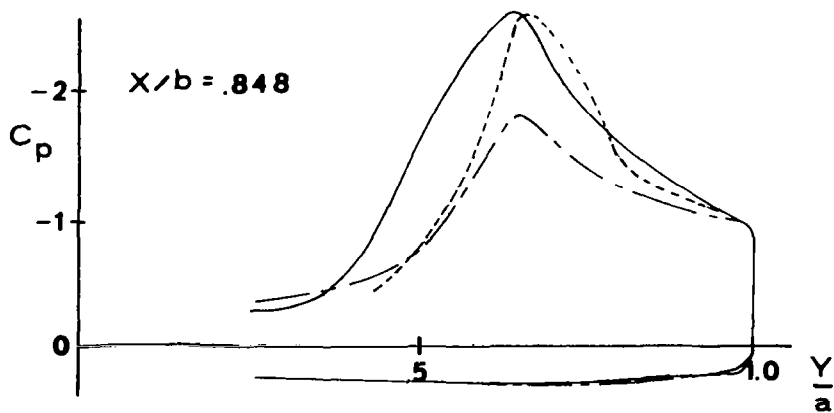
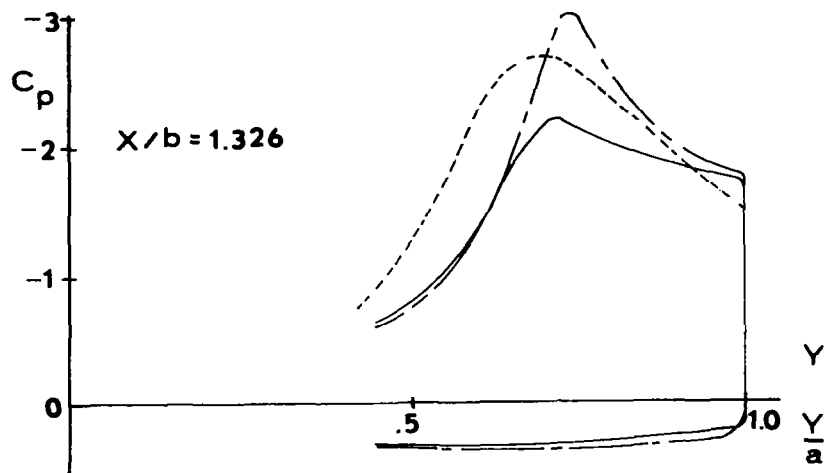
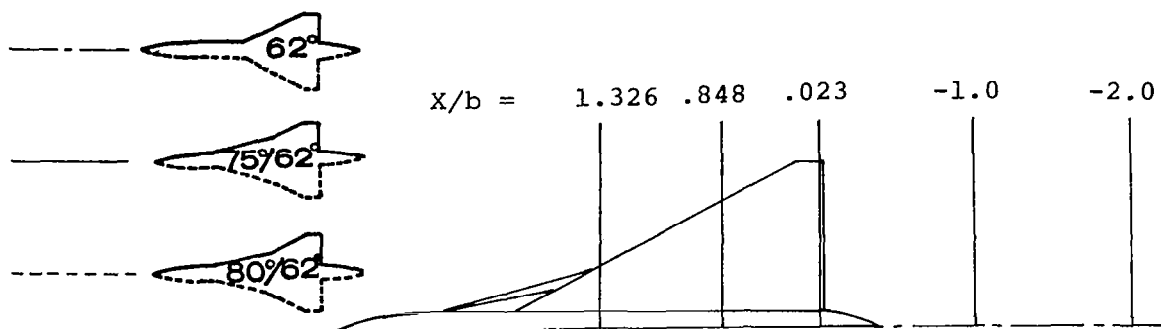


FIGURE 8j Effect Of Strake On Pressure Distribution $\alpha = +20^\circ$ 67

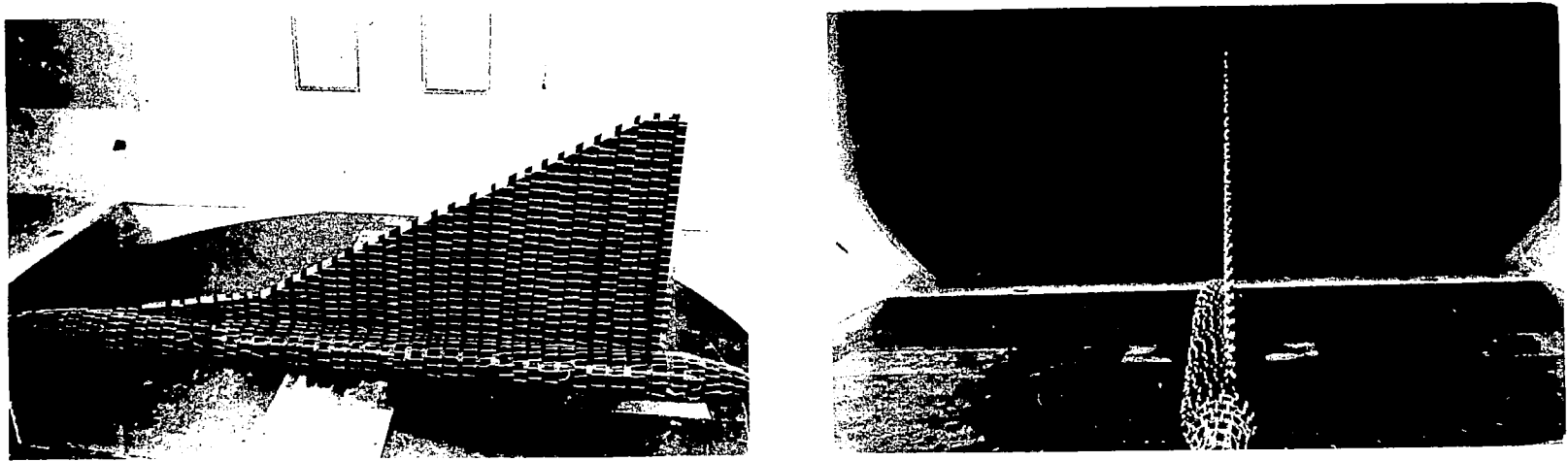


Figure 9a Tuft Pattern $\alpha = 0^\circ$, $80^\circ/62^\circ$ Double-Delta Wing

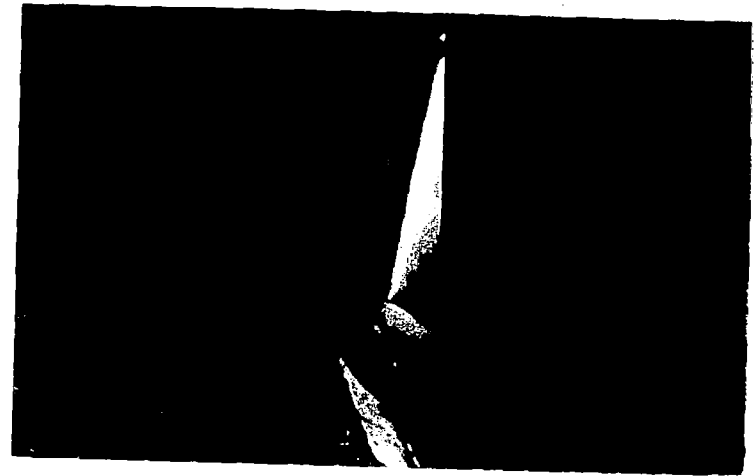
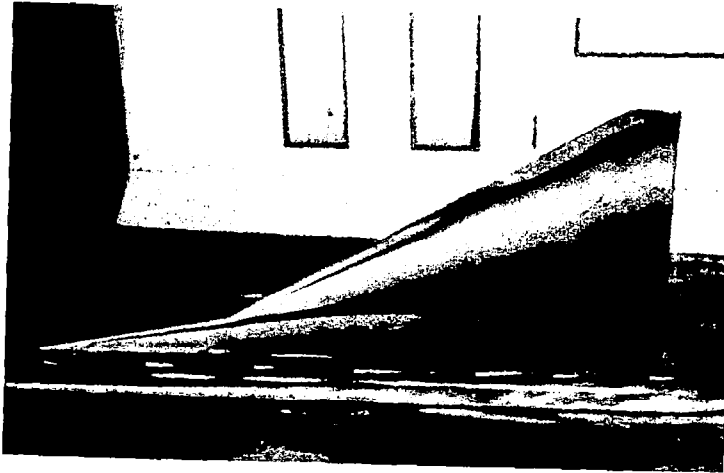
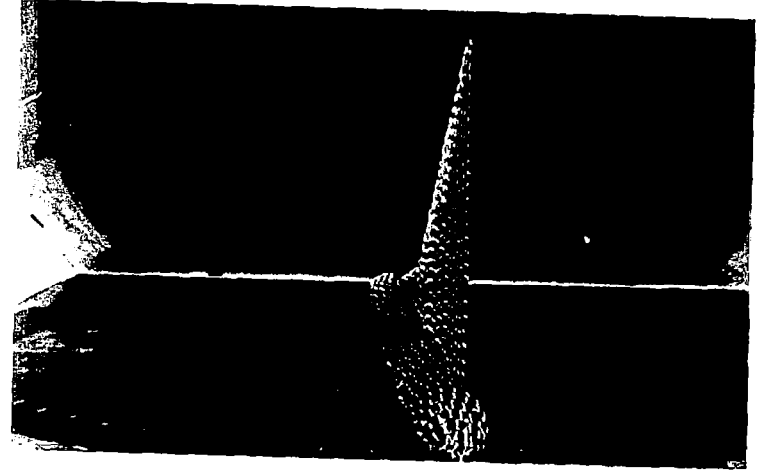
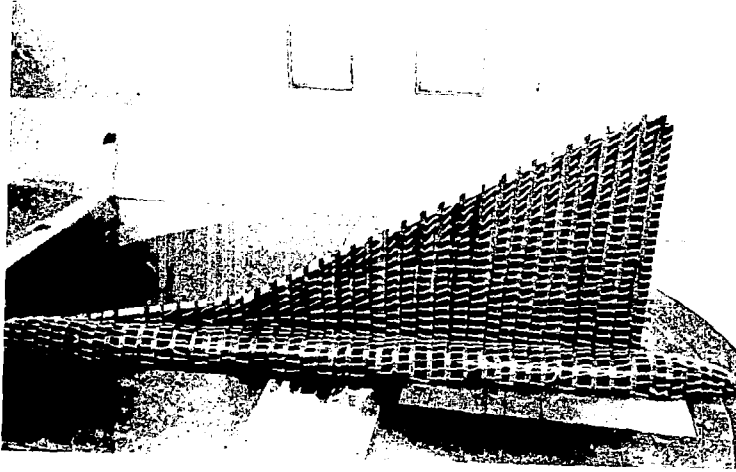


Figure 9b Tuft and Oil Streak Patterns $\alpha = 5^\circ$, $80^\circ/62^\circ$ Double Delta Wing

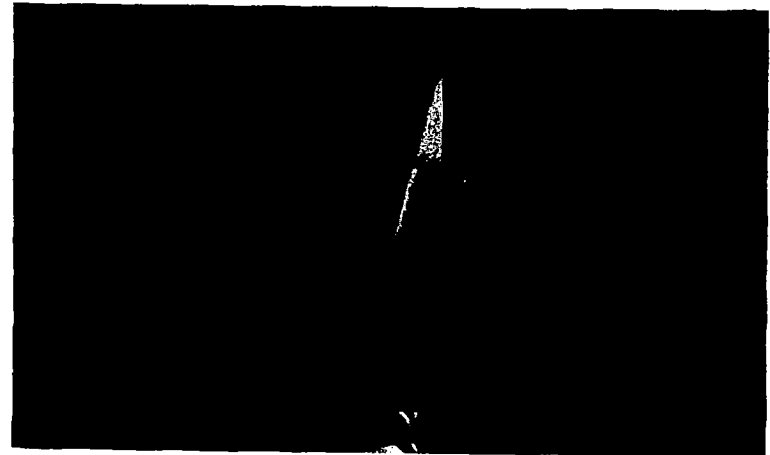
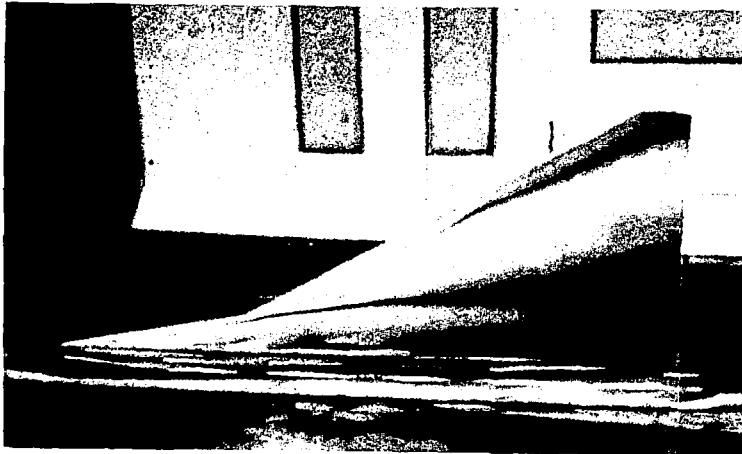
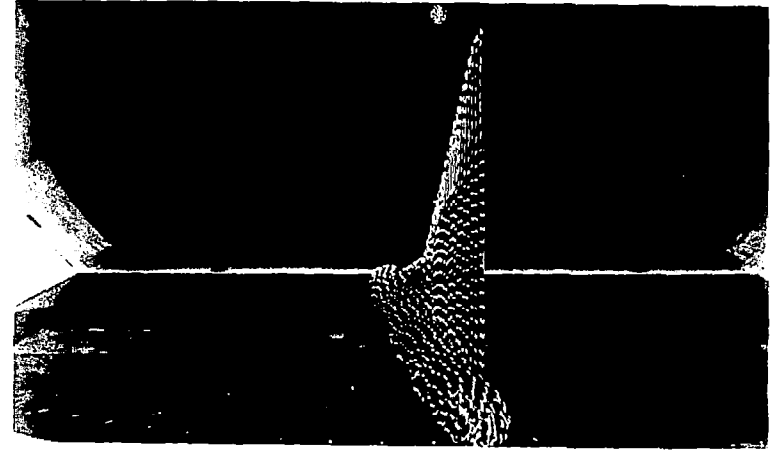
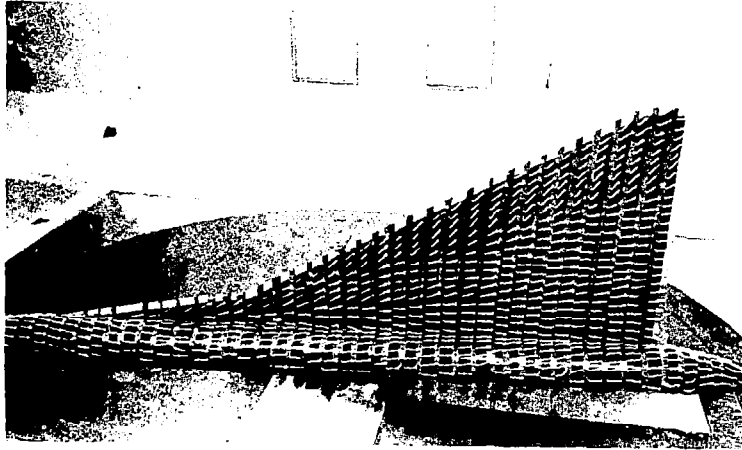


Figure 9c Tuft and Oil Streak Patterns $\alpha = 6^\circ$, $80^\circ/62^\circ$ Double-Delta Wing

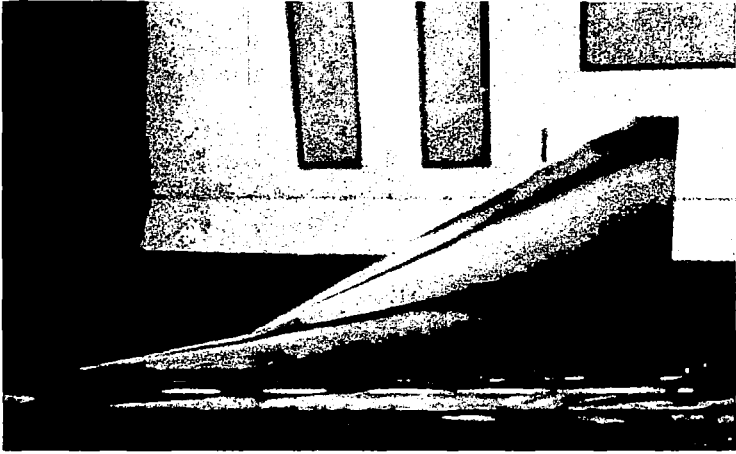


Figure 9d Oil Streak Pattern $\alpha = 6 \frac{1}{2}^\circ$, $80^\circ/62^\circ$ Double-Delta Wing

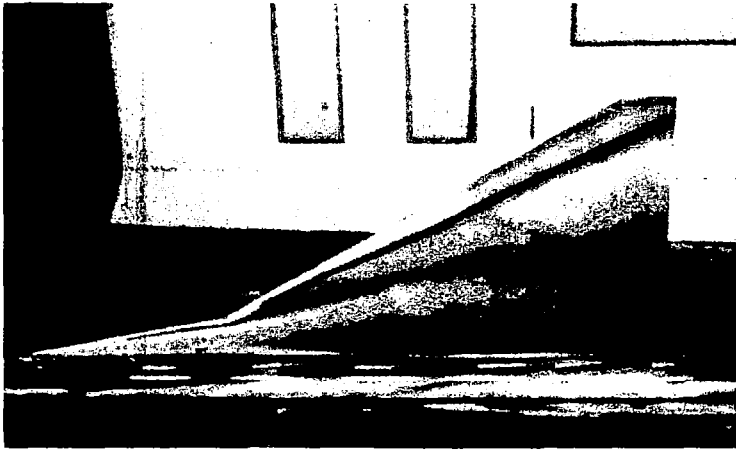
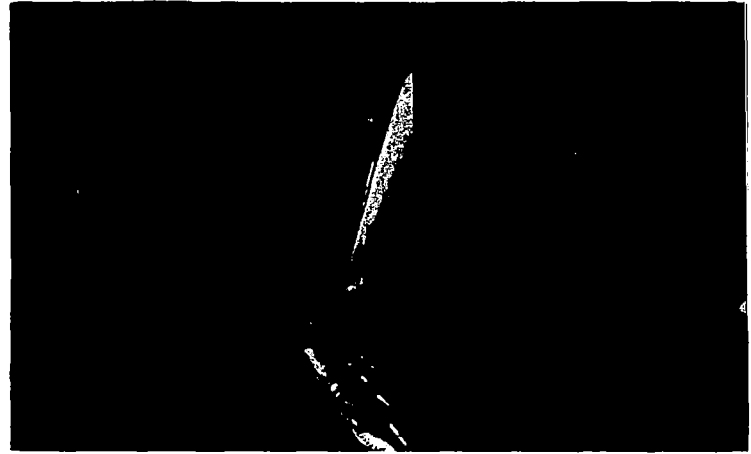


Figure 9e Oil Streak Pattern $\alpha = 7^\circ$, $80^\circ/62^\circ$ Double-Delta Wing



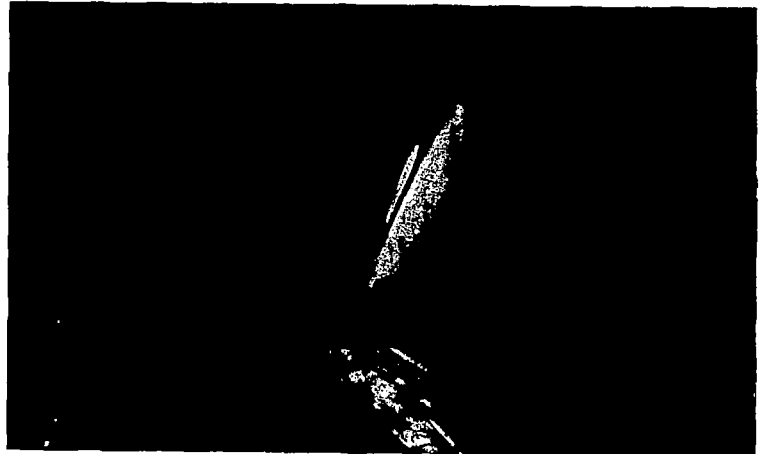
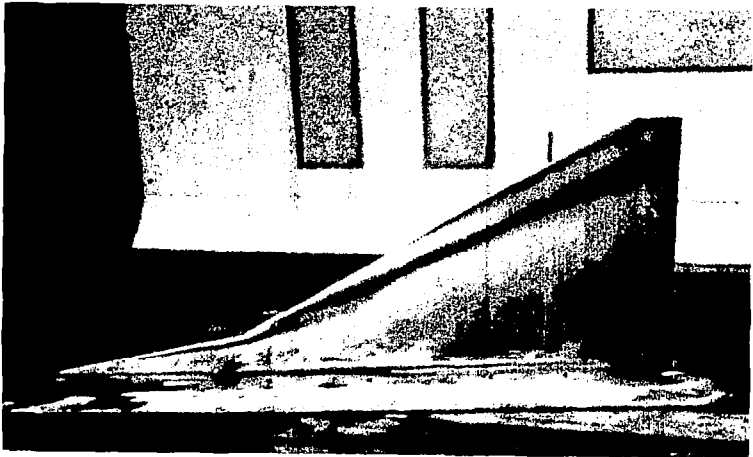
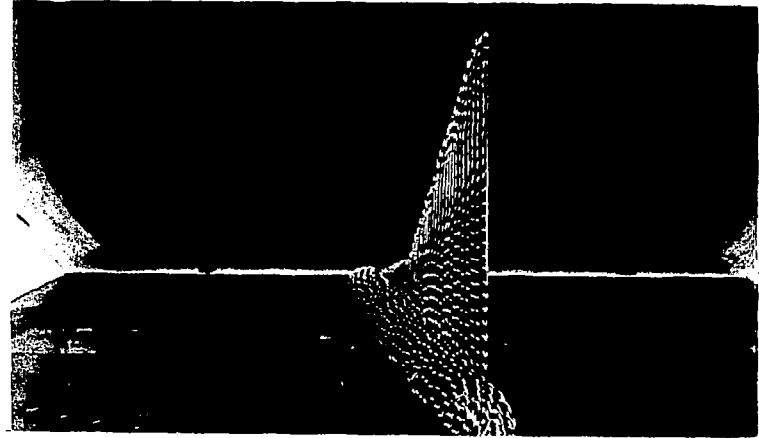
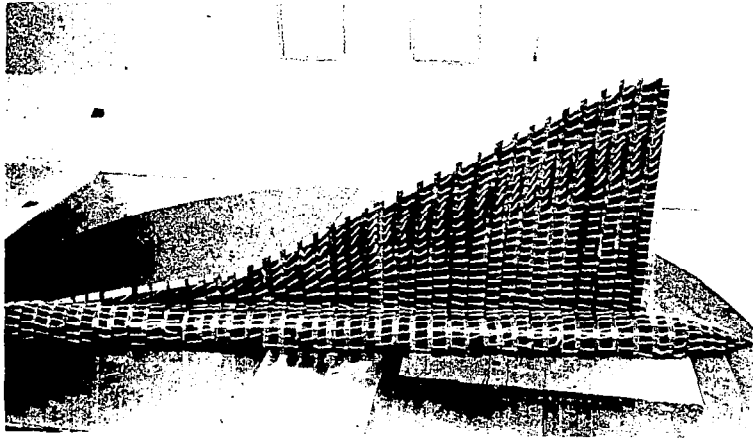


Figure 9f Tuft and Oil Streak Patterns $\alpha = 8^\circ$, $80^\circ/62^\circ$ Double-Delta Wing

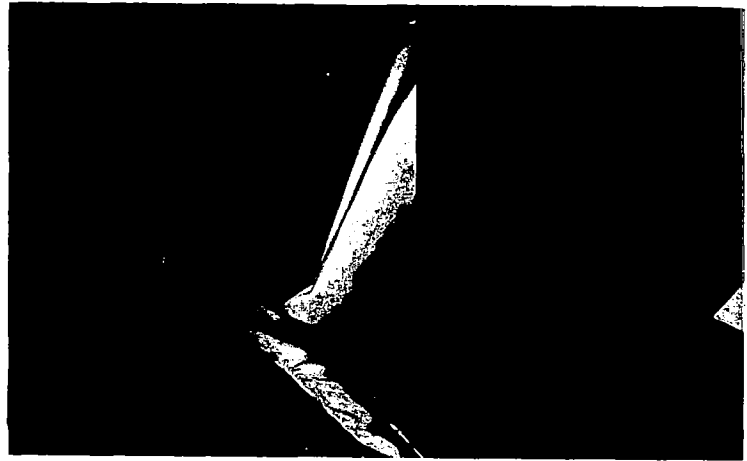
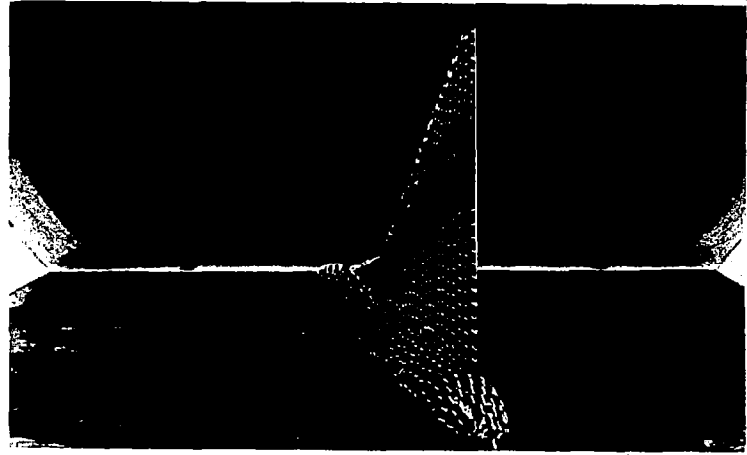
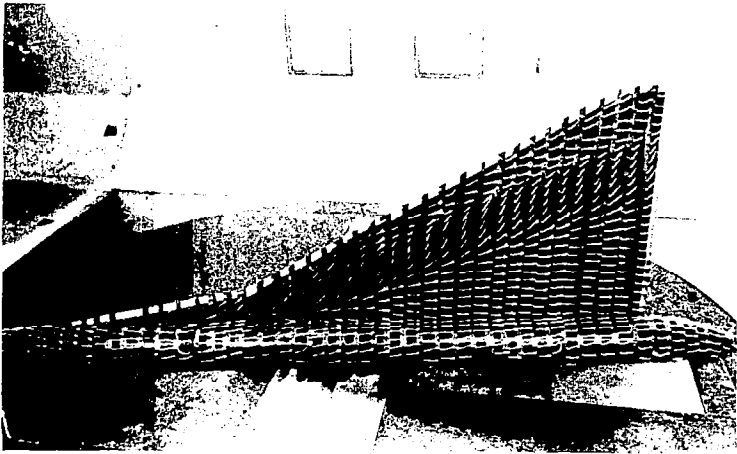


Figure 9g Tuft and Oil Streak Patterns $\alpha = 10^\circ$, $80^\circ/62^\circ$ Double-Delta Wing

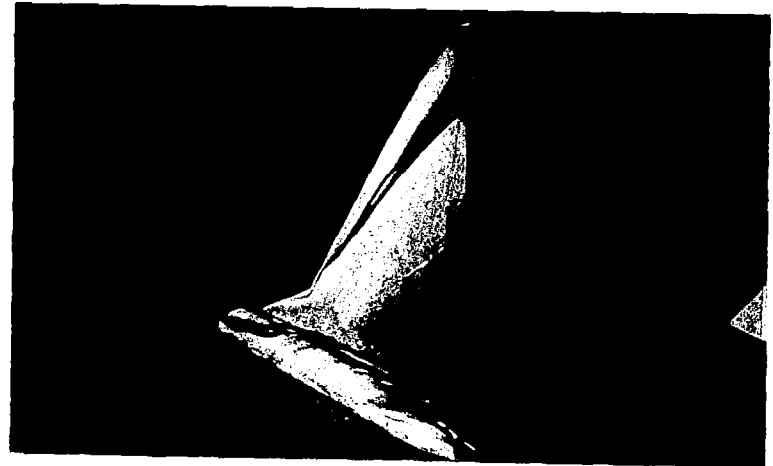
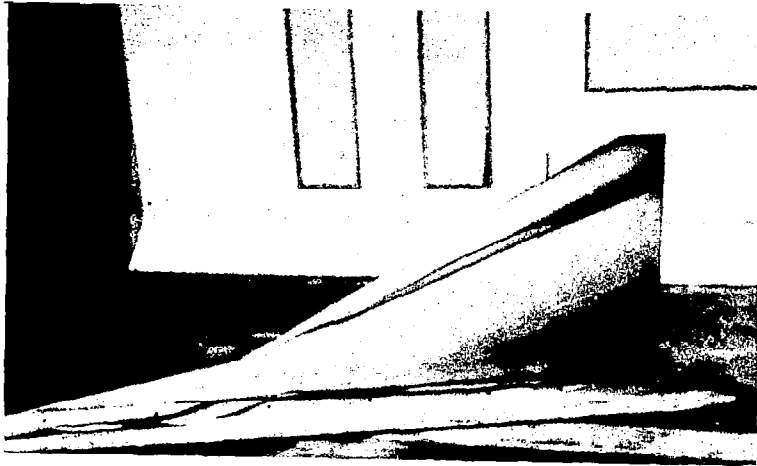
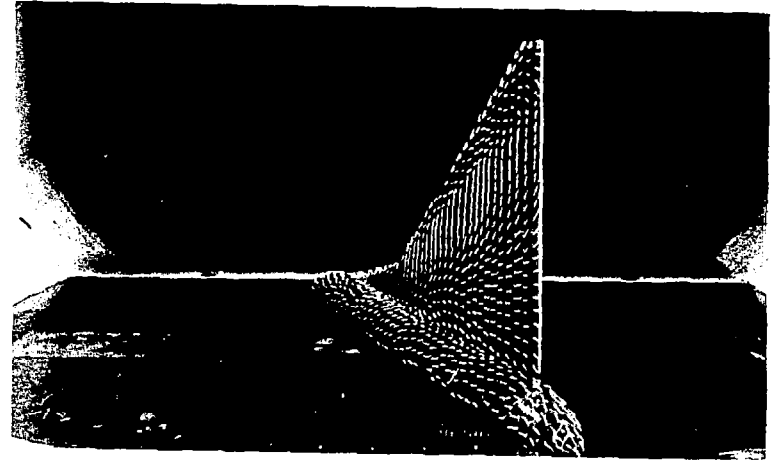
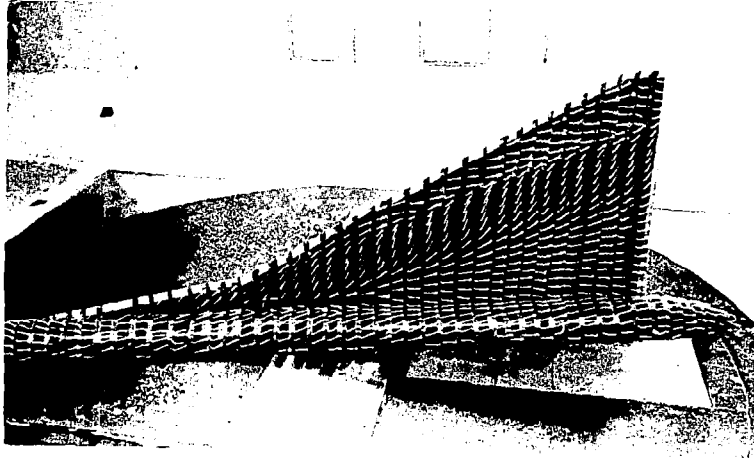


Figure 9h Tuft and Oil Streak Patterns $\alpha = 15^\circ, 80^\circ/62^\circ$ Double-Delta Wing

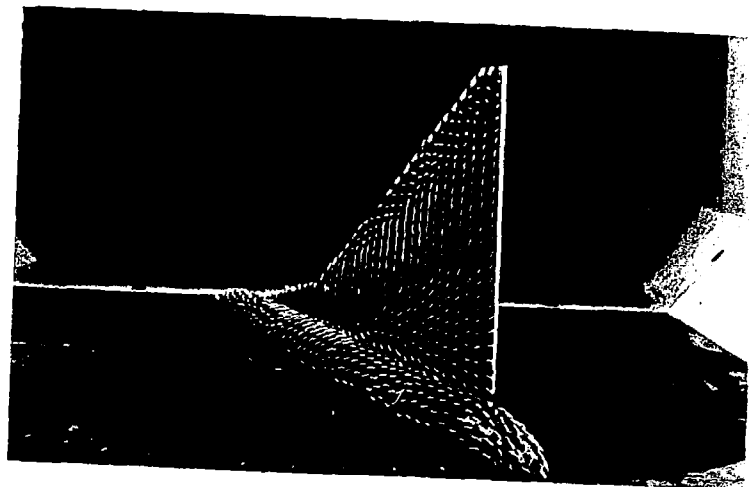
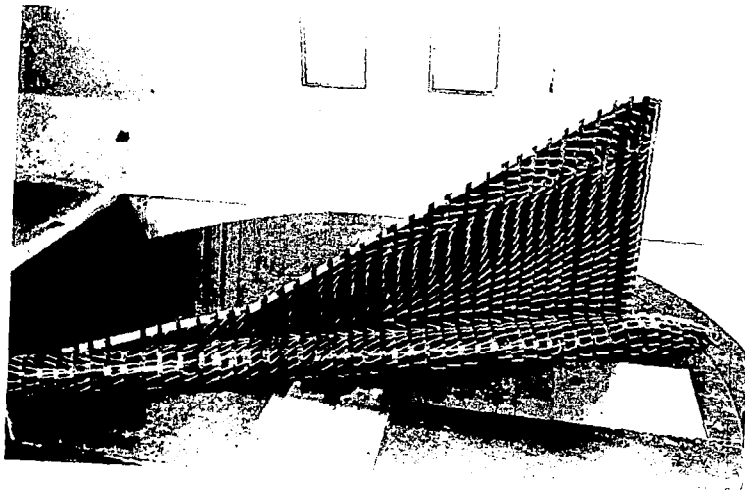


Figure 9i Tuft and Oil Streak Patterns $\alpha = 20^\circ, 80^\circ/62^\circ$ Double-Delta Wing

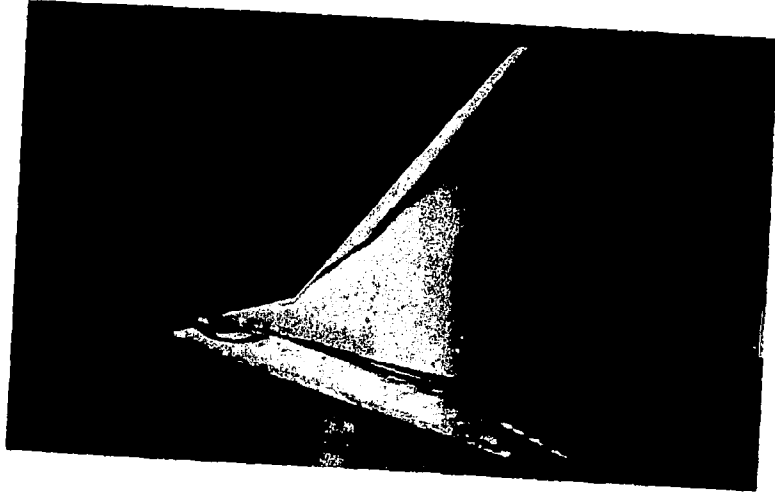
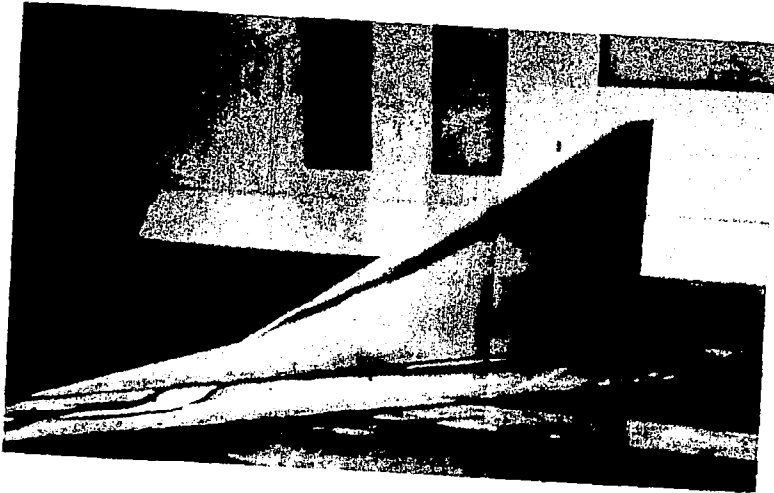
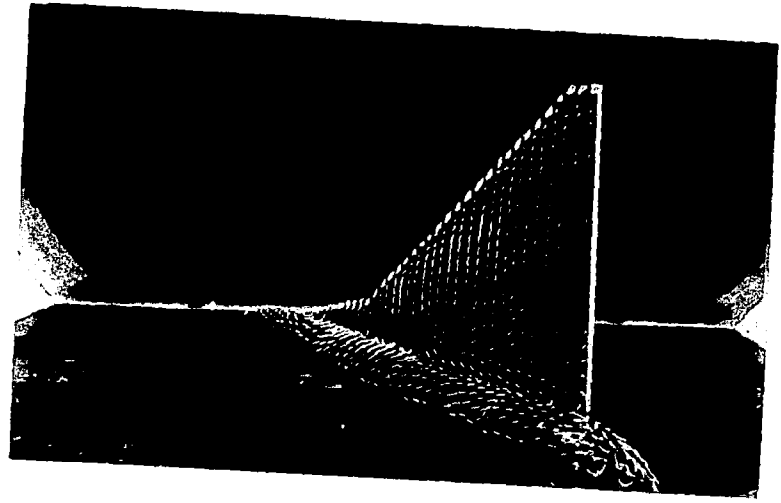
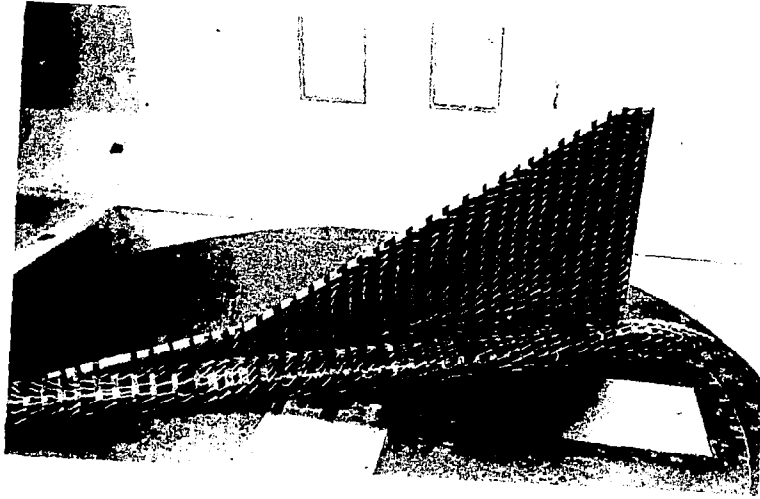


Figure 9j Tuft and Oil Streak Patterns $\alpha = 25^\circ, 80^\circ/62^\circ$ Double-Delta Wing

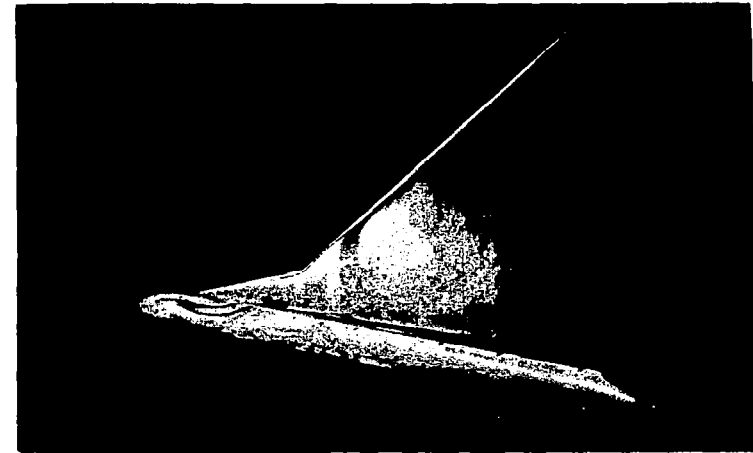
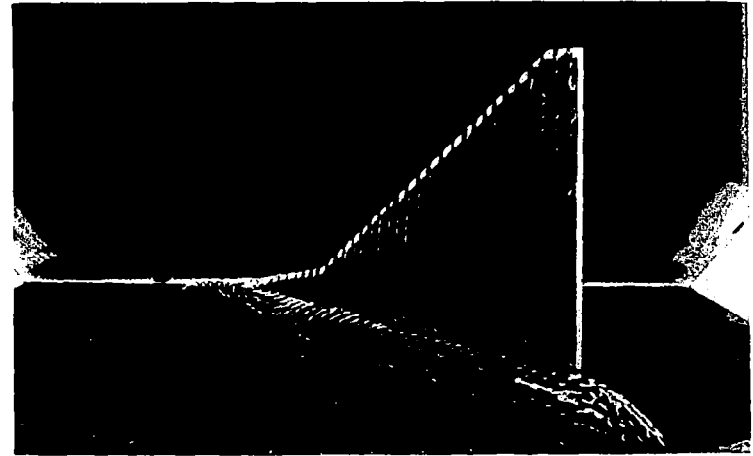
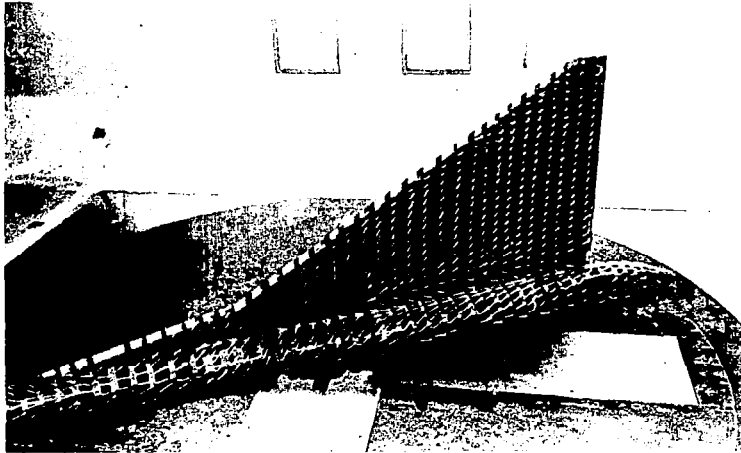


Figure 9k Tuft and Oil Streak Patterns $\alpha = 30^\circ$, $80^\circ/62^\circ$ Double-Delta Wing

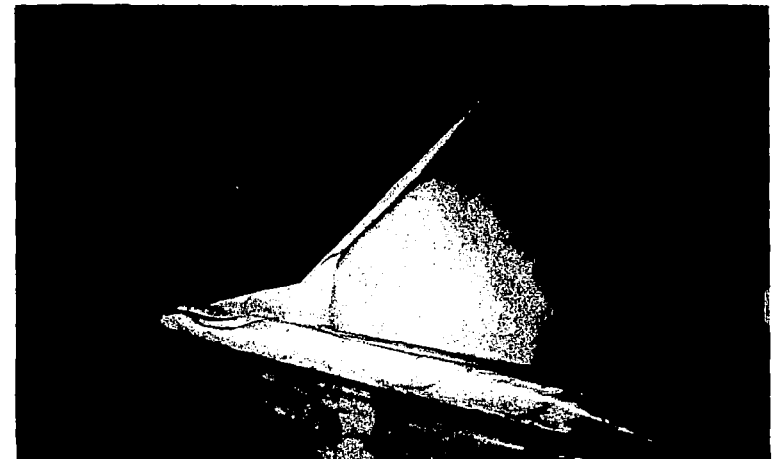
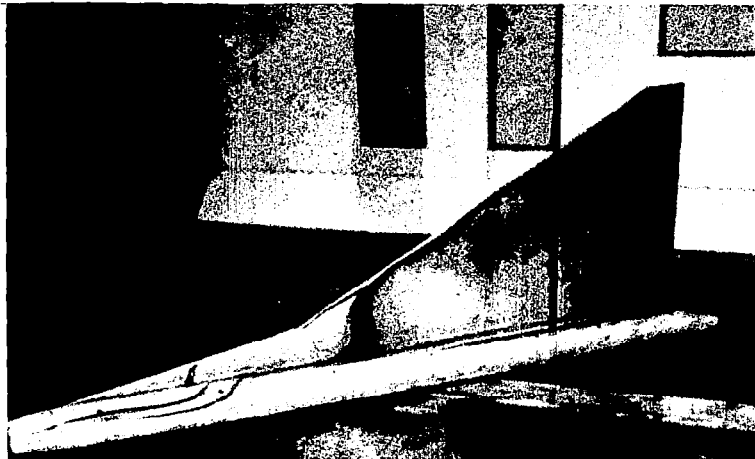
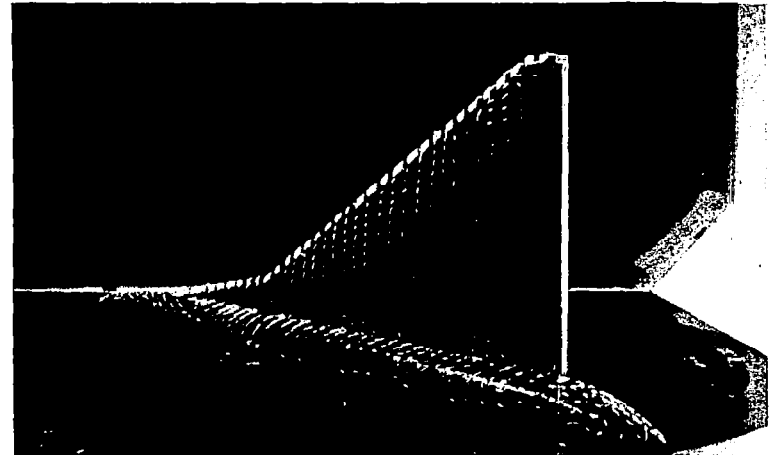
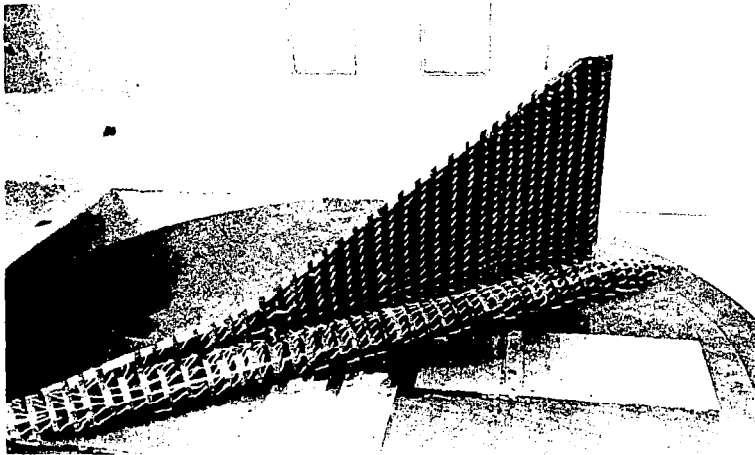


Figure 91 Tuft and Oil Streak Patterns $\alpha = 35^\circ, 80^\circ/62^\circ$ Double-Delta Wing

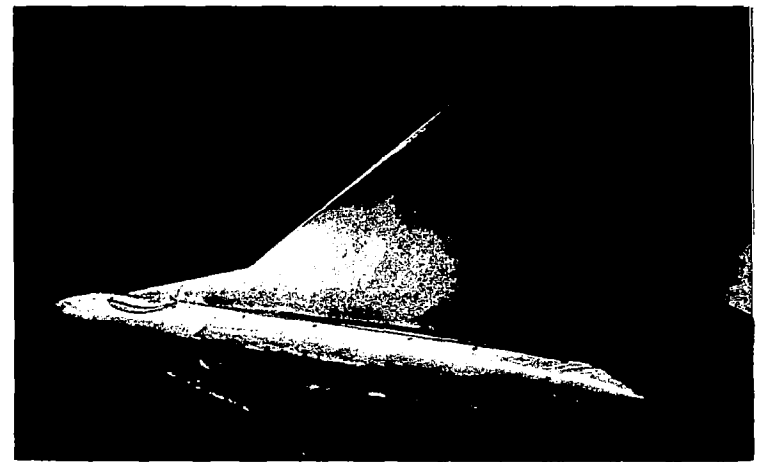
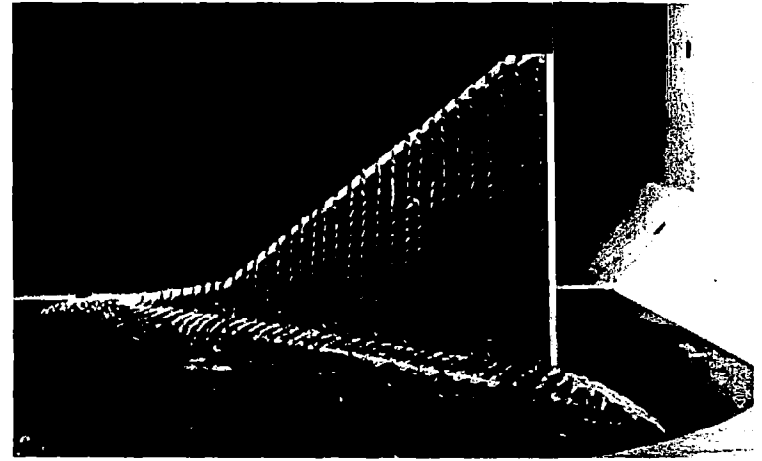
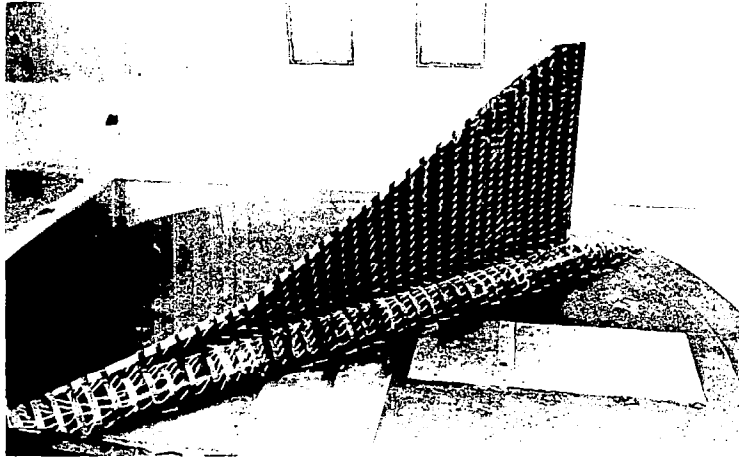
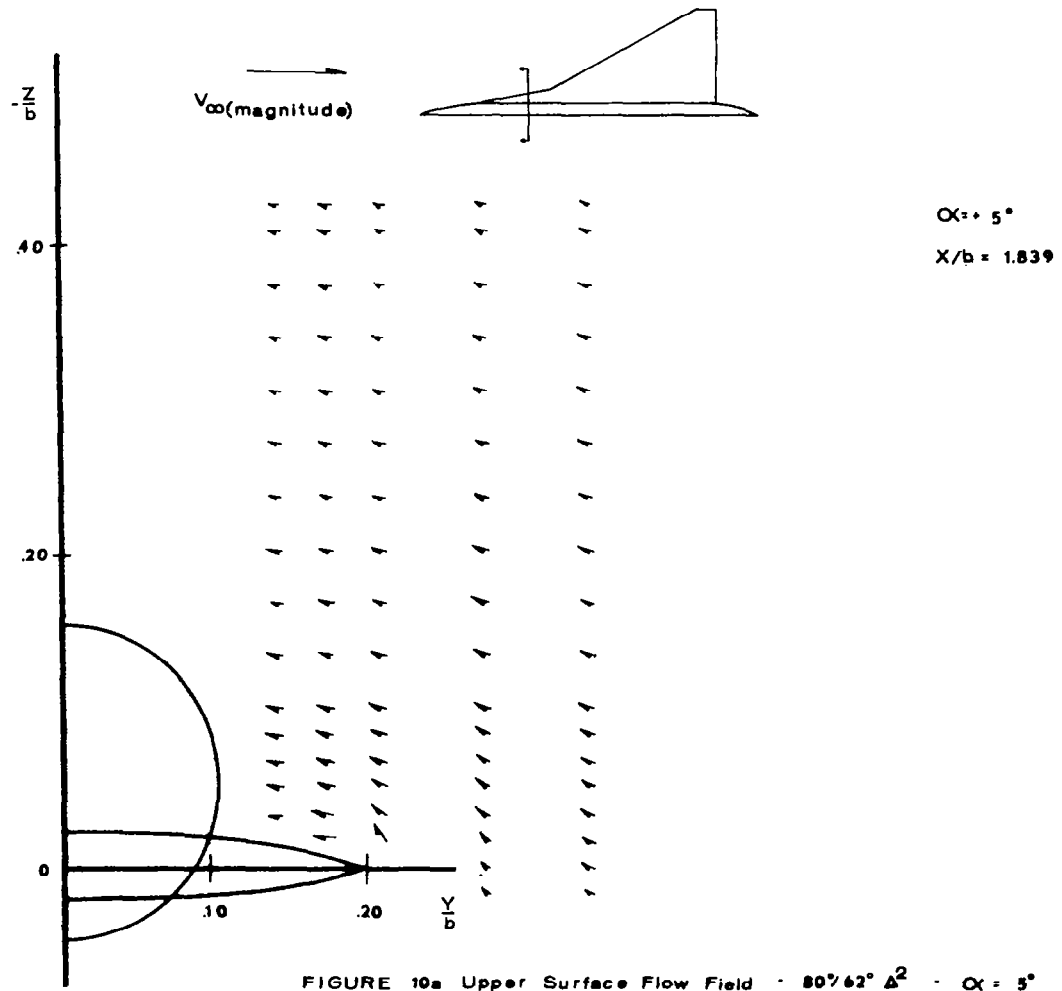


Figure 9m Tuft and Oil Streak Patterns $\alpha = 40^\circ, 80^\circ/62^\circ$ Double-Delta Wing



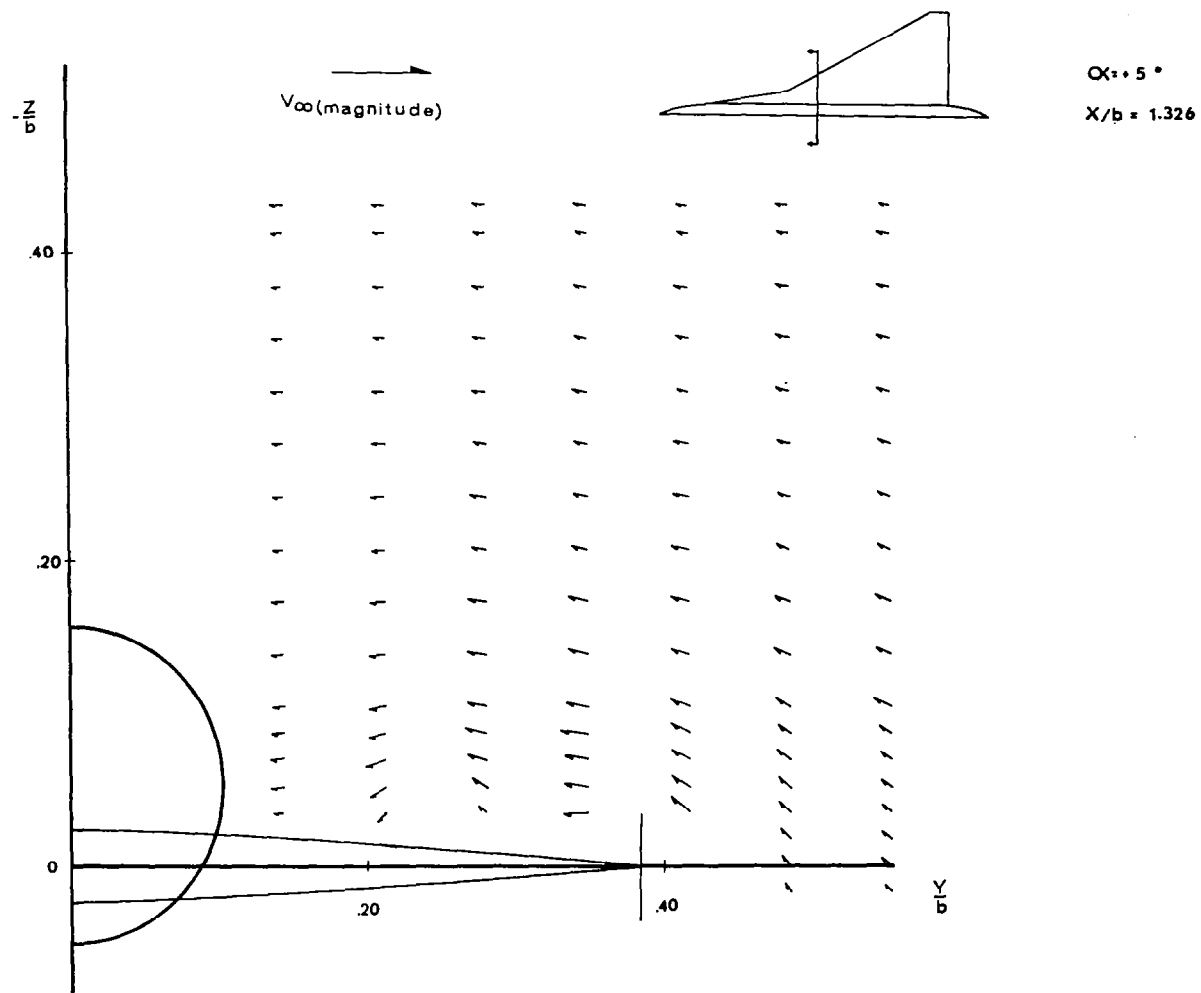
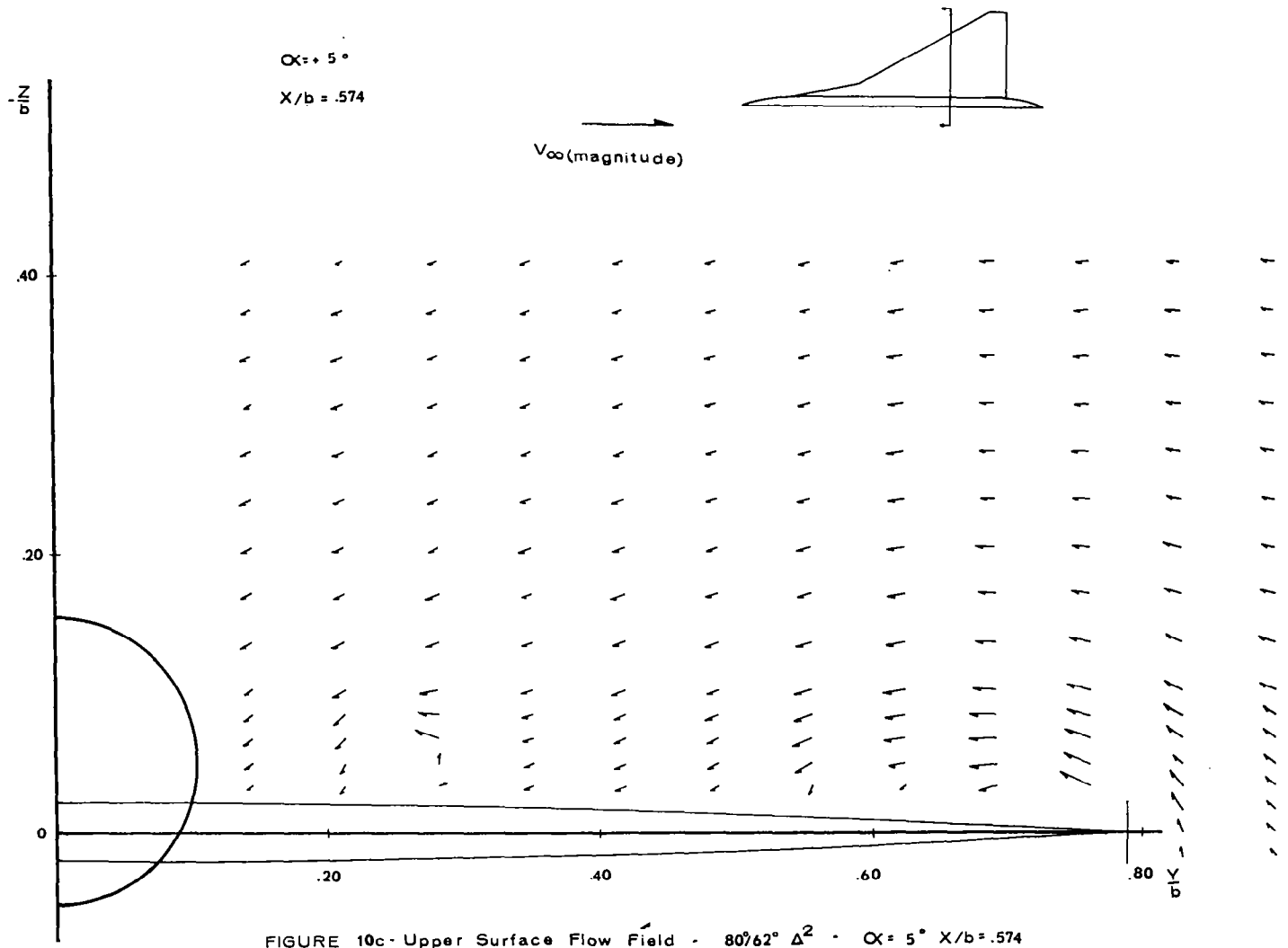


FIGURE 10b- Upper Surface Flow Field - $80\% \Delta^2$ - $\alpha = 5^\circ$ $X/b = 1.326$



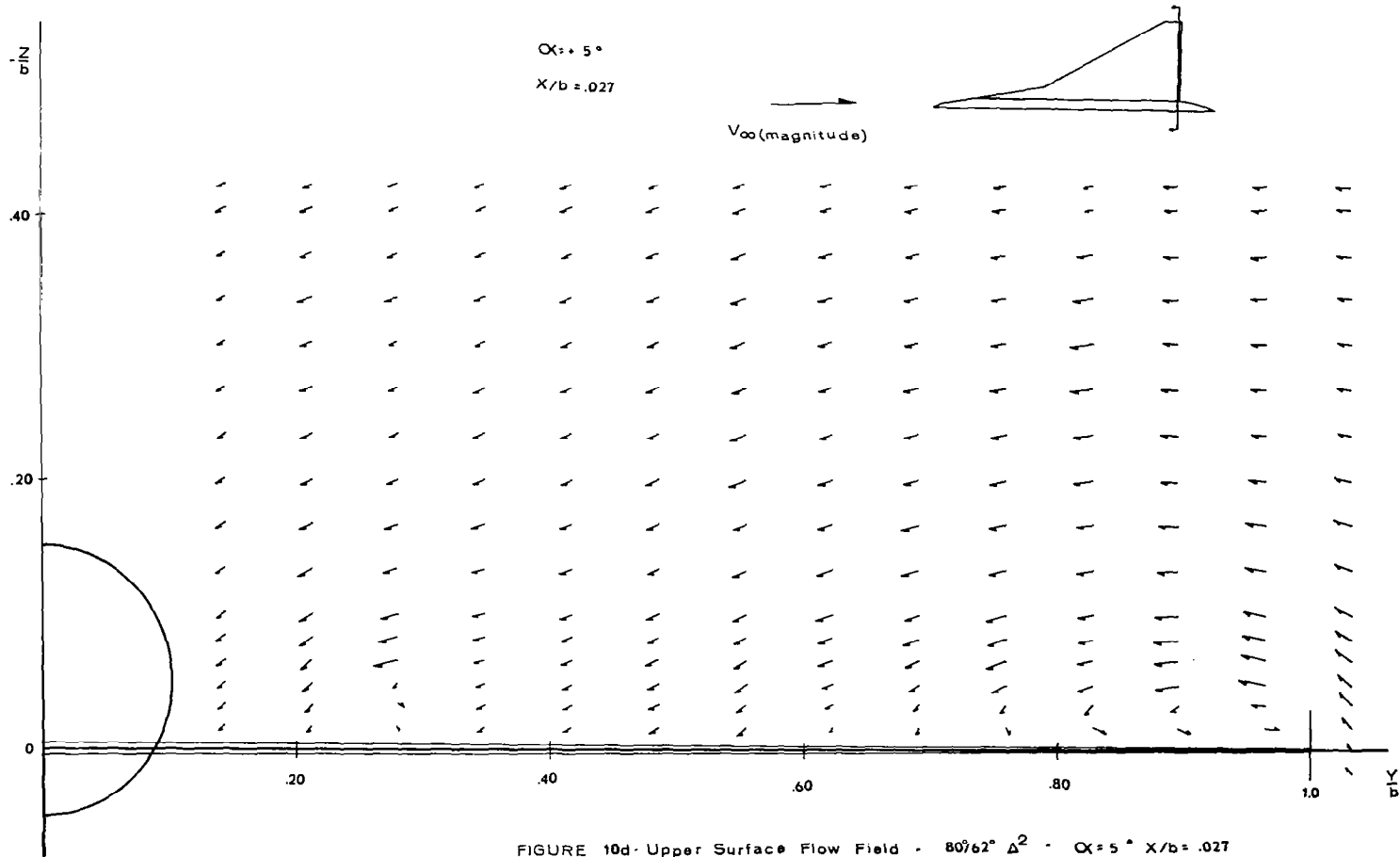
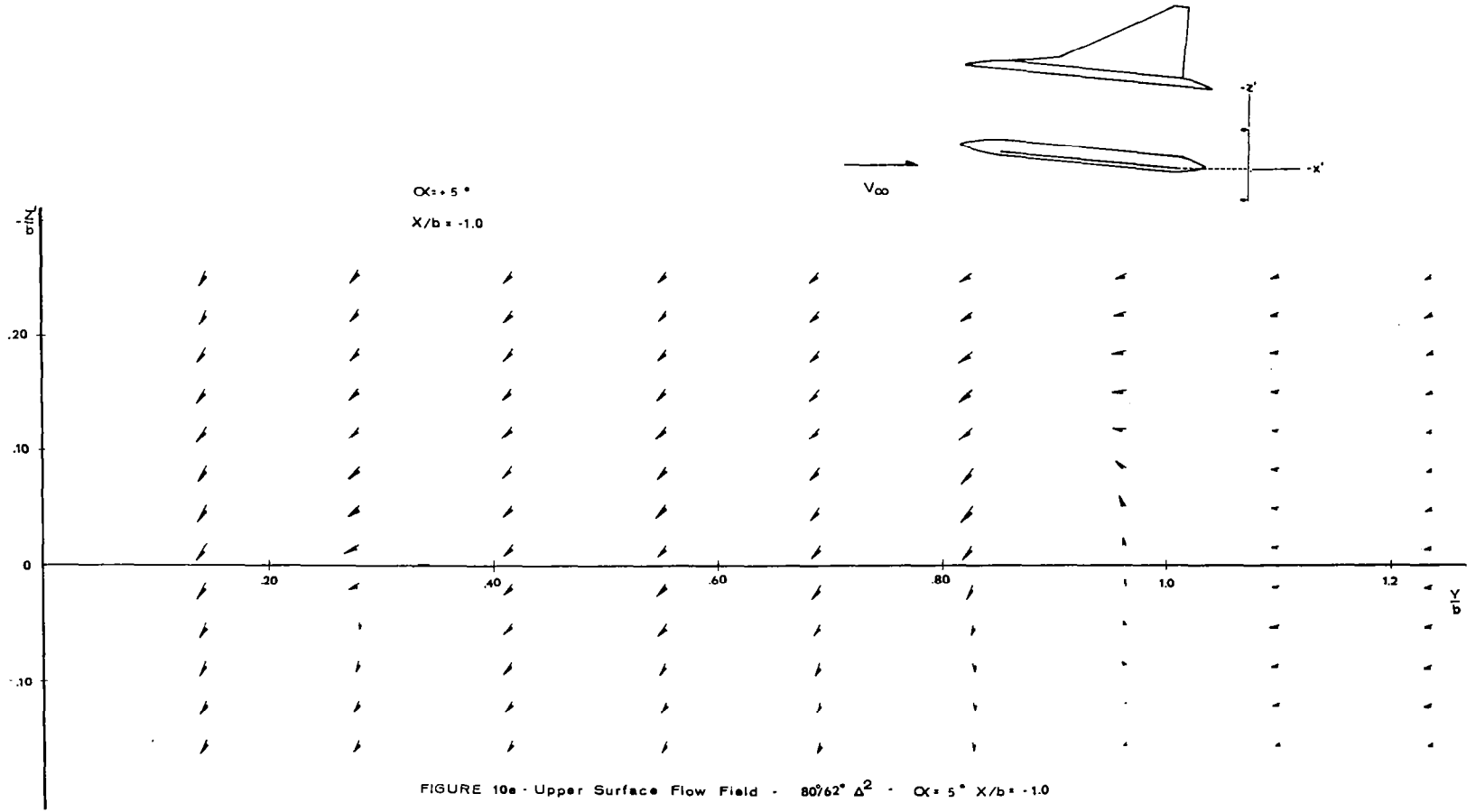


FIGURE 10d - Upper Surface Flow Field - $80^\circ/62^\circ \Delta^2$ - $\alpha = 5^\circ$ $X/b = .027$



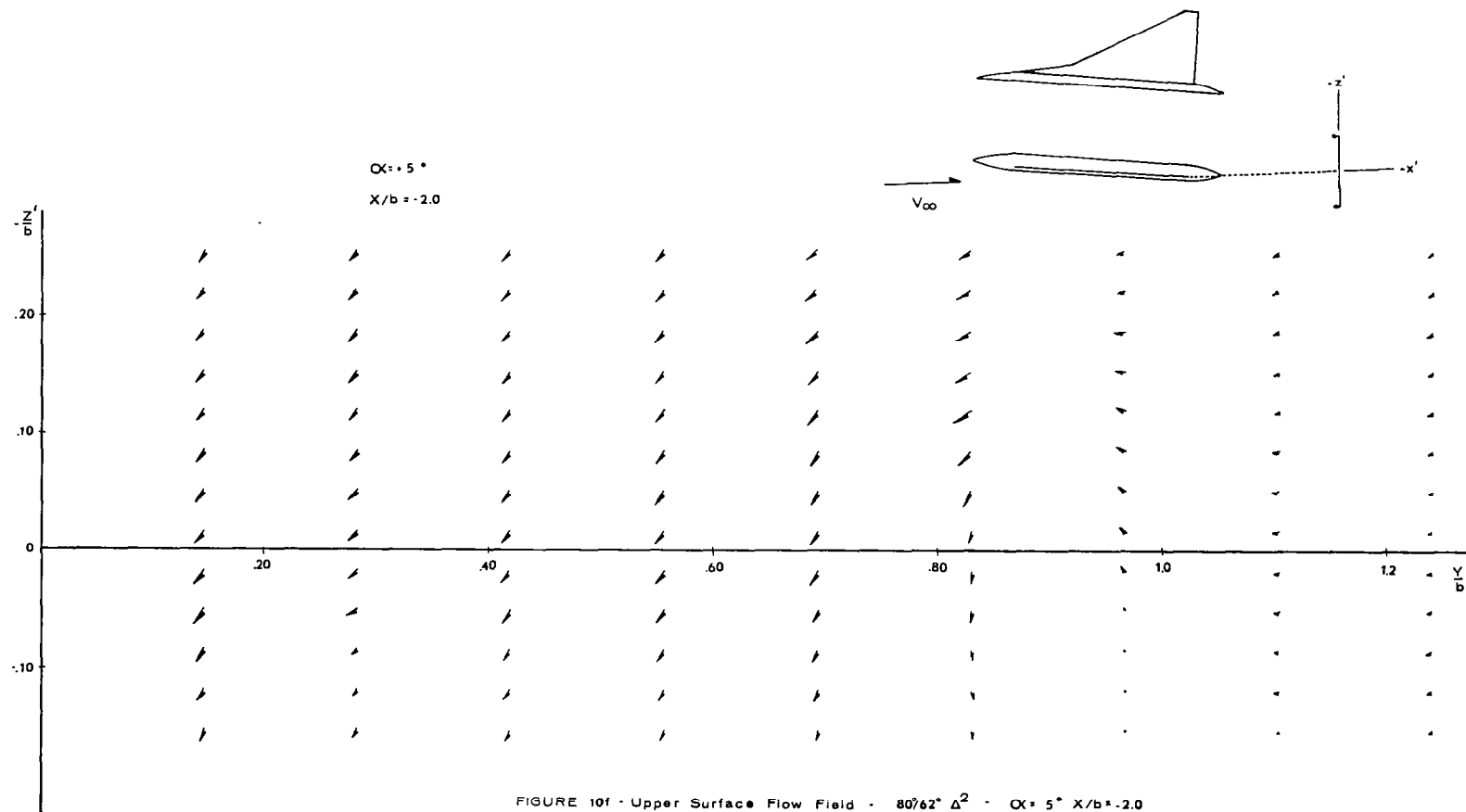
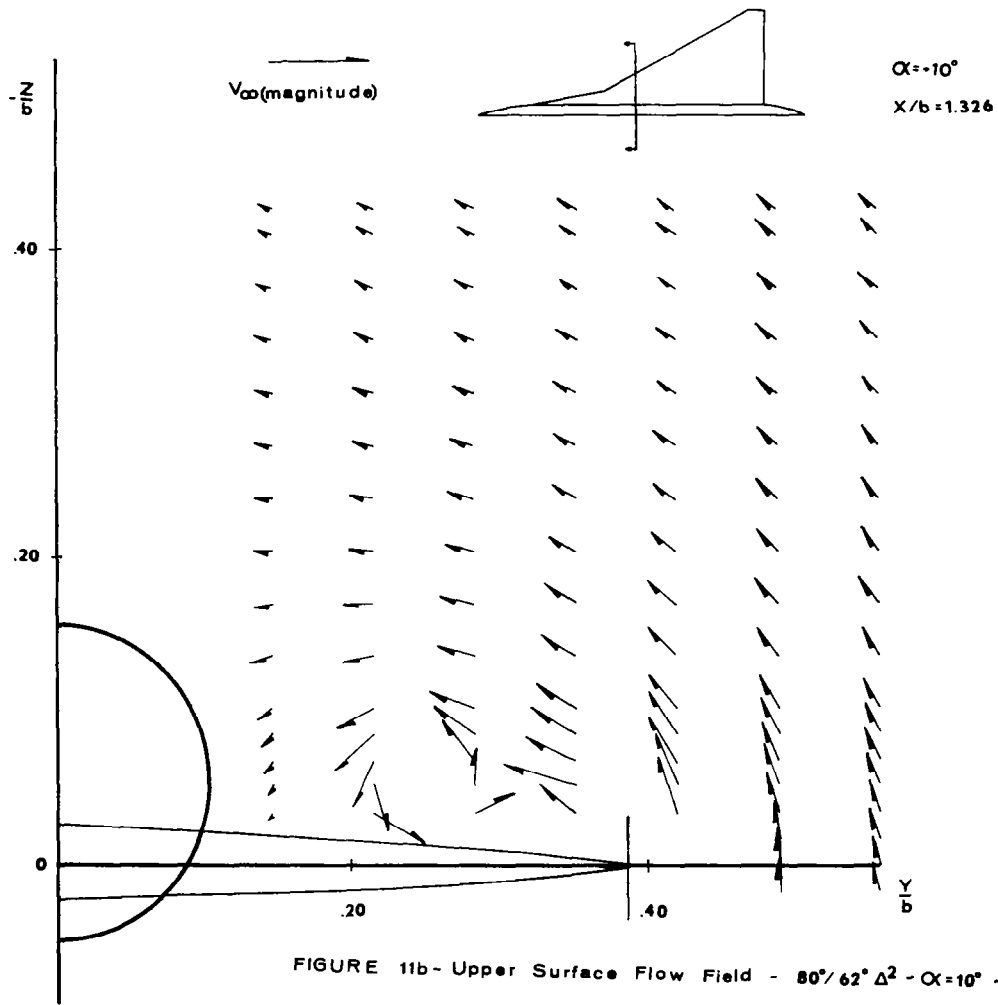


FIGURE 10f - Upper Surface Flow Field - $80\% \Delta^2$ - $\alpha = 5^\circ$ $X/b = -2.0$



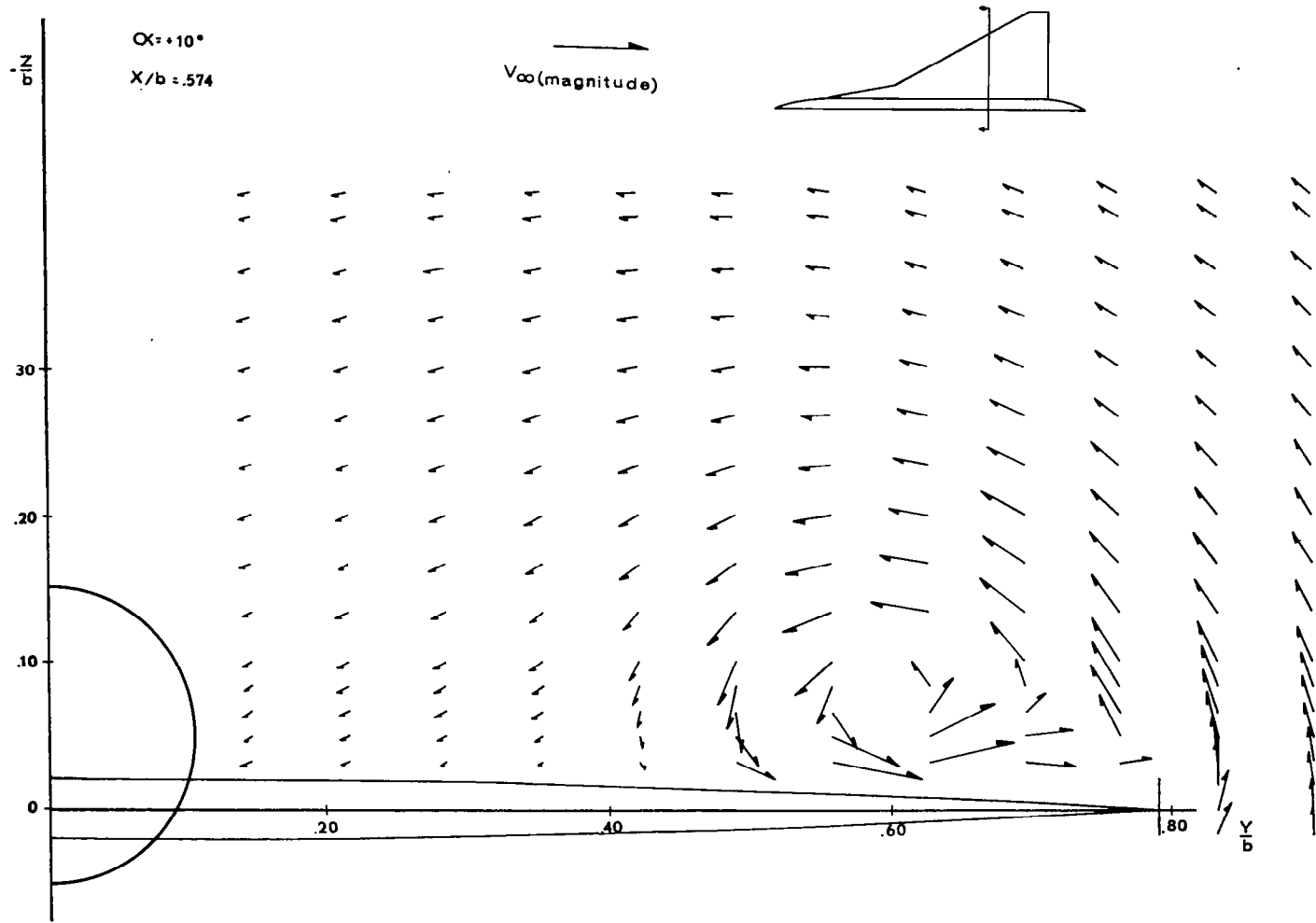


FIGURE 11c - Upper Surface Flow Field - $80^\circ 62' \Delta^2$ - $\alpha = 10^\circ$ $X/b = .574$

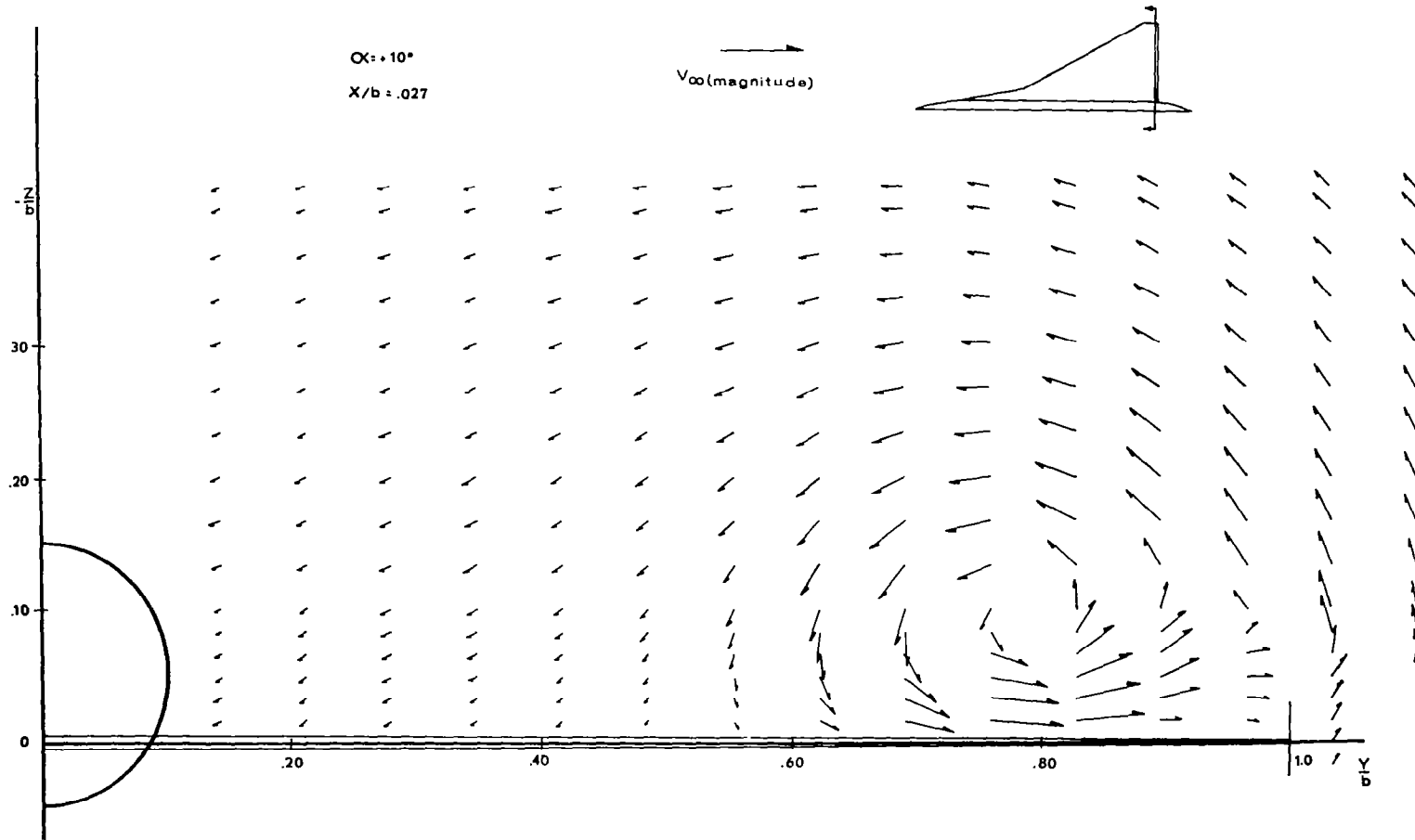
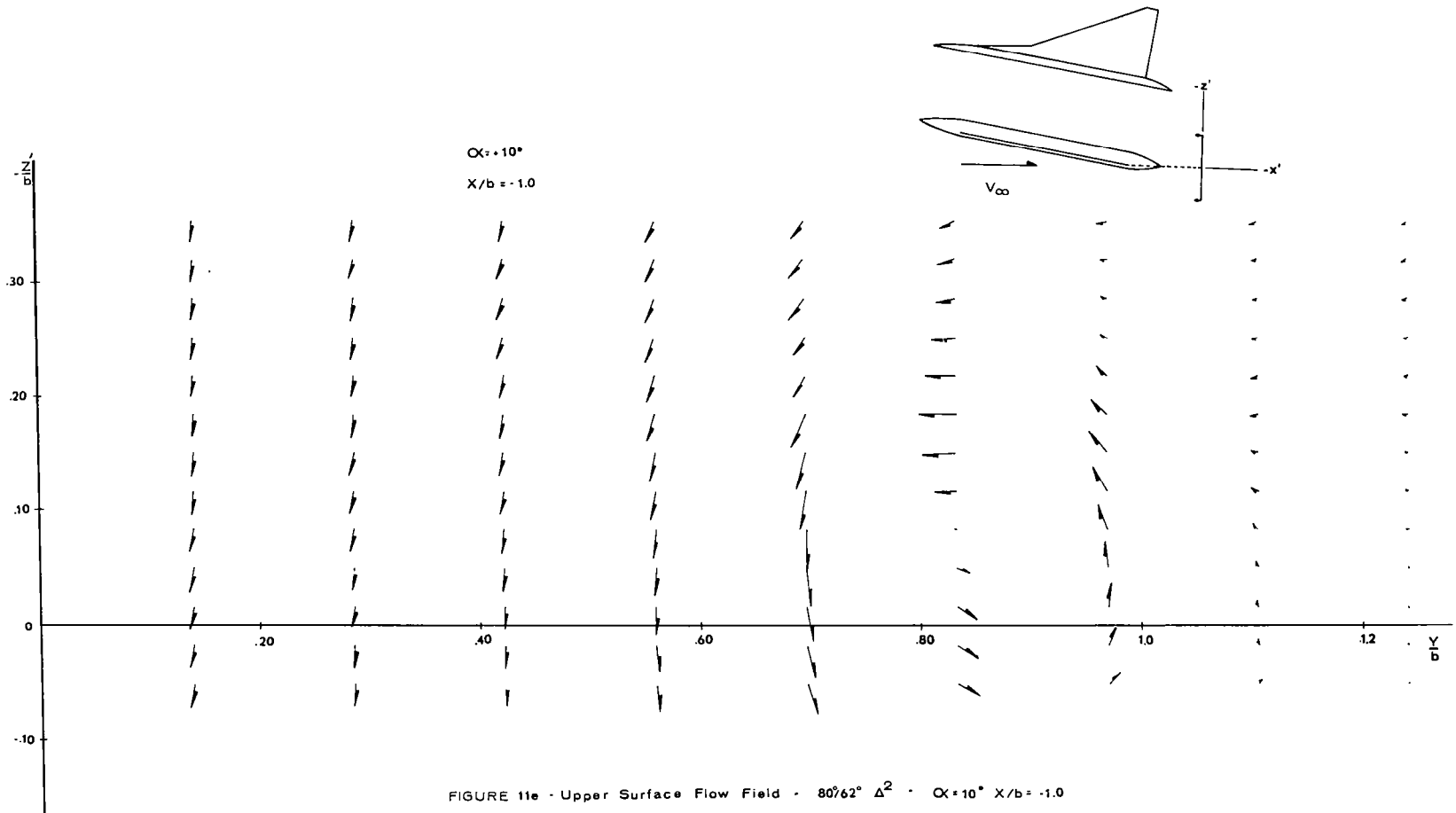
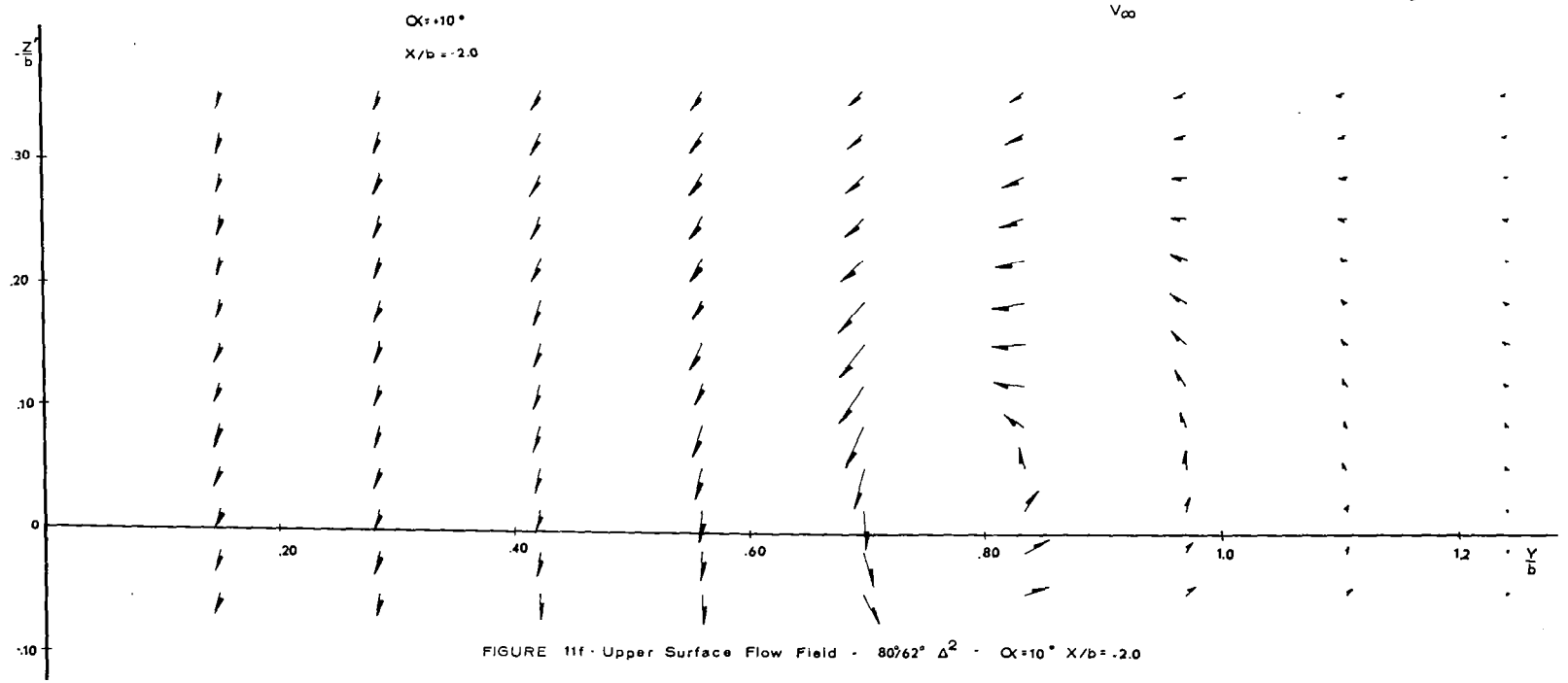
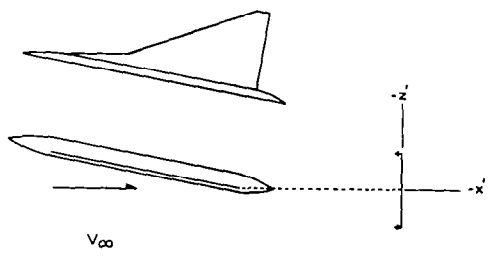


FIGURE 11d - Upper Surface Flow Field - $80\% \Delta^2$ - $\alpha = 10^\circ$ $X/b = .027$





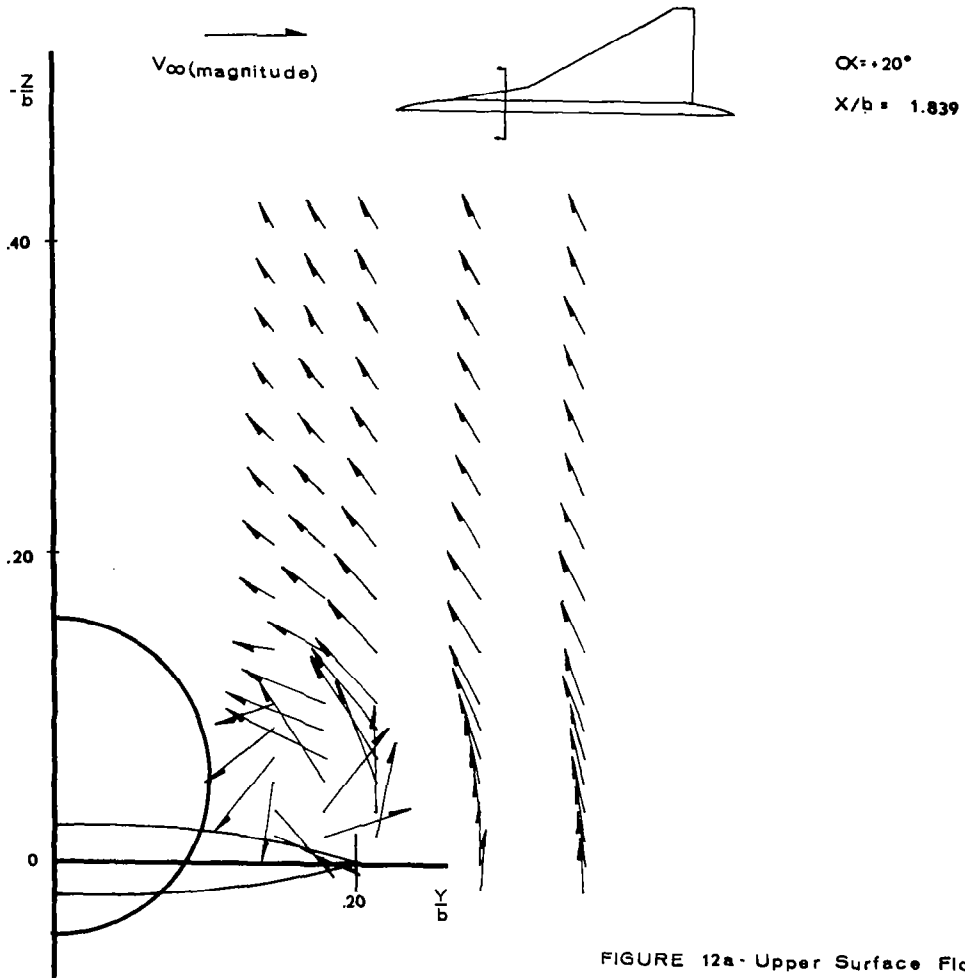
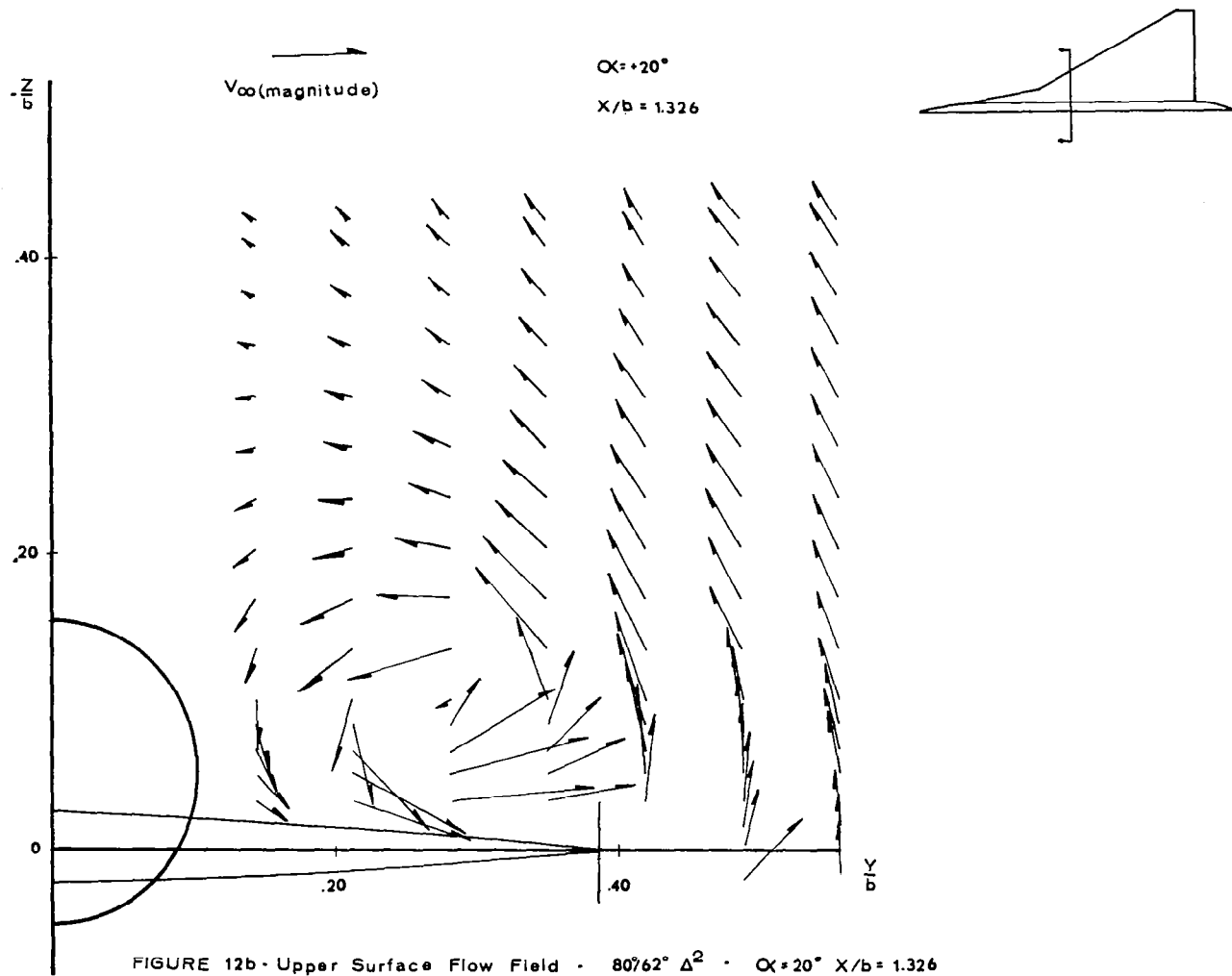


FIGURE 12a - Upper Surface Flow Field - $80762^\circ \Delta^2$ - $\alpha = 20^\circ$ $X/b = 1.839$



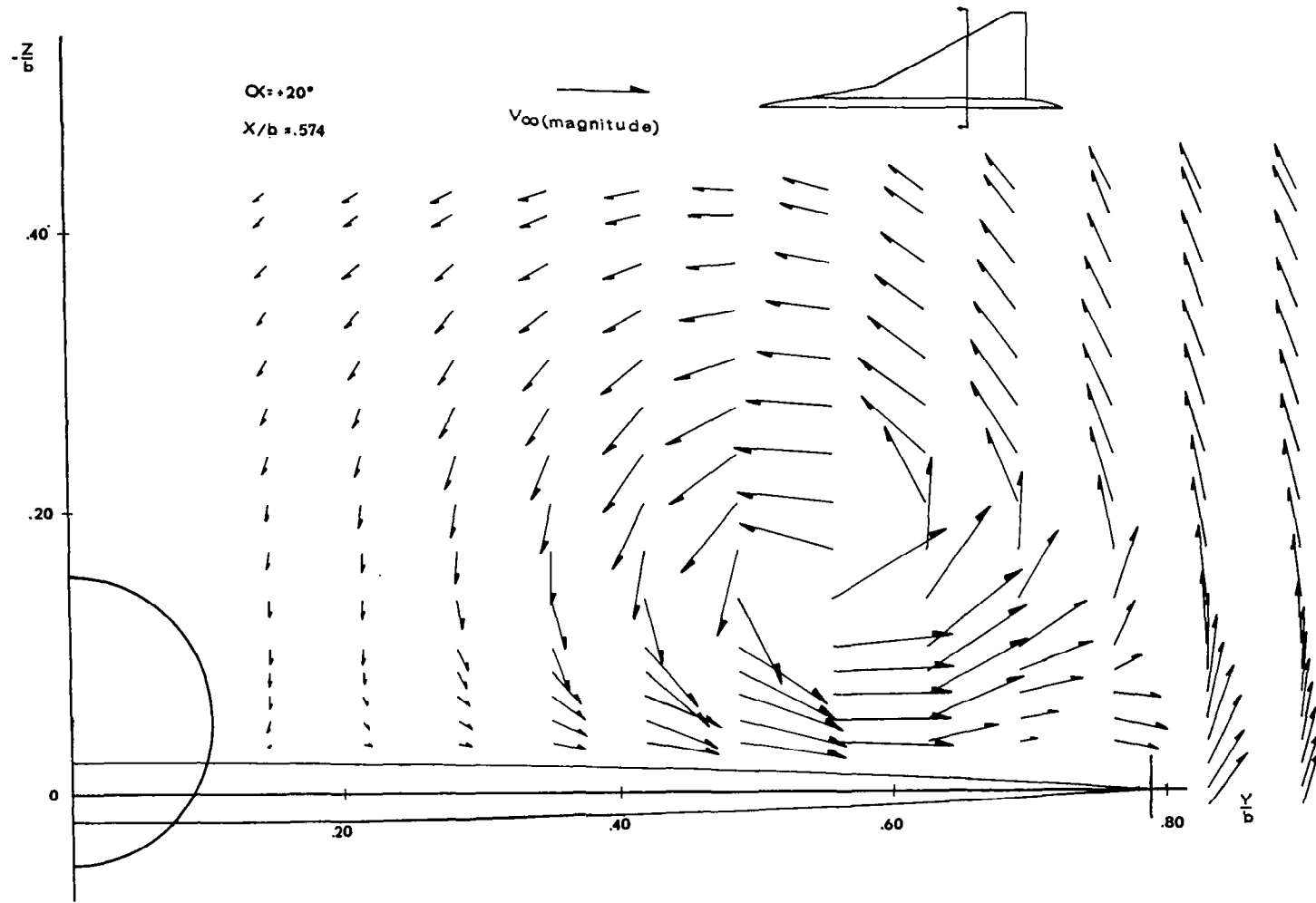


FIGURE 12c - Upper Surface Flow Field - $80^\circ/62^\circ \Delta^2$ - $\alpha = 20^\circ$ $X/b = .574$

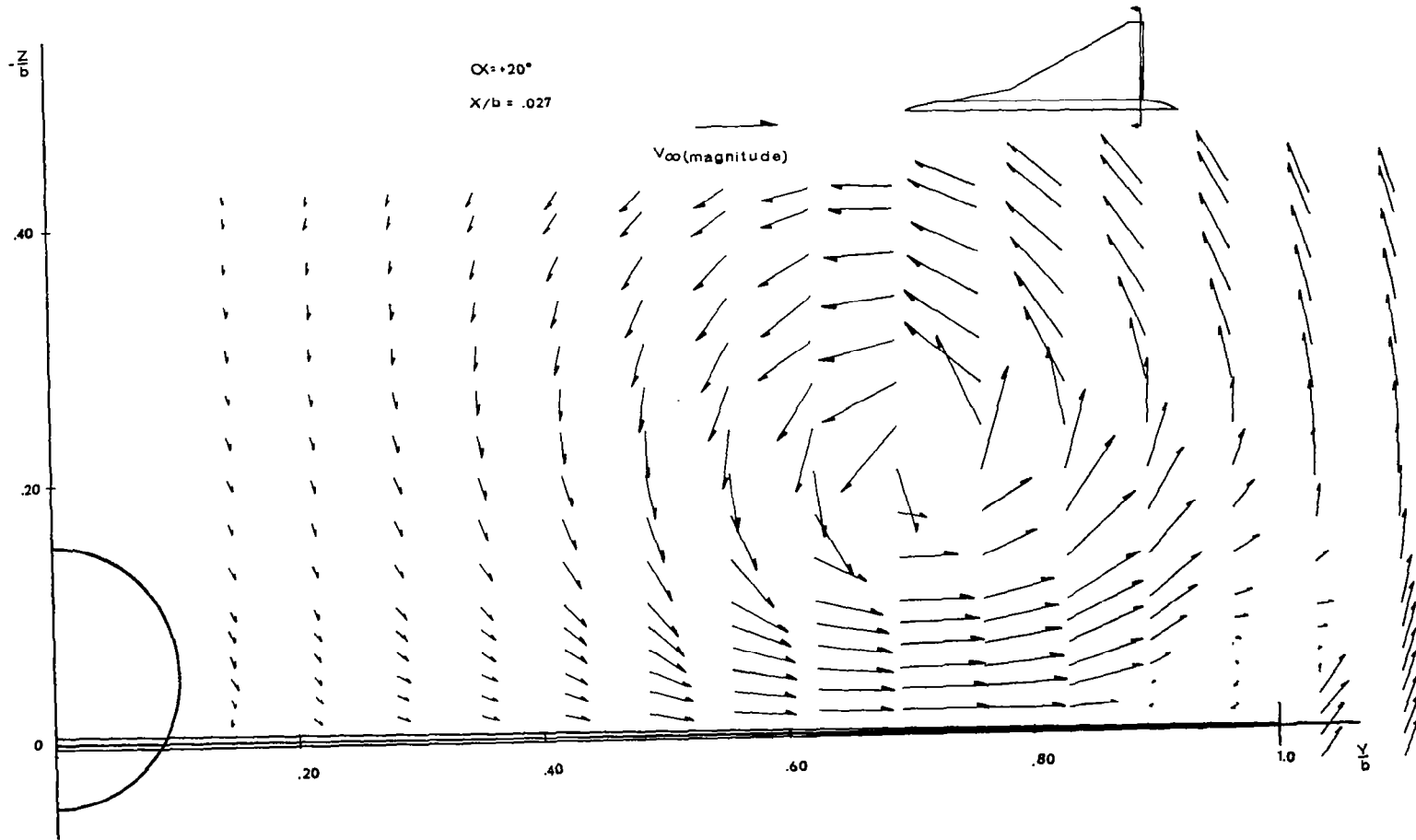


FIGURE 12d- Upper Surface Flow Field - $80^\circ/62^\circ \Delta^2$ - $\alpha = 20^\circ$ $X/b = .027$

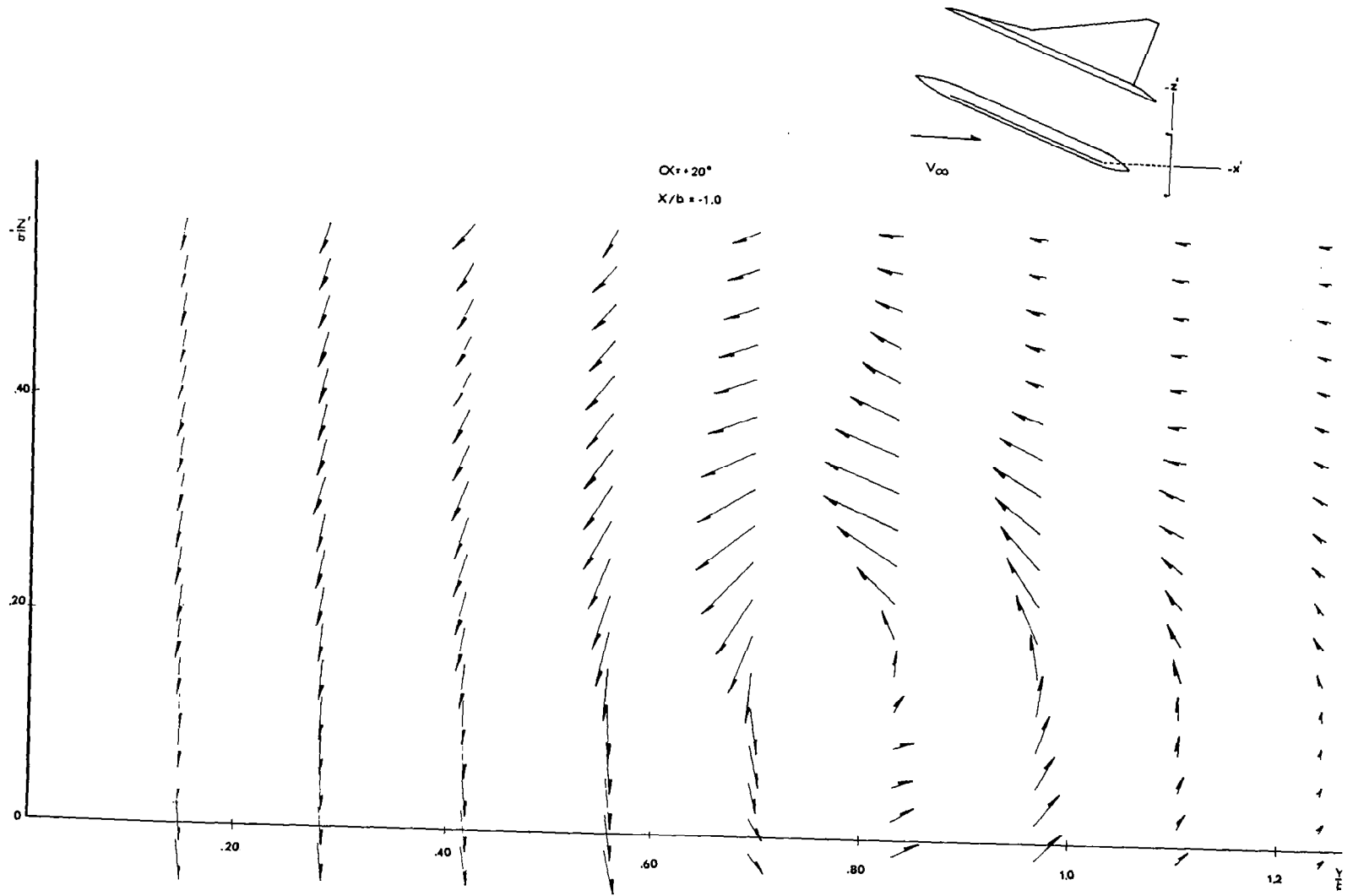


FIGURE 12e - Upper Surface Flow Field - $80/62^\circ \Delta^2$ - $\alpha = 20^\circ$ $X/b = -1.0$

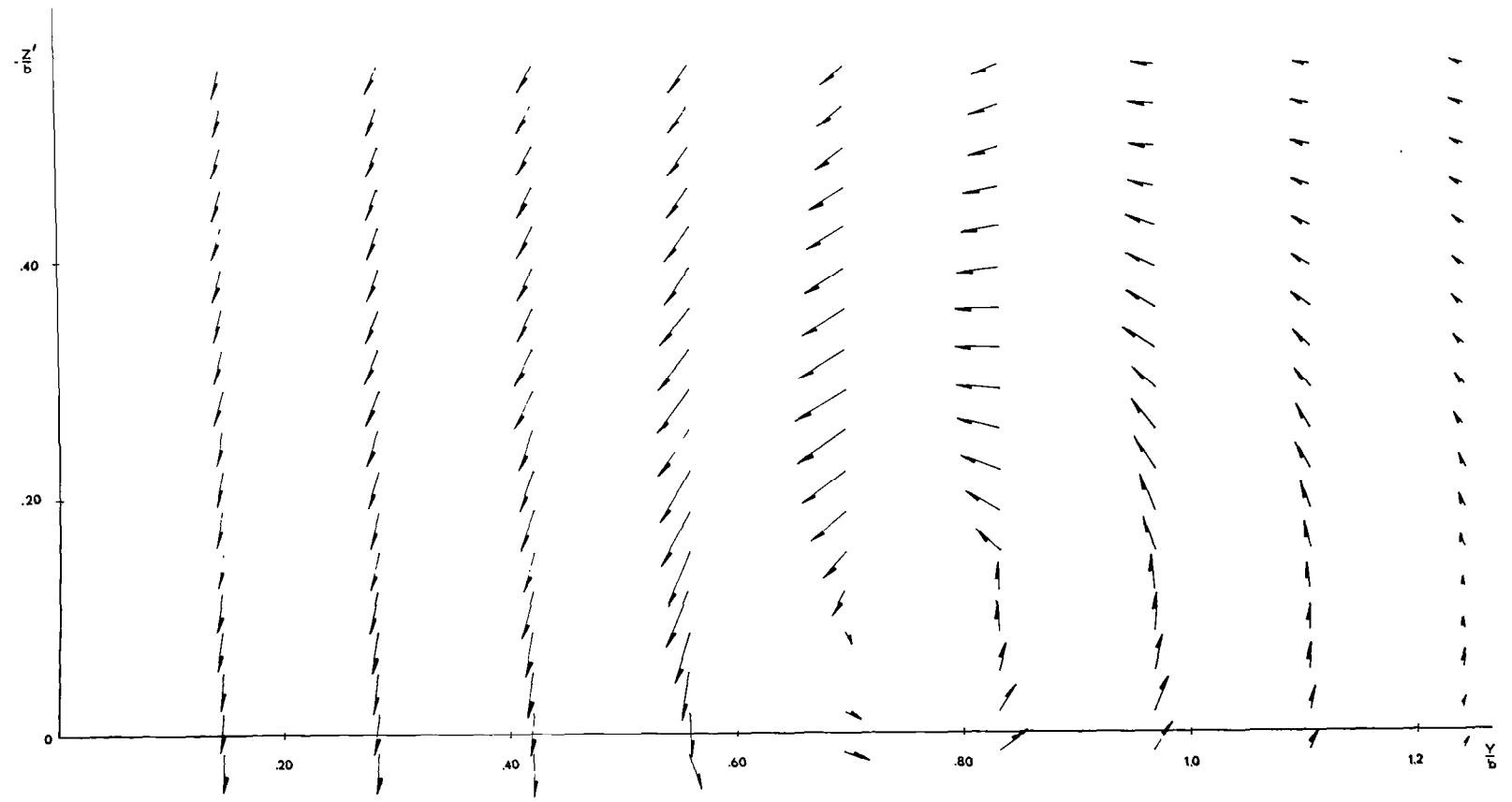
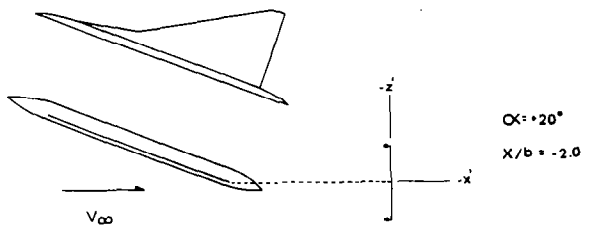


FIGURE 12f - Upper Surface Flow Field - $80762^\circ \Delta^2$ - $\alpha = 20^\circ$ $X/b = -2.0$

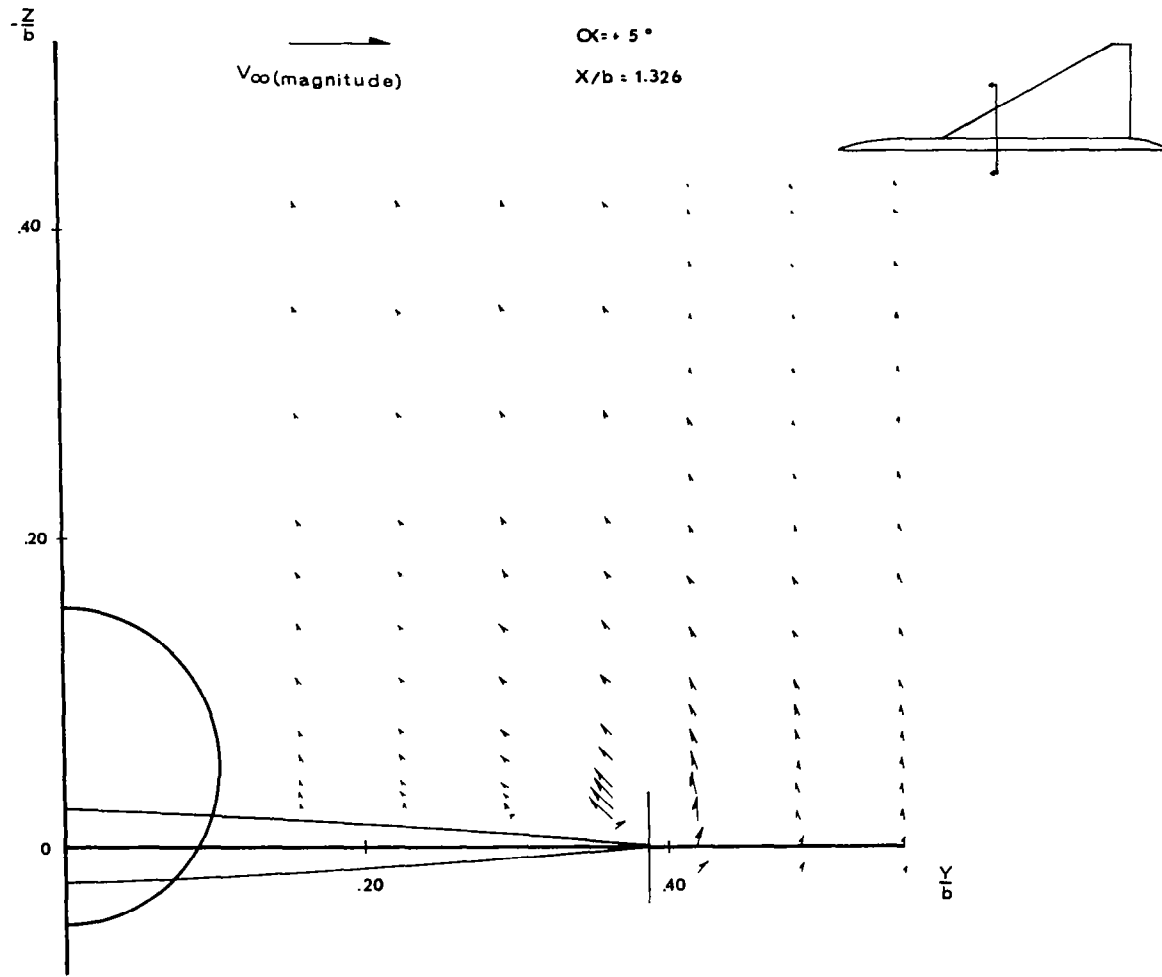


FIGURE 13a - Upper Surface Flow Field - $62^\circ \Delta$ - $\alpha = 5^\circ$ $X/b = 1.326$

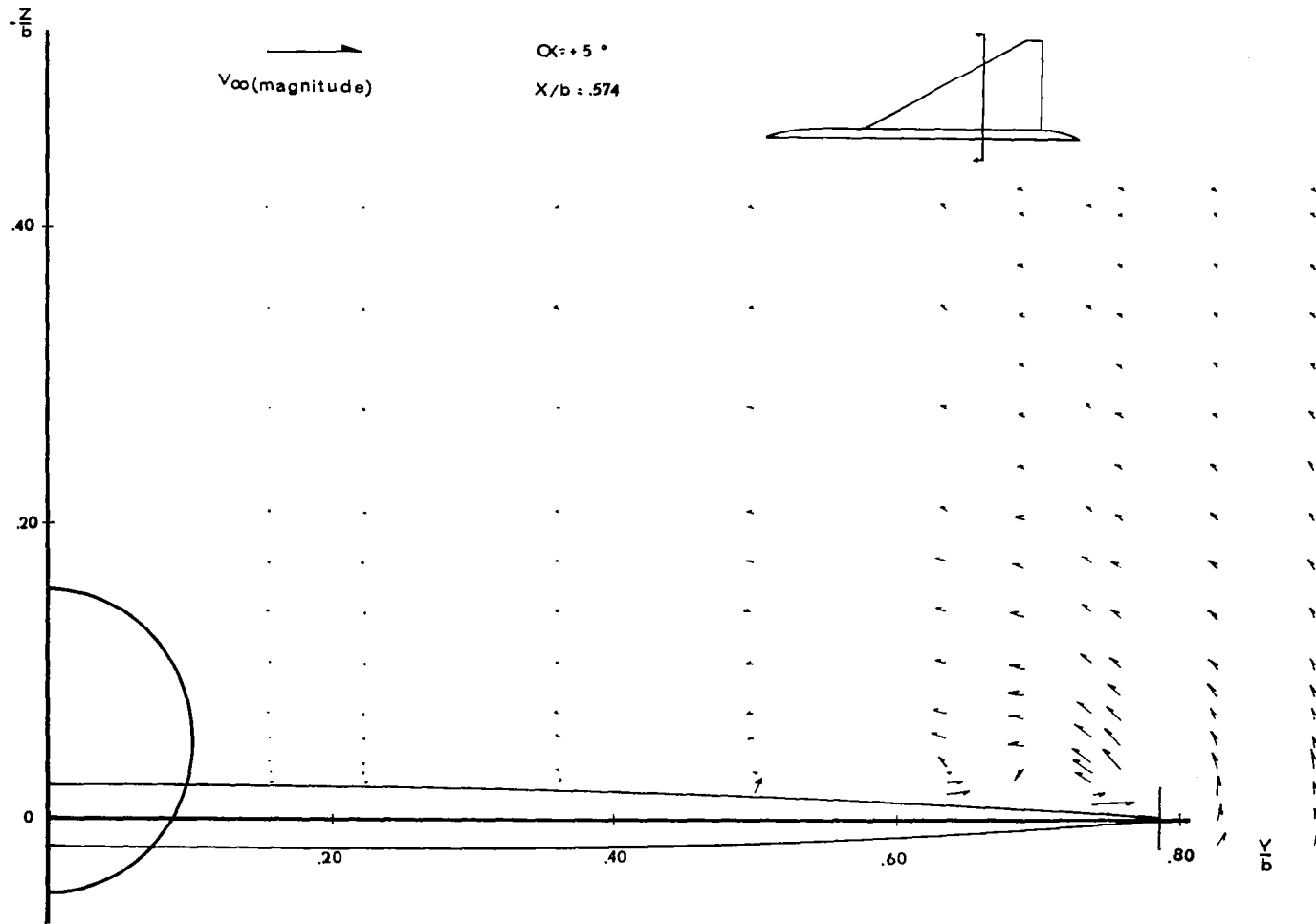


FIGURE 13b - Upper Surface Flow Field - $62^\circ \Delta$ - $\alpha = 5^\circ$ $X/b = .574$

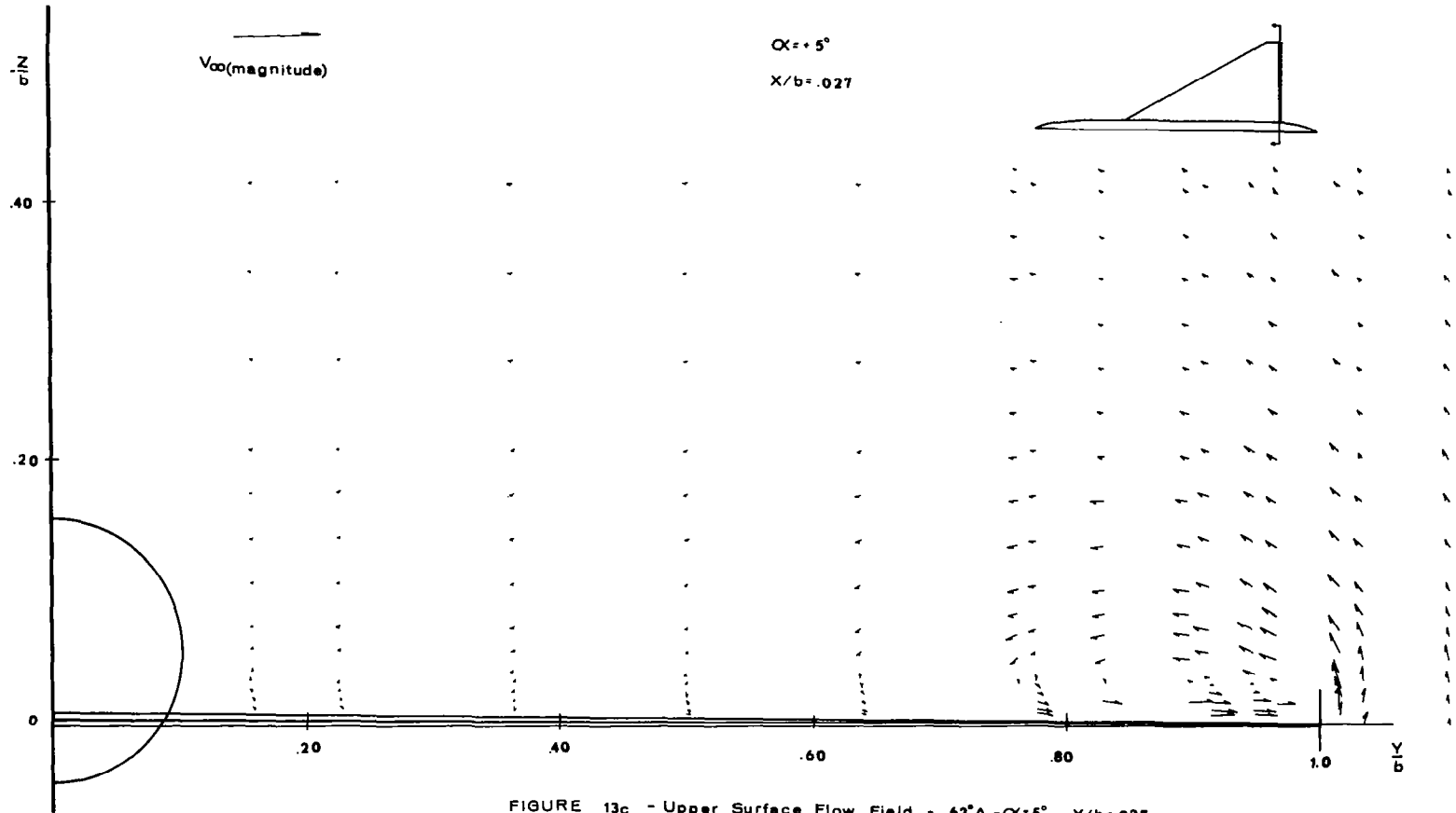


FIGURE 13c - Upper Surface Flow Field - $62^\circ\Delta$ - $\alpha = 5^\circ$ - $X/b = .027$

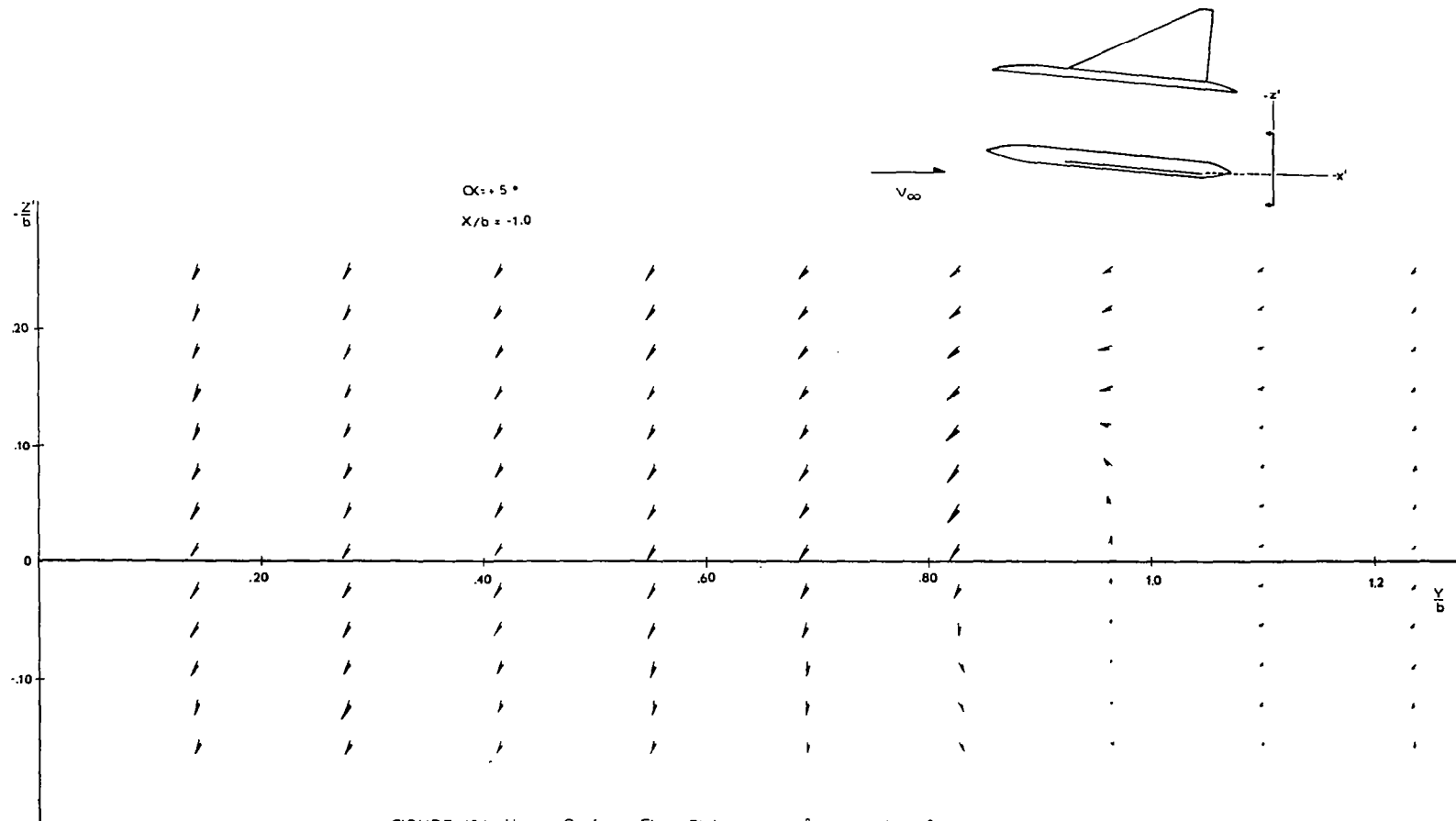


FIGURE 13d - Upper Surface Flow Field - $62^\circ \Delta$ - $\alpha = 5^\circ$ $X/b = -1.0$

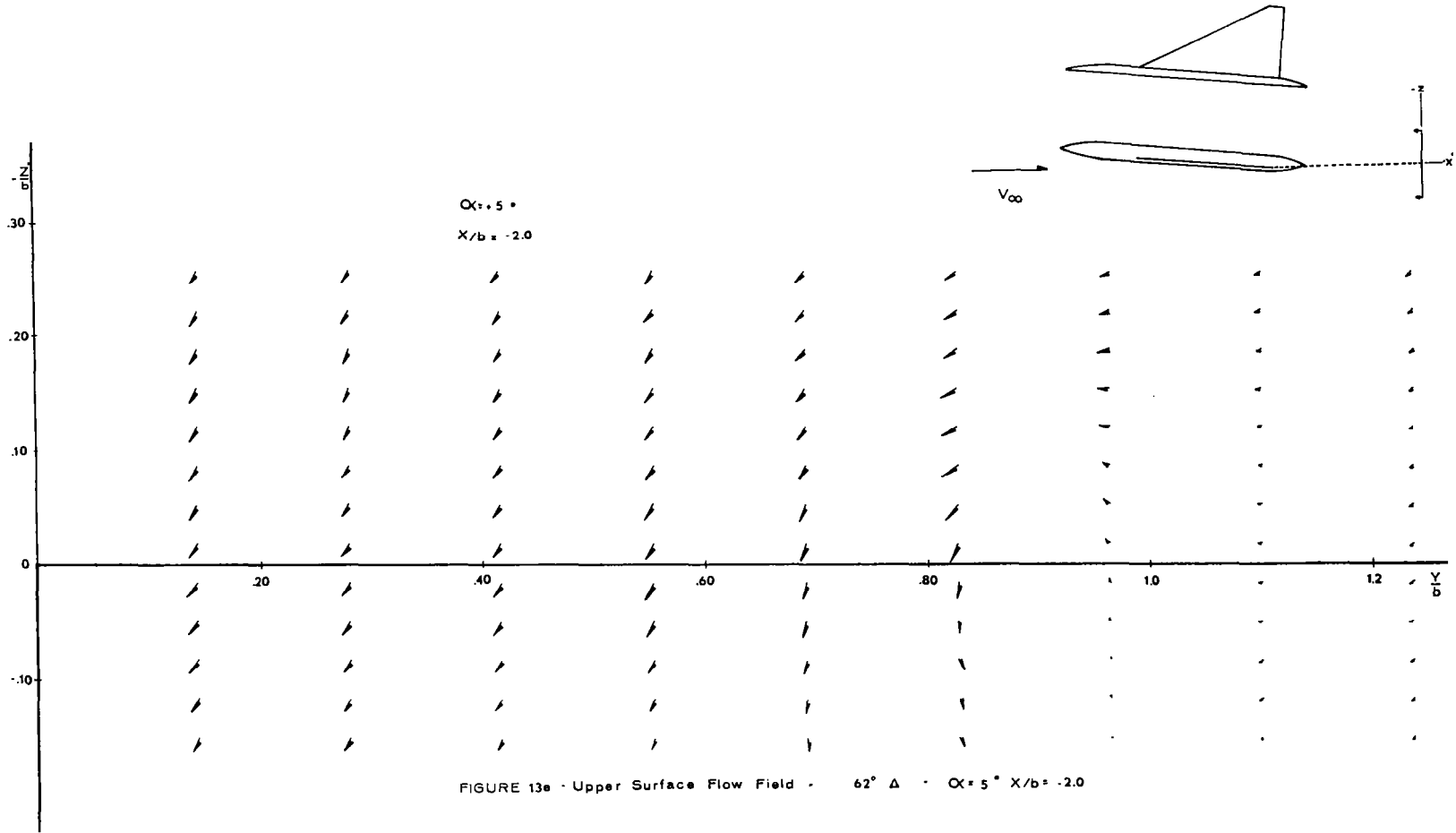


FIGURE 13e - Upper Surface Flow Field - $62^\circ \Delta$ - $\alpha = 5^\circ$ $X/b = -2.0$

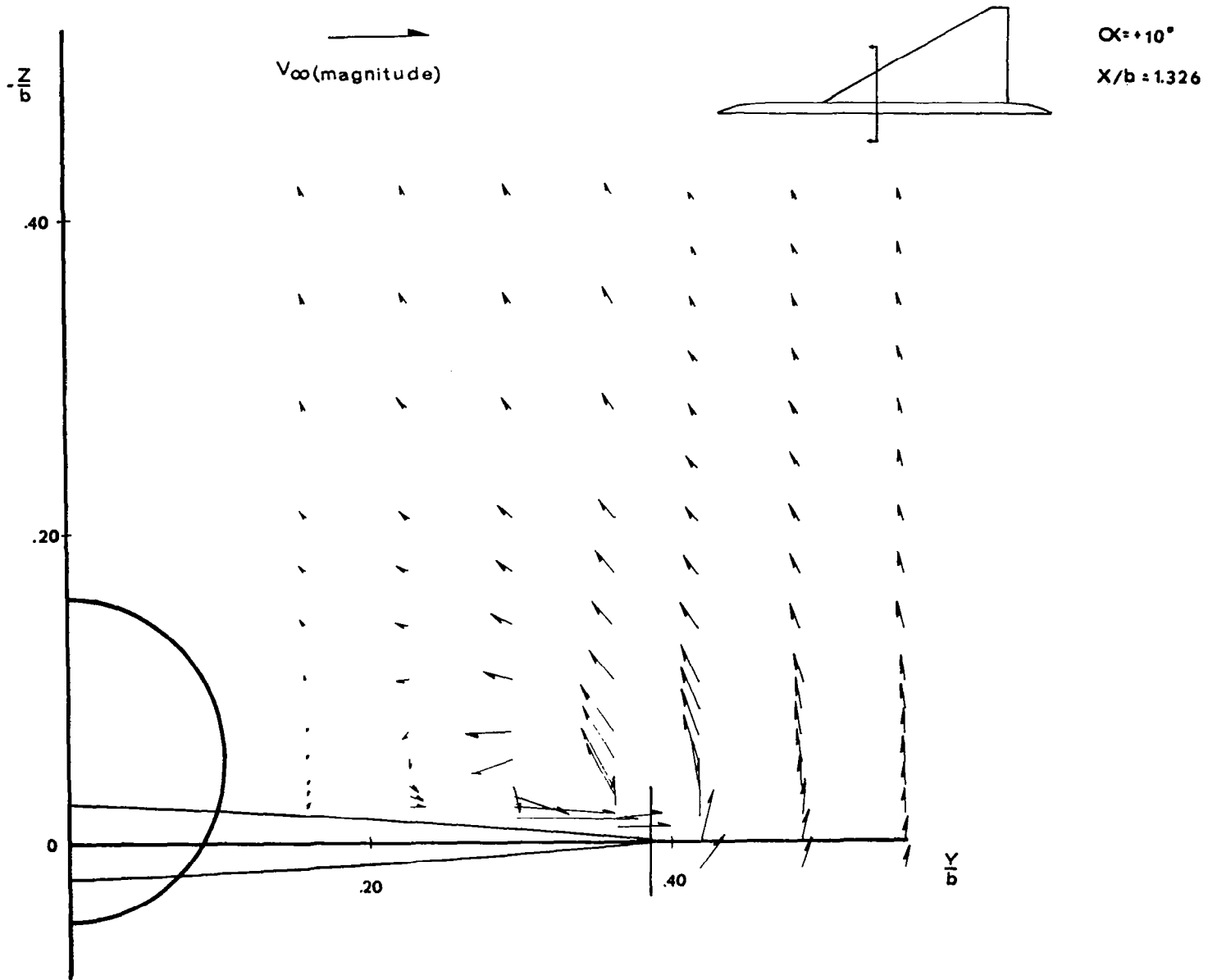


FIGURE 14a - Upper Surface Flow Field - $62^\circ \Delta$ - $\alpha = 10^\circ$ $X/b = 1.326$

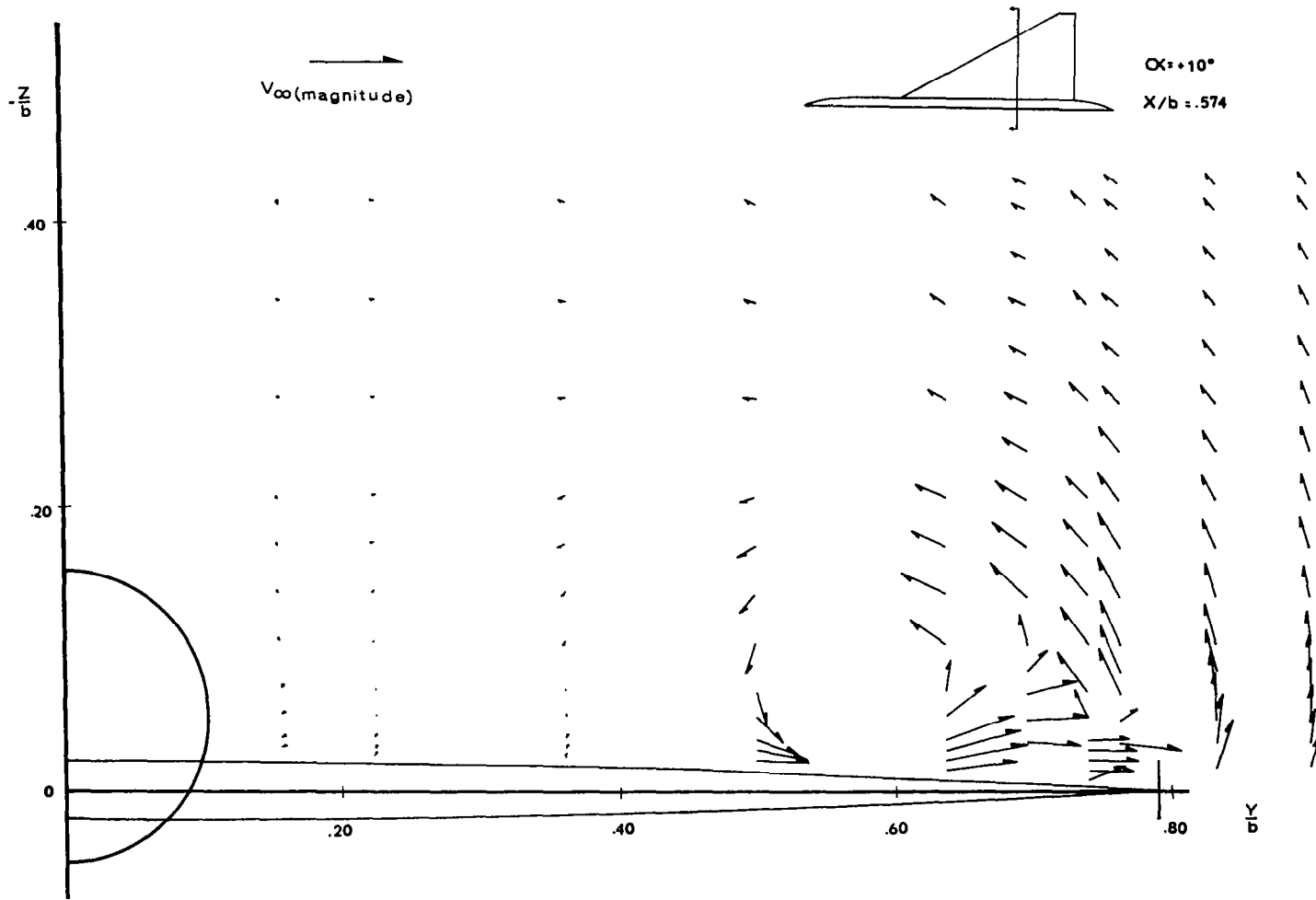


FIGURE 14b - Upper Surface Flow Field - $62^\circ \Delta$ - $\alpha = 10^\circ$ $X/b = .574$

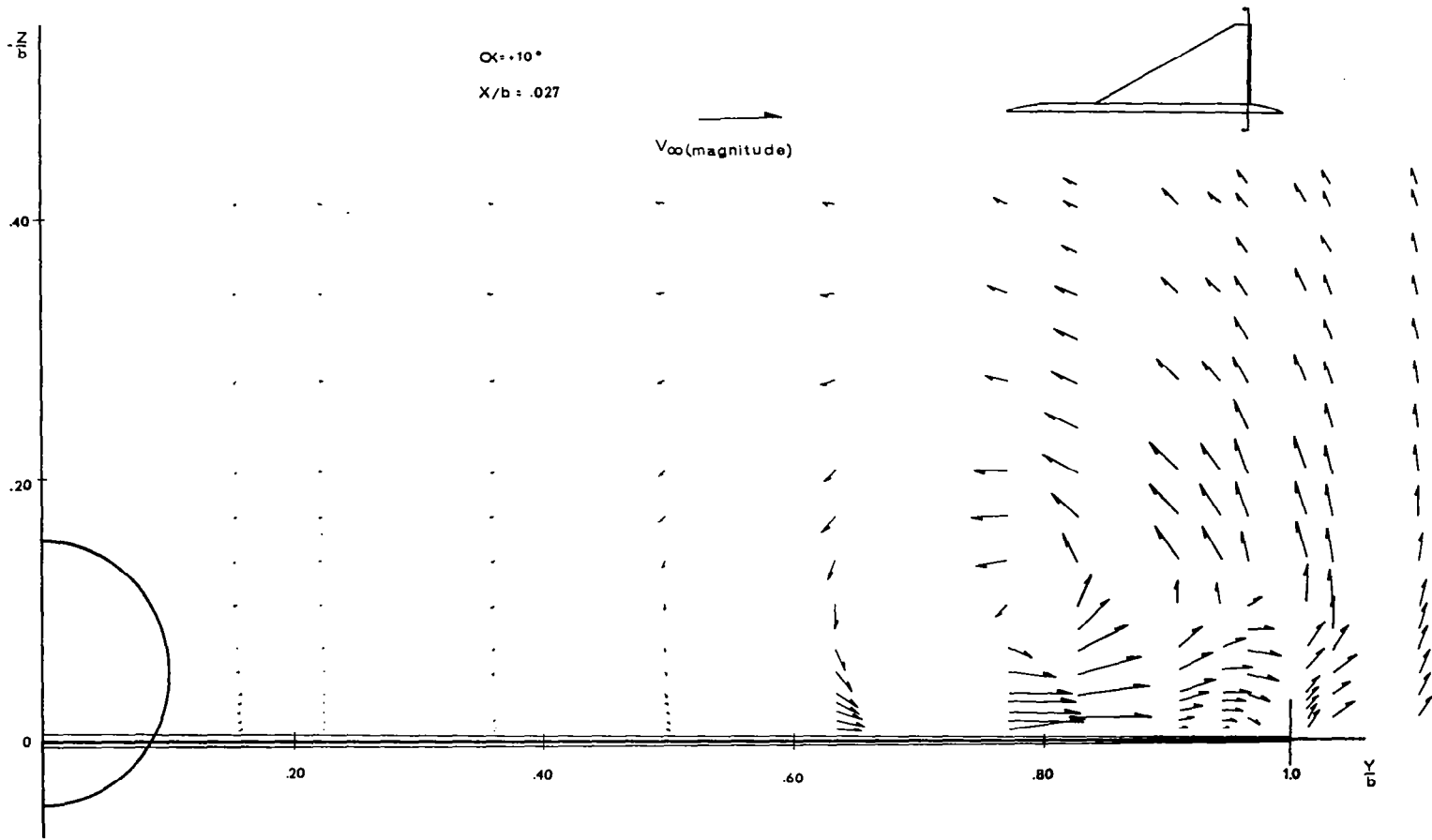
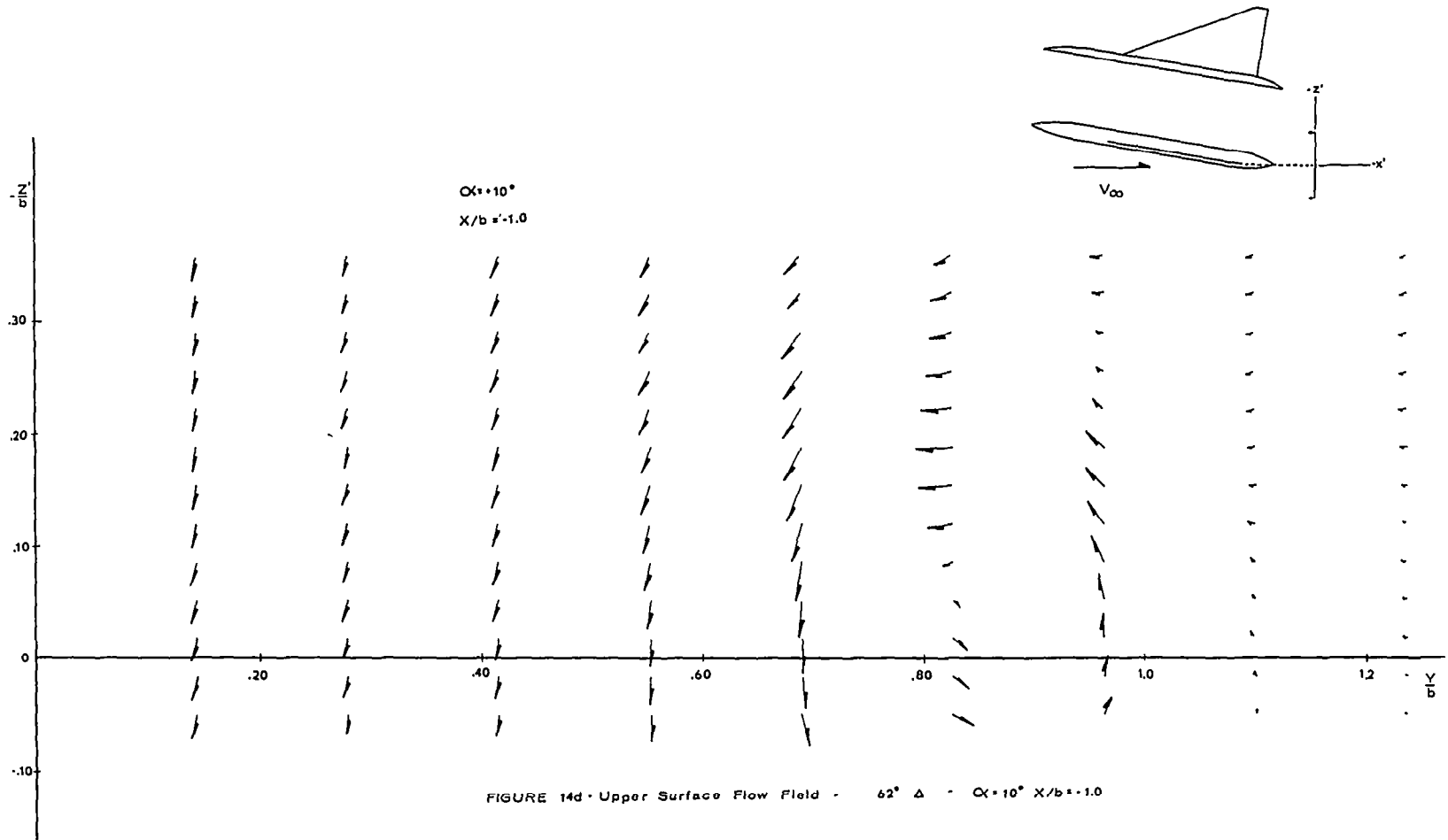
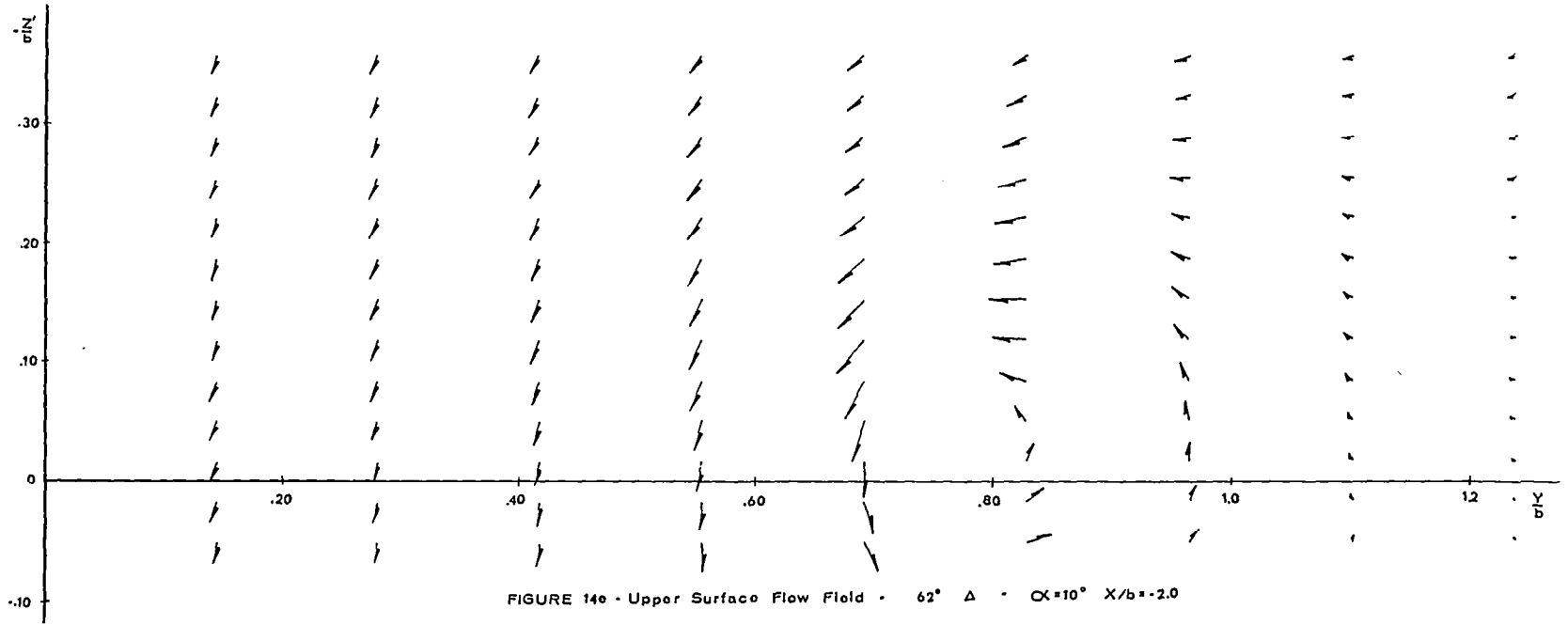
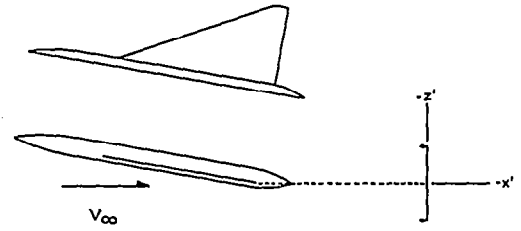


FIGURE 14c - Upper Surface Flow Field - $62^\circ \Delta$ - $\alpha = 10^\circ$ $X/b = .027$



$\alpha = 10^\circ$
 $X/b = 2.0$



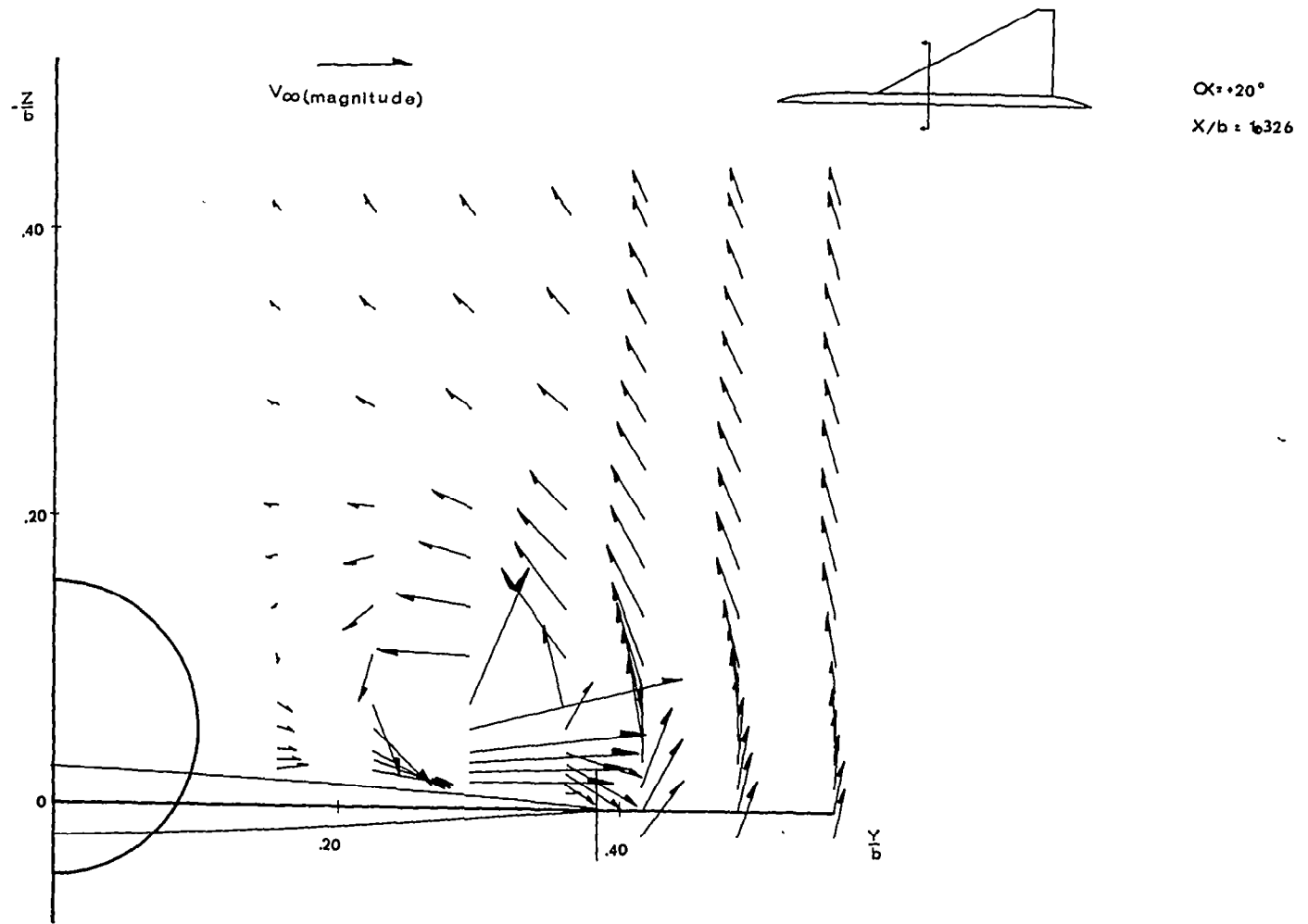


FIGURE 15a - Upper Surface Flow Field - $62^\circ \Delta$ - $\alpha = 20^\circ$ $X/b = 1.326$

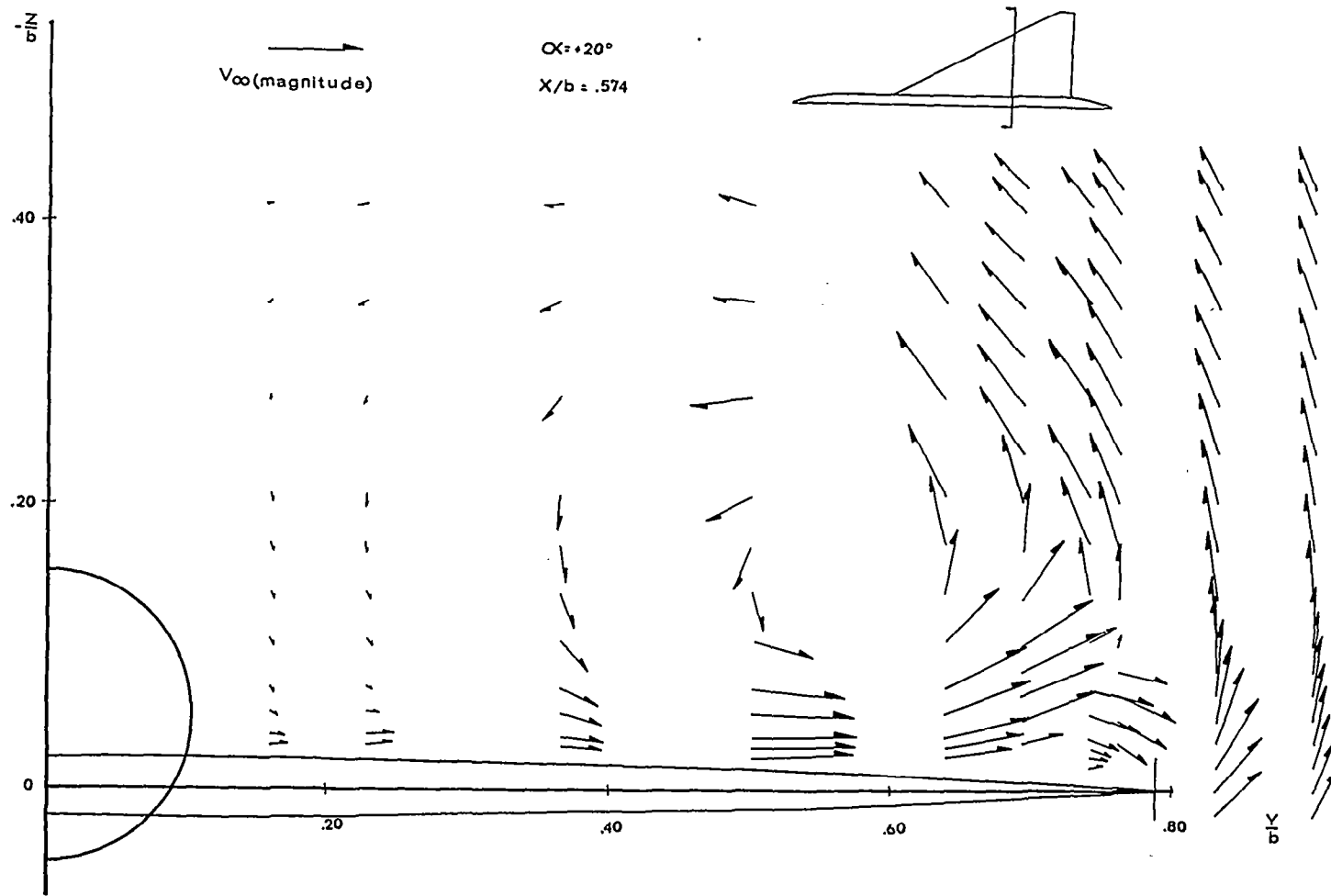
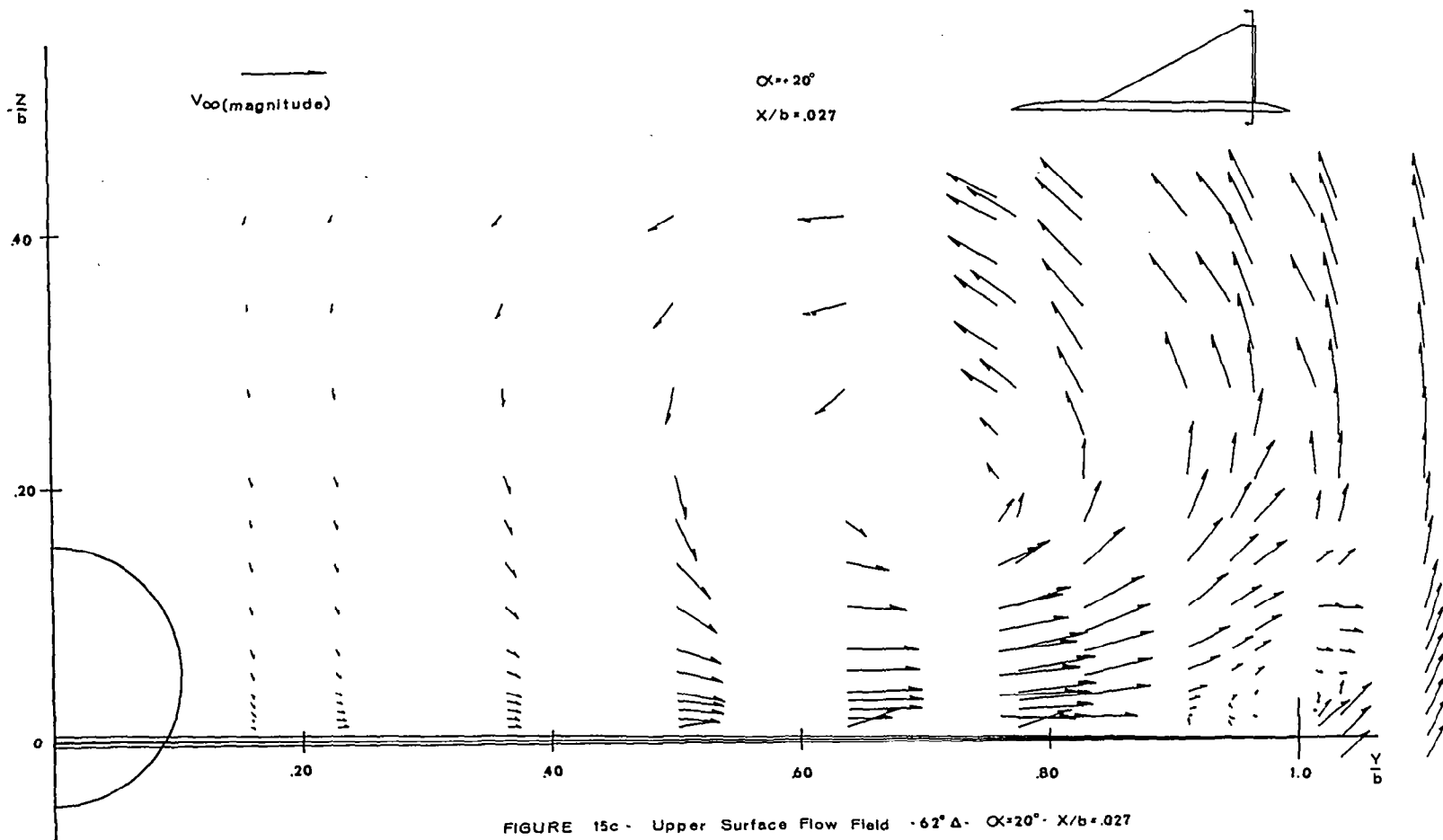


FIGURE 15b - Upper Surface Flow Field - $62^\circ \Delta$ - $\alpha = 20^\circ$ $X/b = .574$



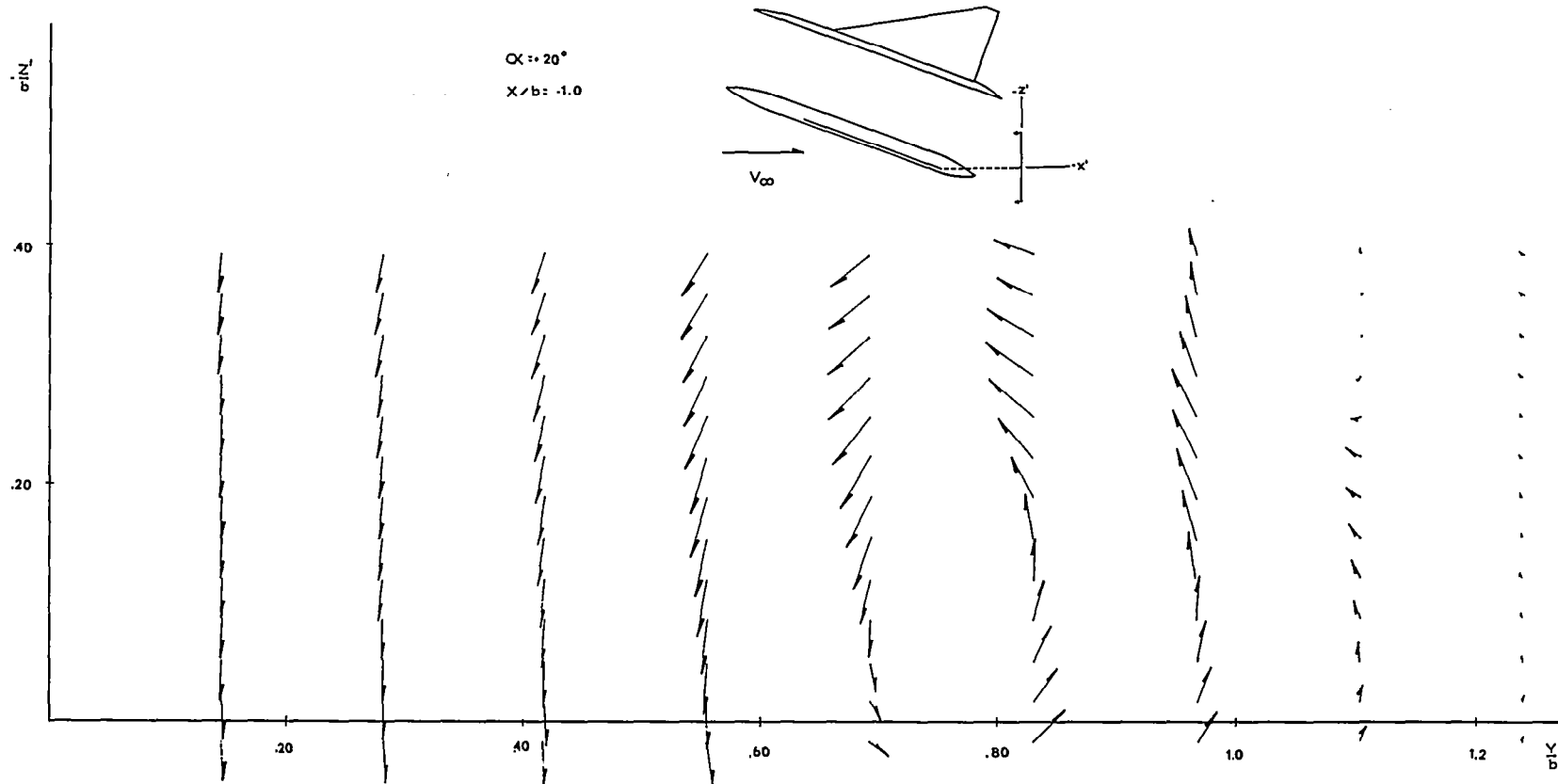
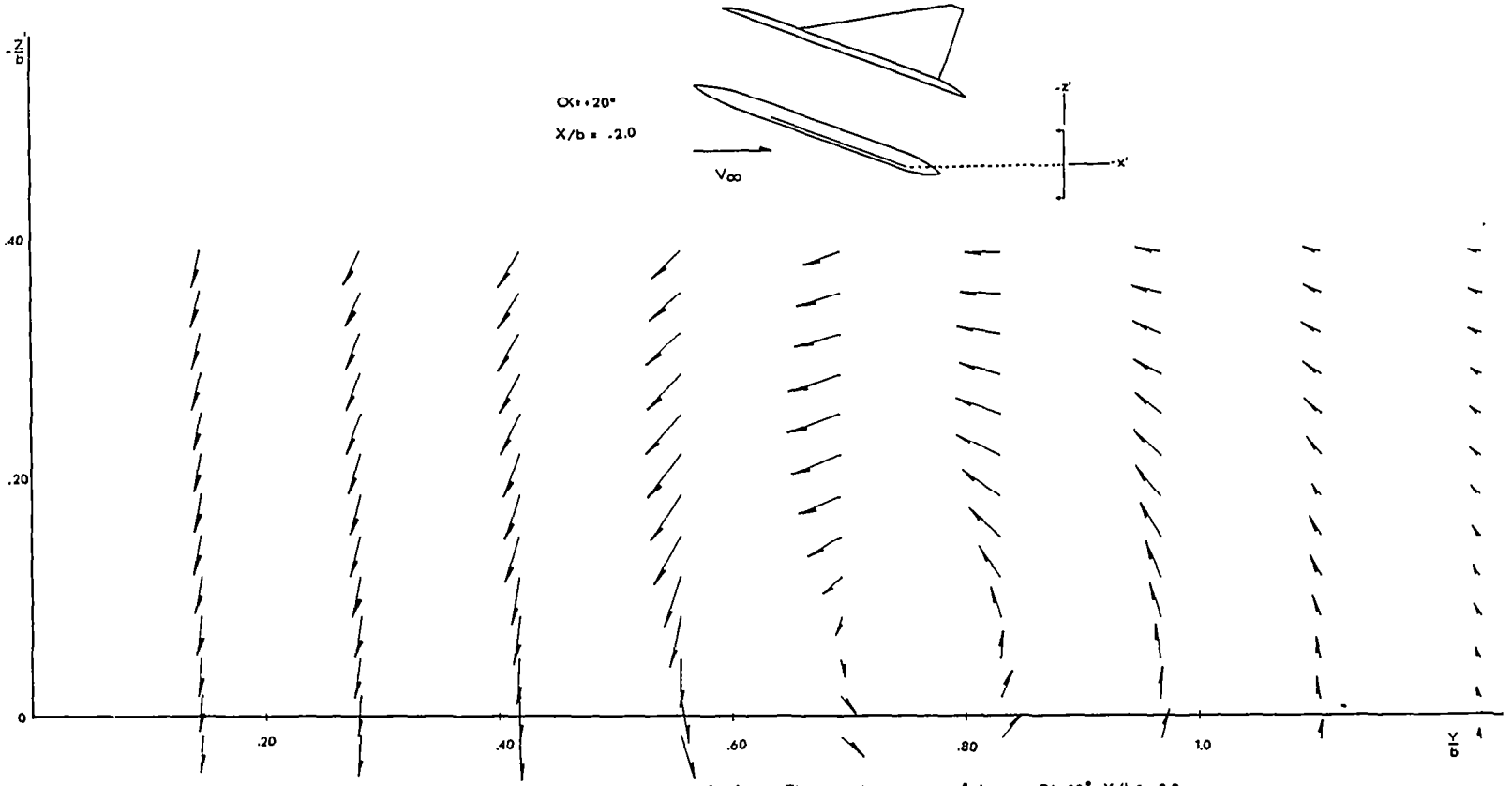
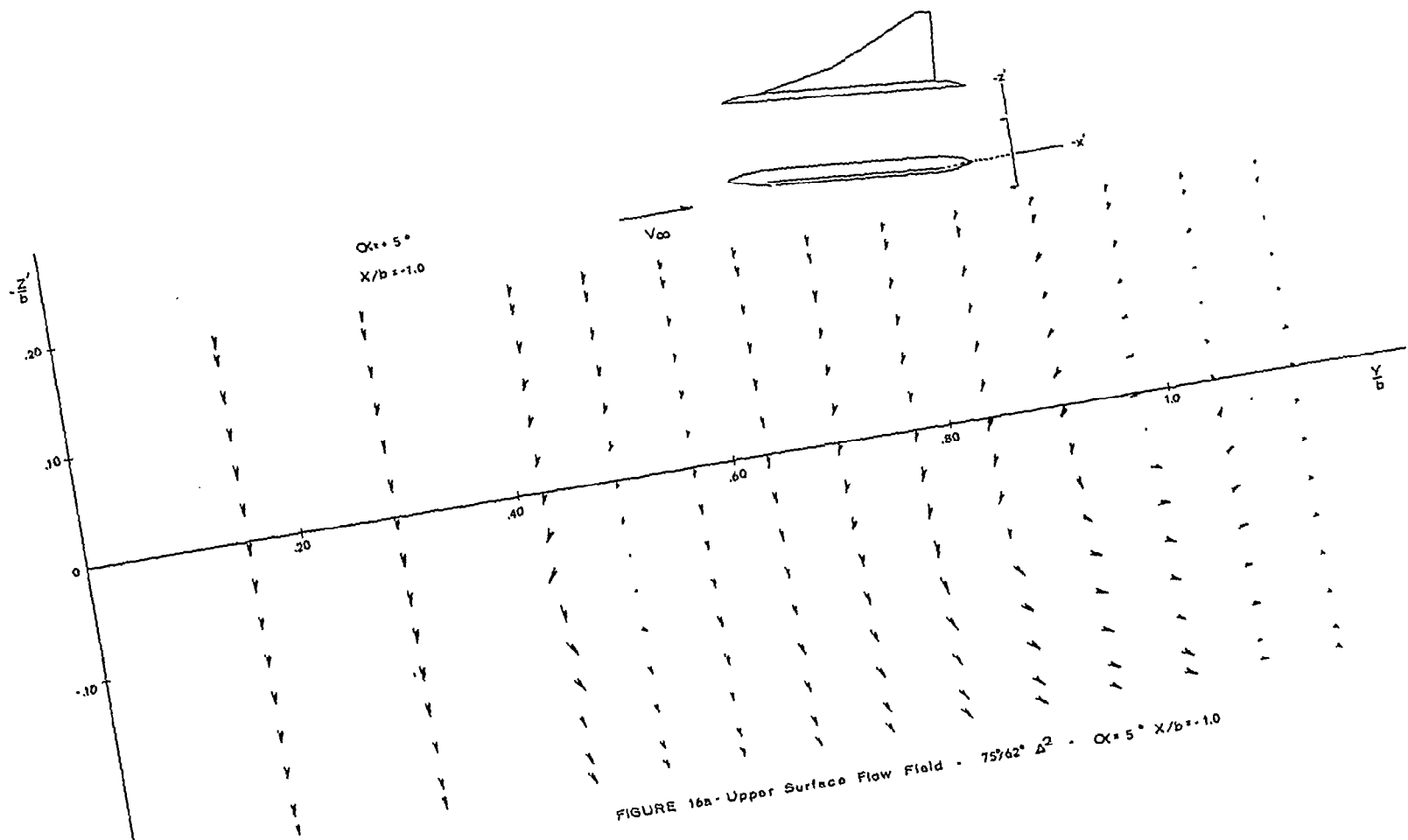
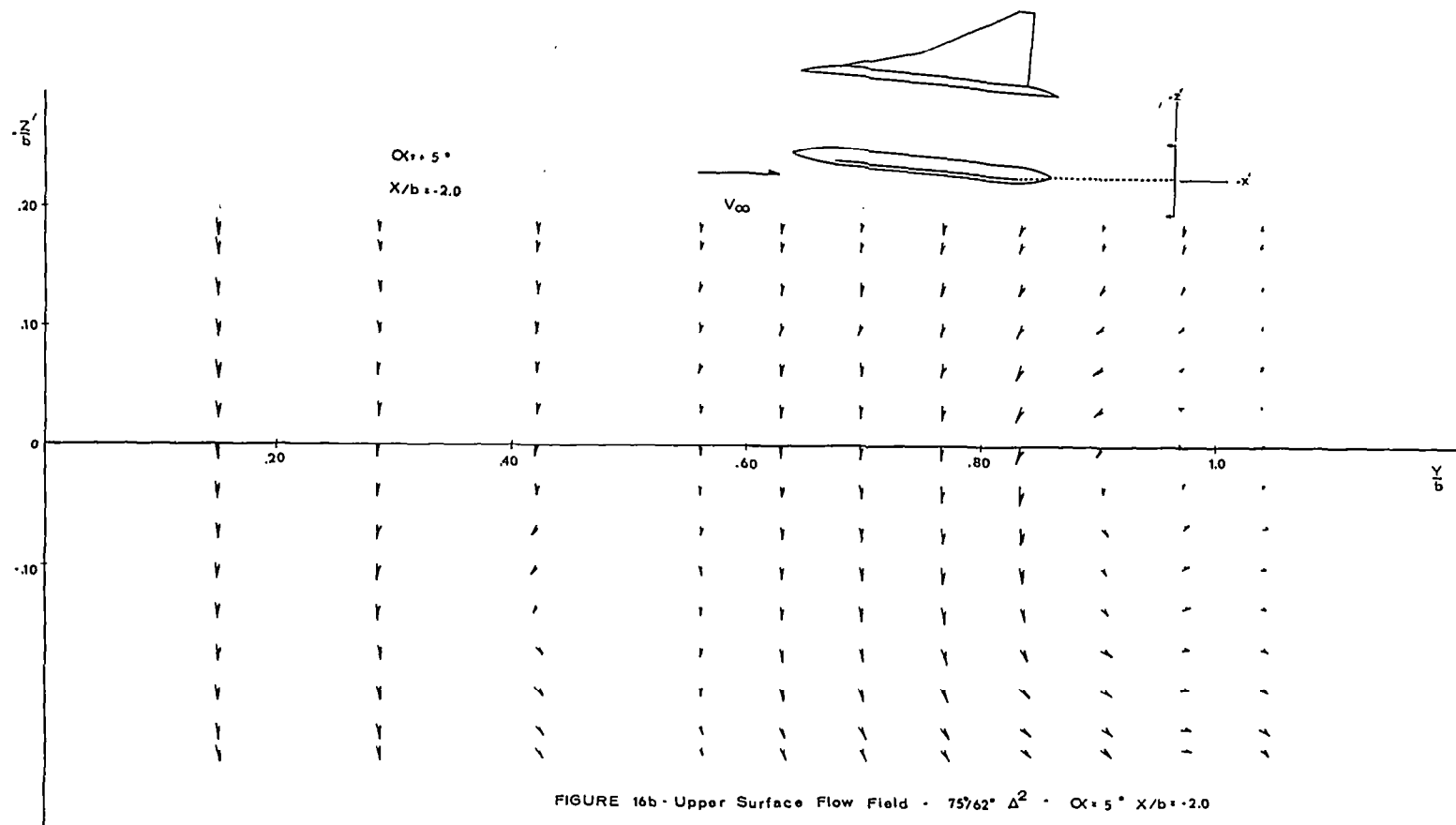


FIGURE 15d - Upper Surface Flow Field - $62^\circ \Delta$ - $\alpha = 20^\circ$ $X/b = -1.0$







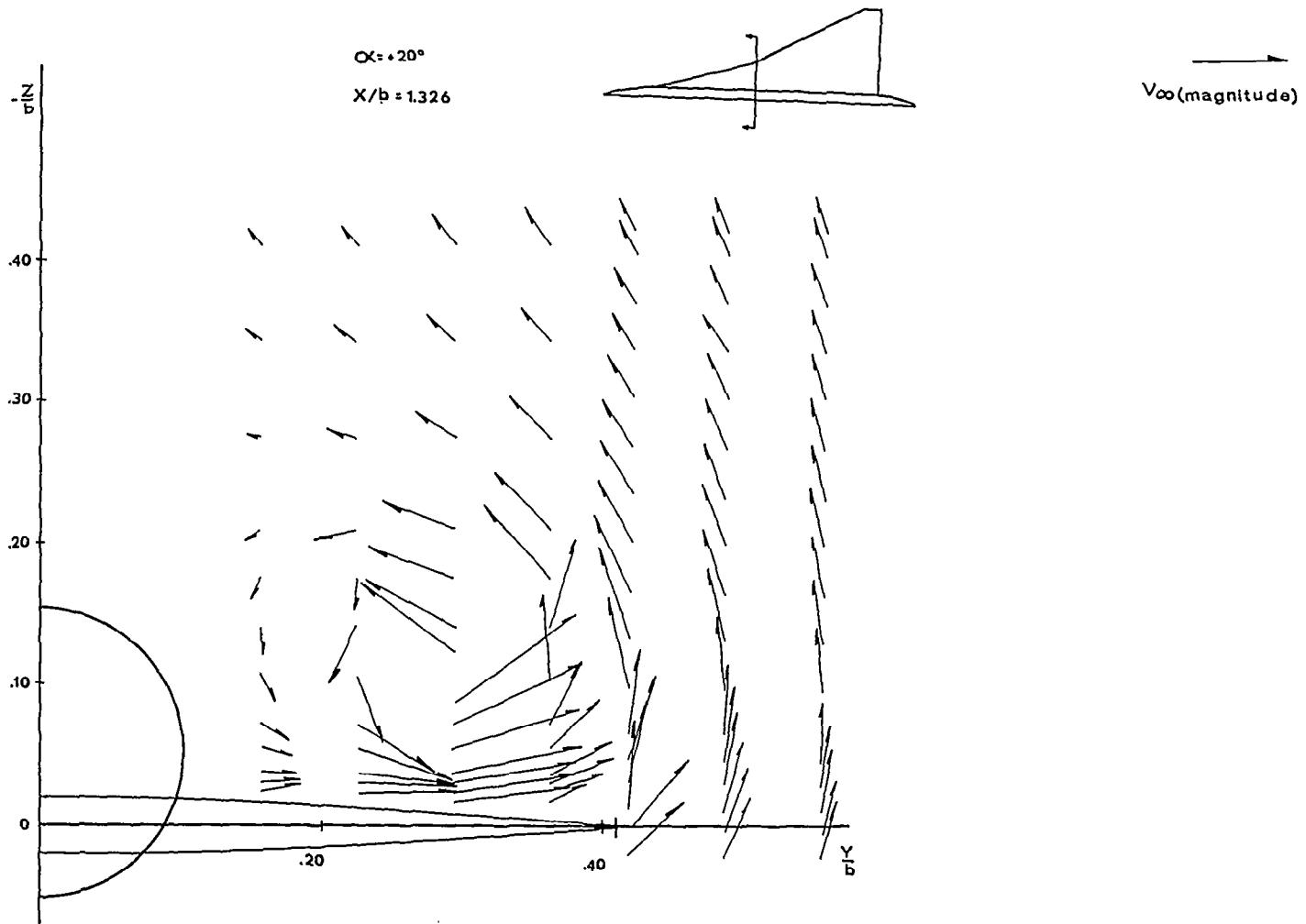


FIGURE 17a- Upper Surface Flow Field - $75^\circ 62' \Delta^2$ - $\alpha = 20^\circ$ $X/b = 1.326$

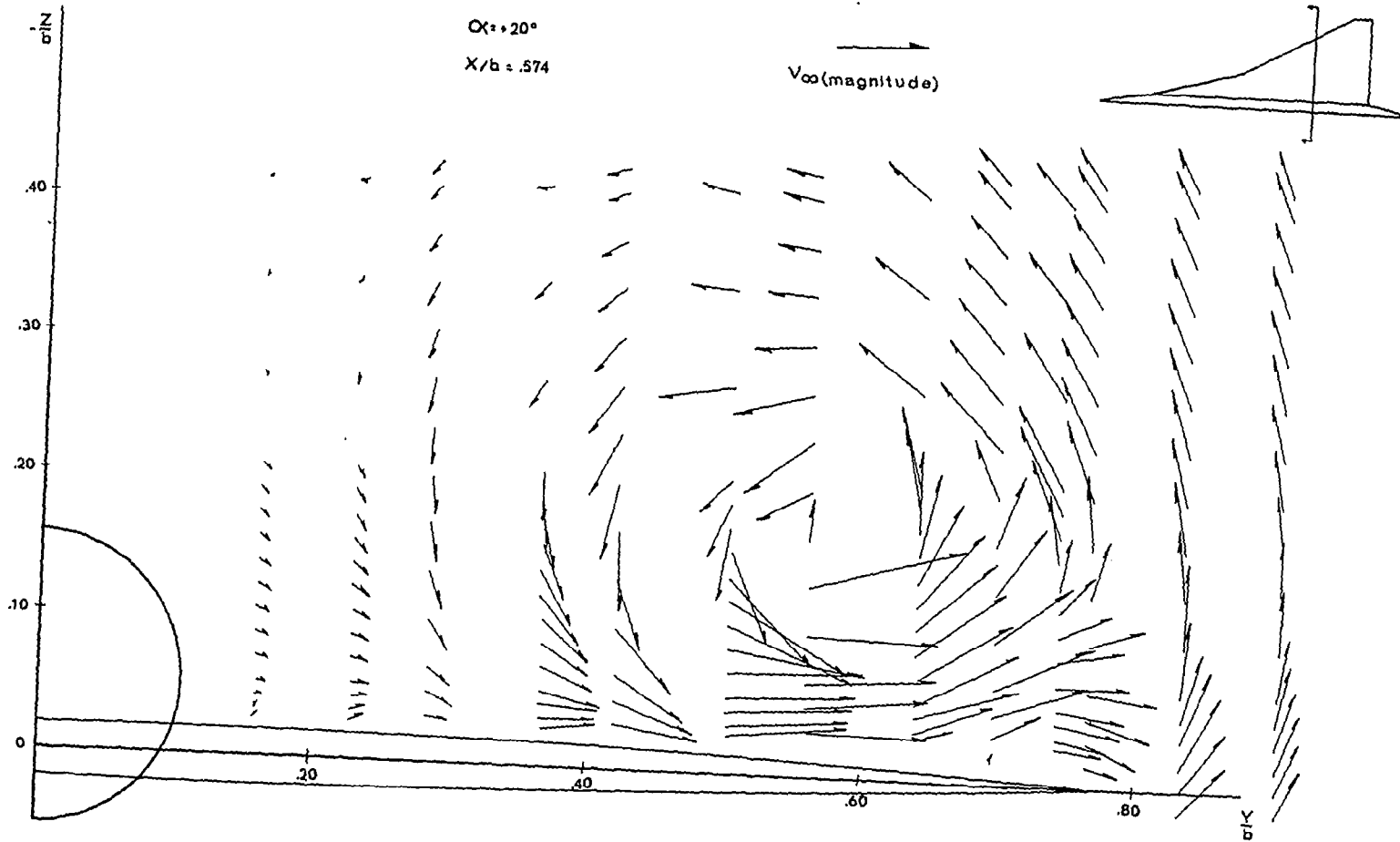


FIGURE 17b- Upper Surface Flow Field - $75^\circ/62^\circ \Delta^2$ - $\alpha = 20^\circ$ $X/b = .574$

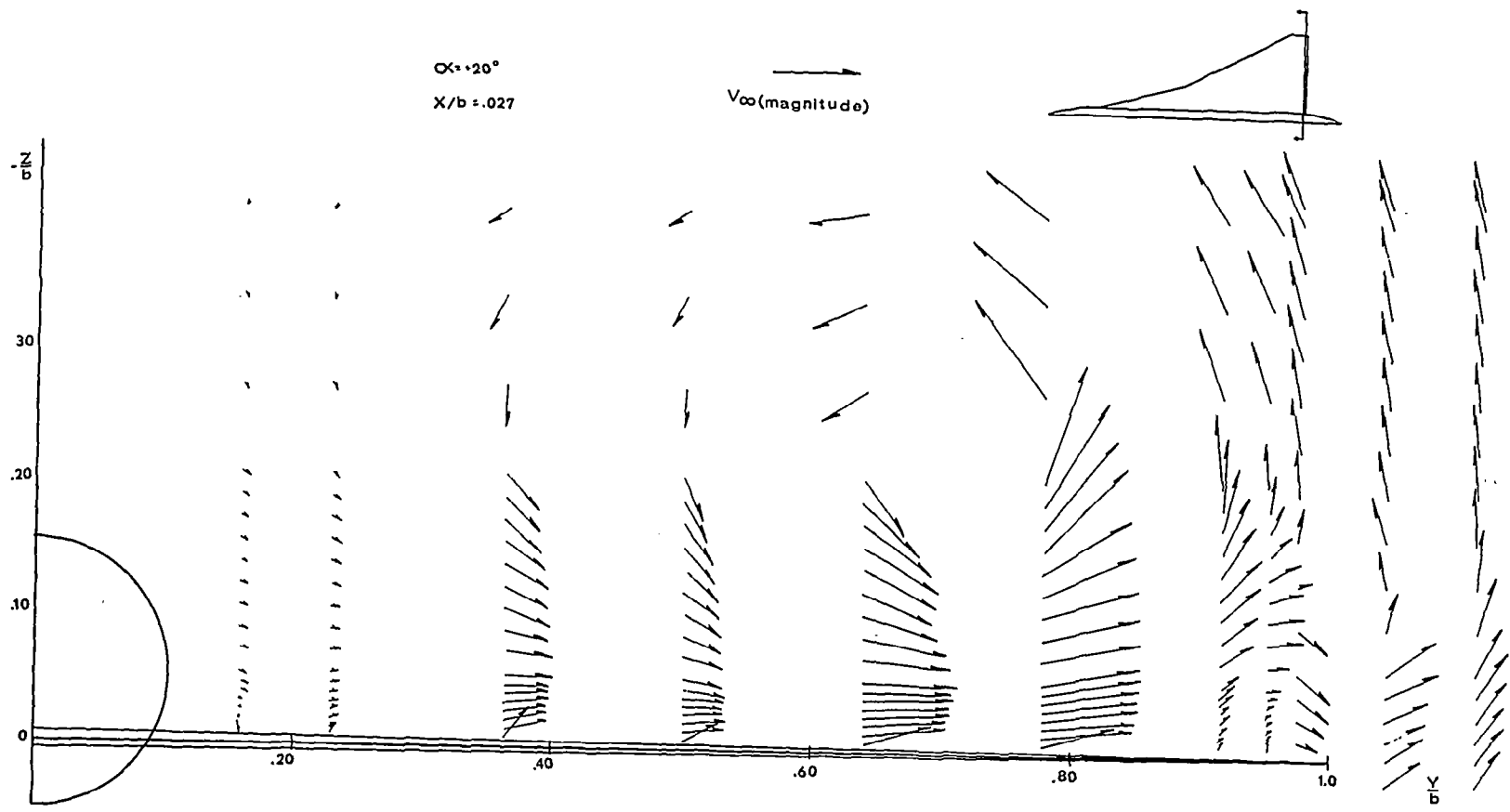


FIGURE 17c - Upper Surface Flow Field - $75.62^\circ \Delta^2$ - $\alpha = 20^\circ$ $X/b = .027$

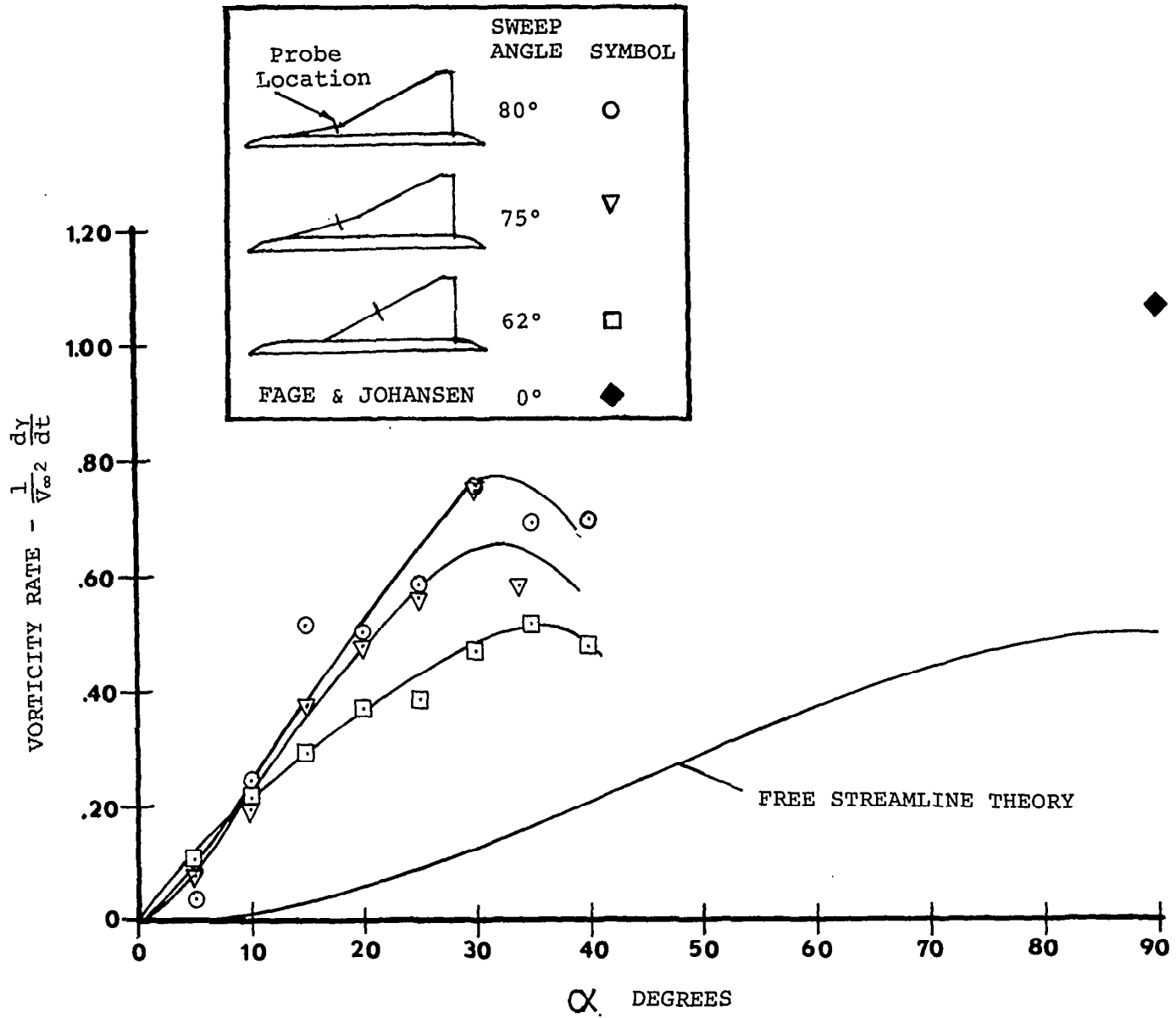


Figure 18 Effect of Sweep Angle on Vortex Sheet Strength

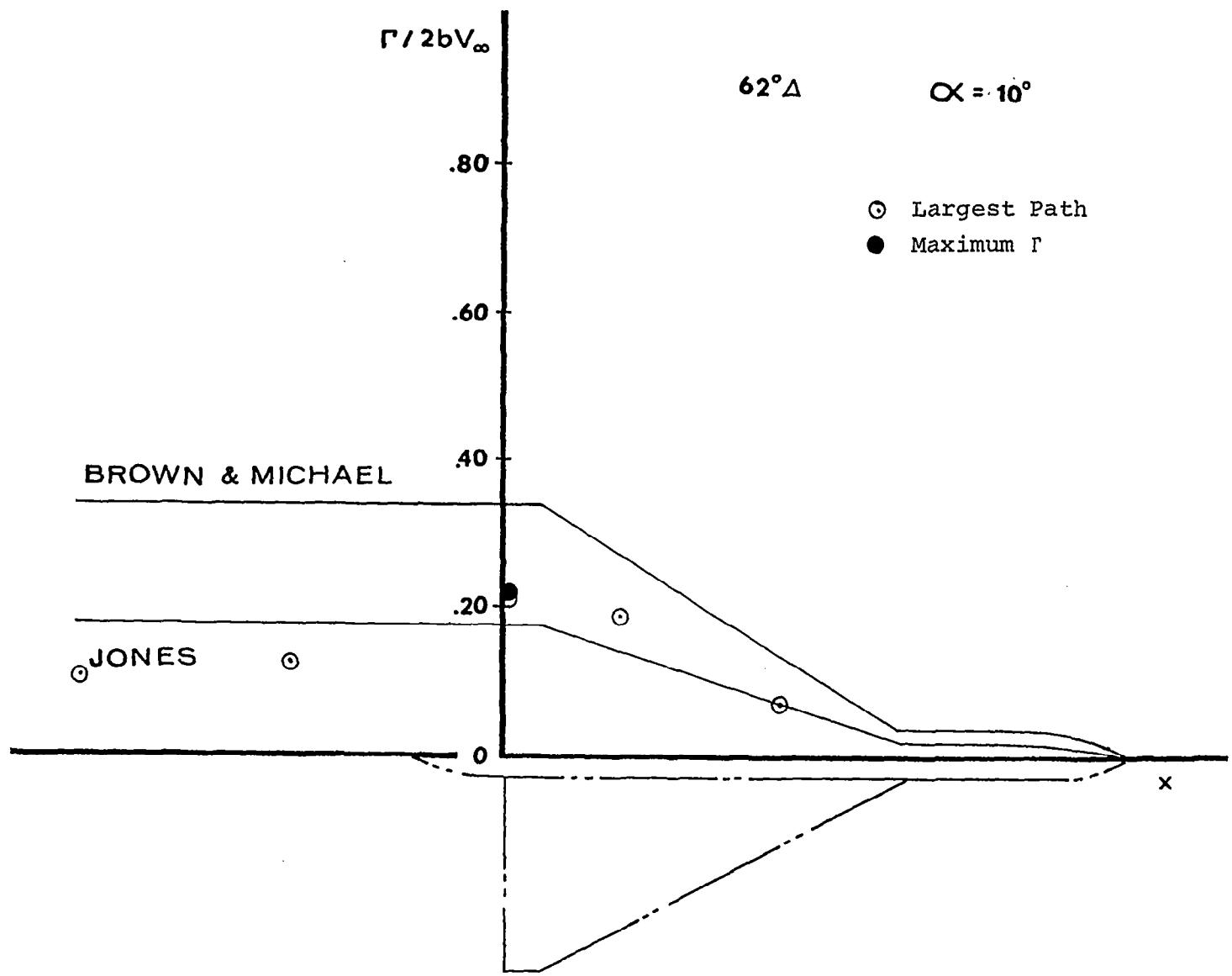


Figure 19a Circulation Integrals 62° Delta Wing, $\alpha = 10^\circ$

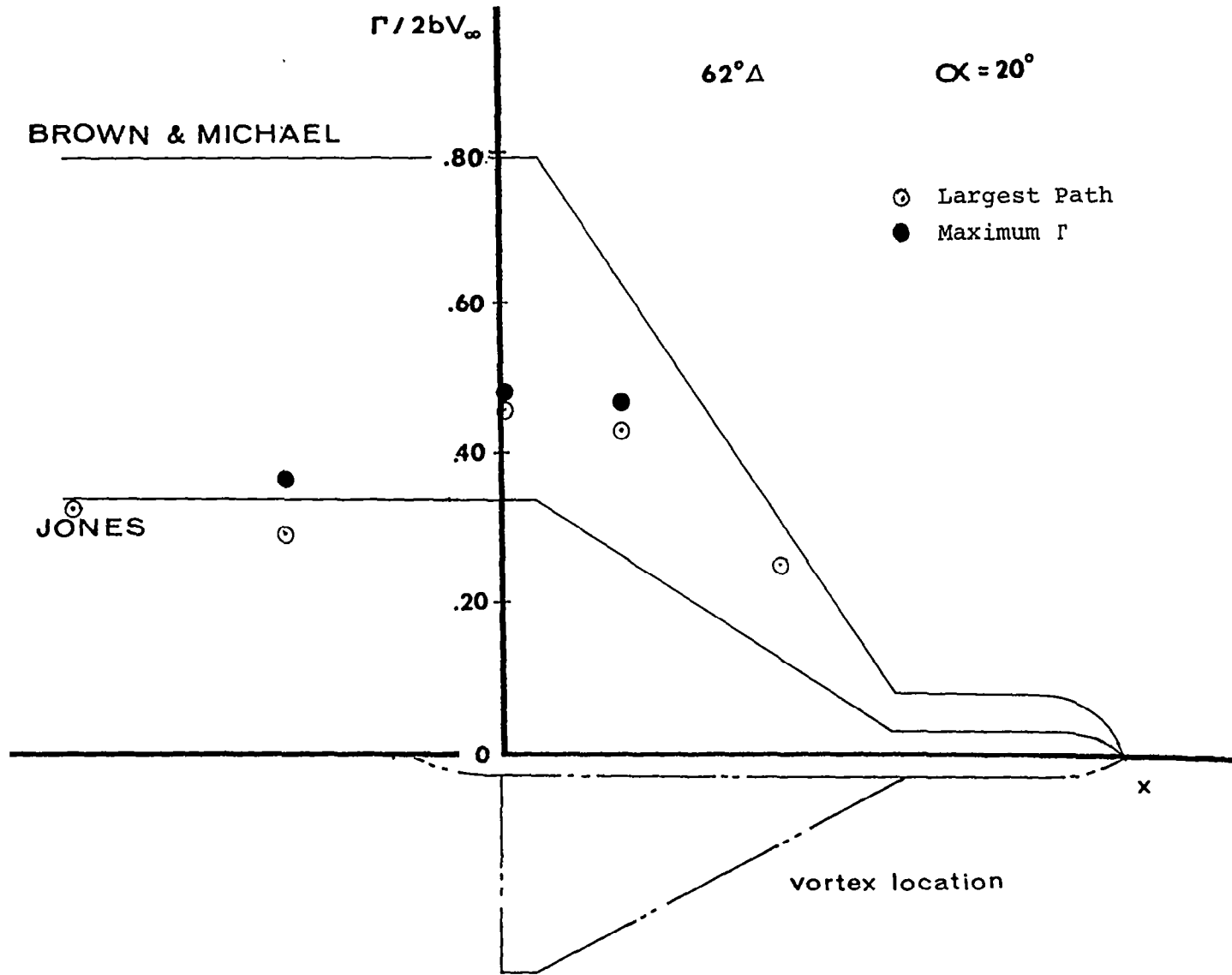


Figure 19b Circulation Integrals 62° Delta Wing, $\alpha = 20^\circ$

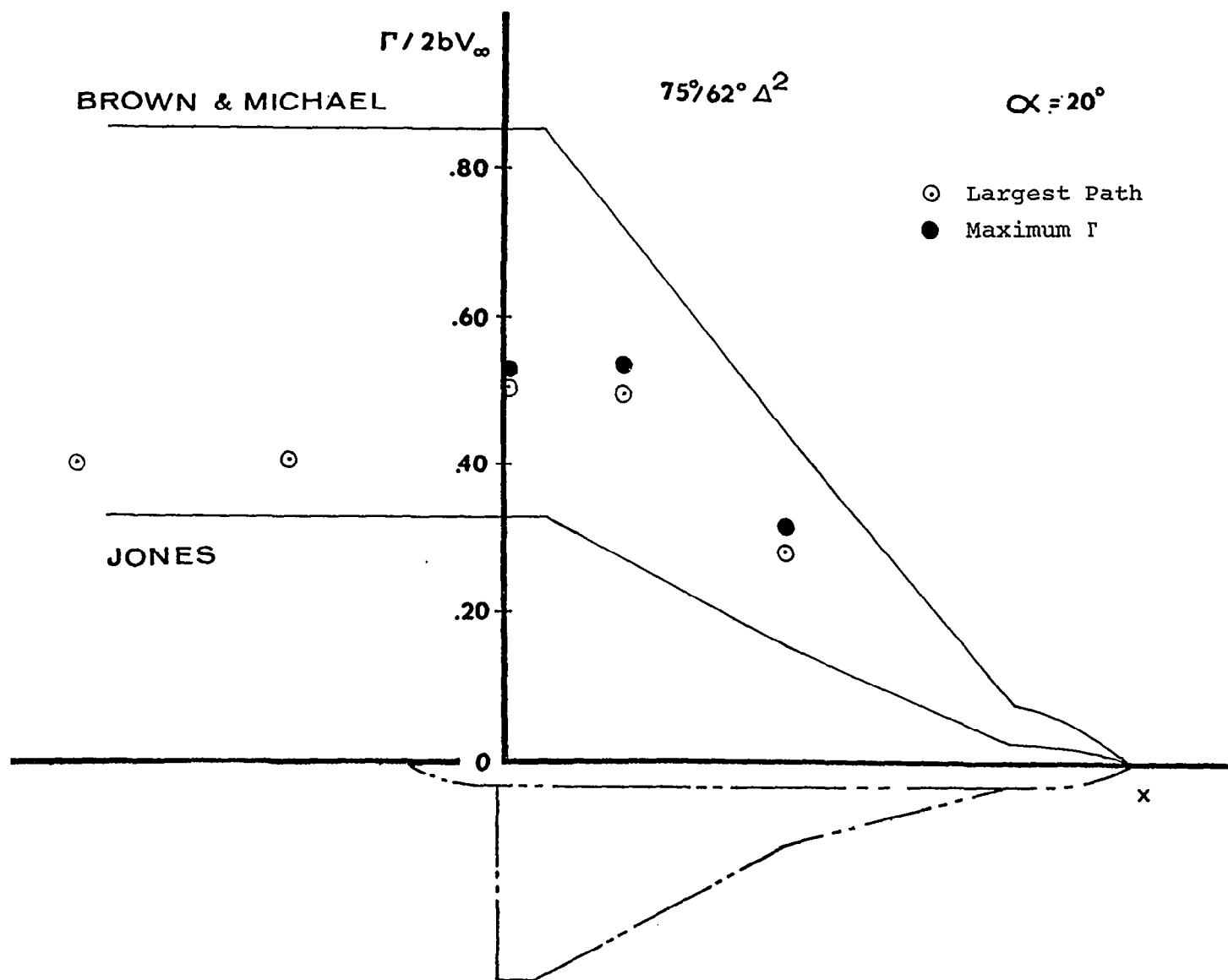


Figure 19c Circulation Integrals $75^\circ/62^\circ$ Double-Delta Wing, $\alpha = 20^\circ$

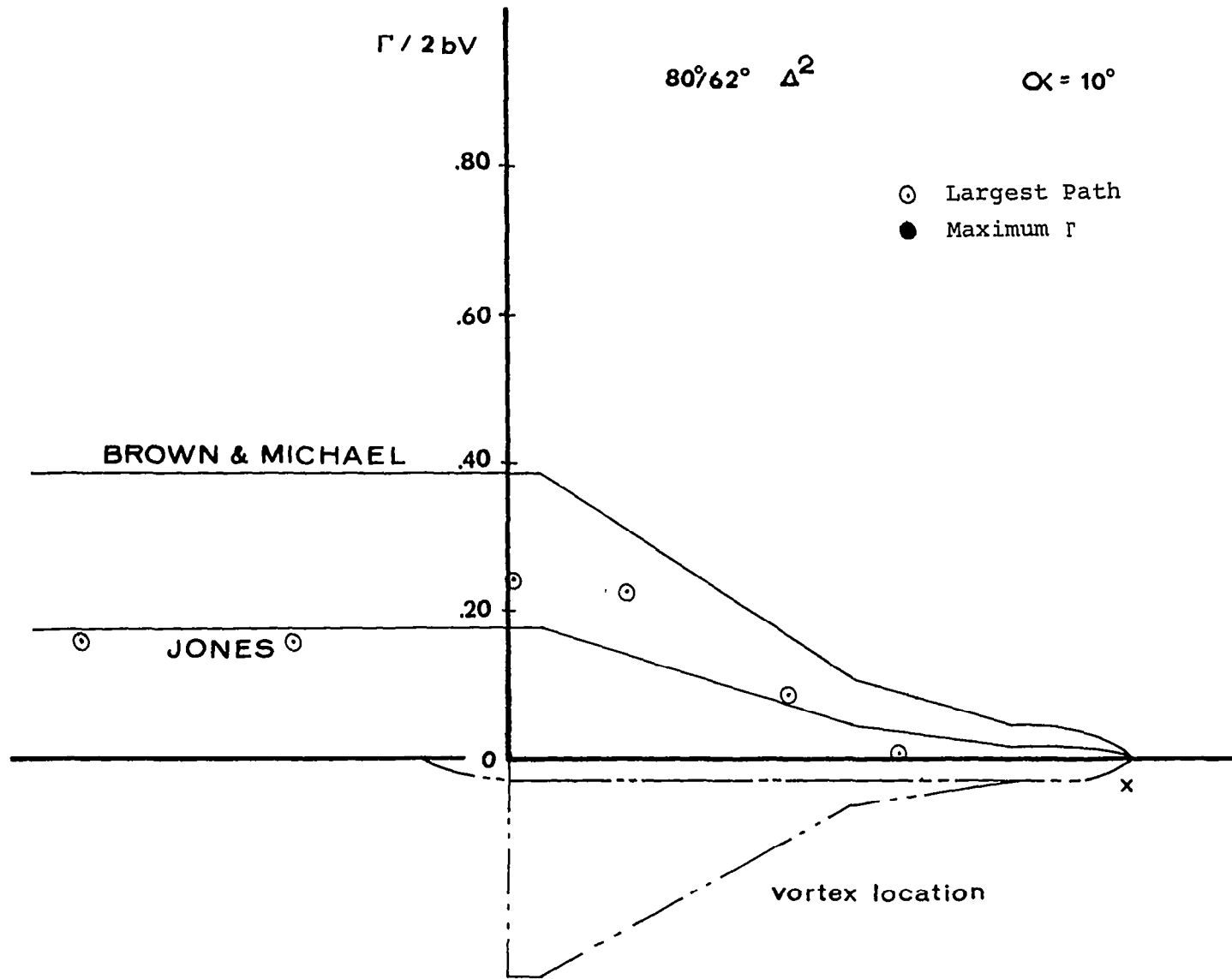


Figure 19d Circulation Integrals $80^\circ/62^\circ$ Double-Delta Wing, $\alpha = 10^\circ$

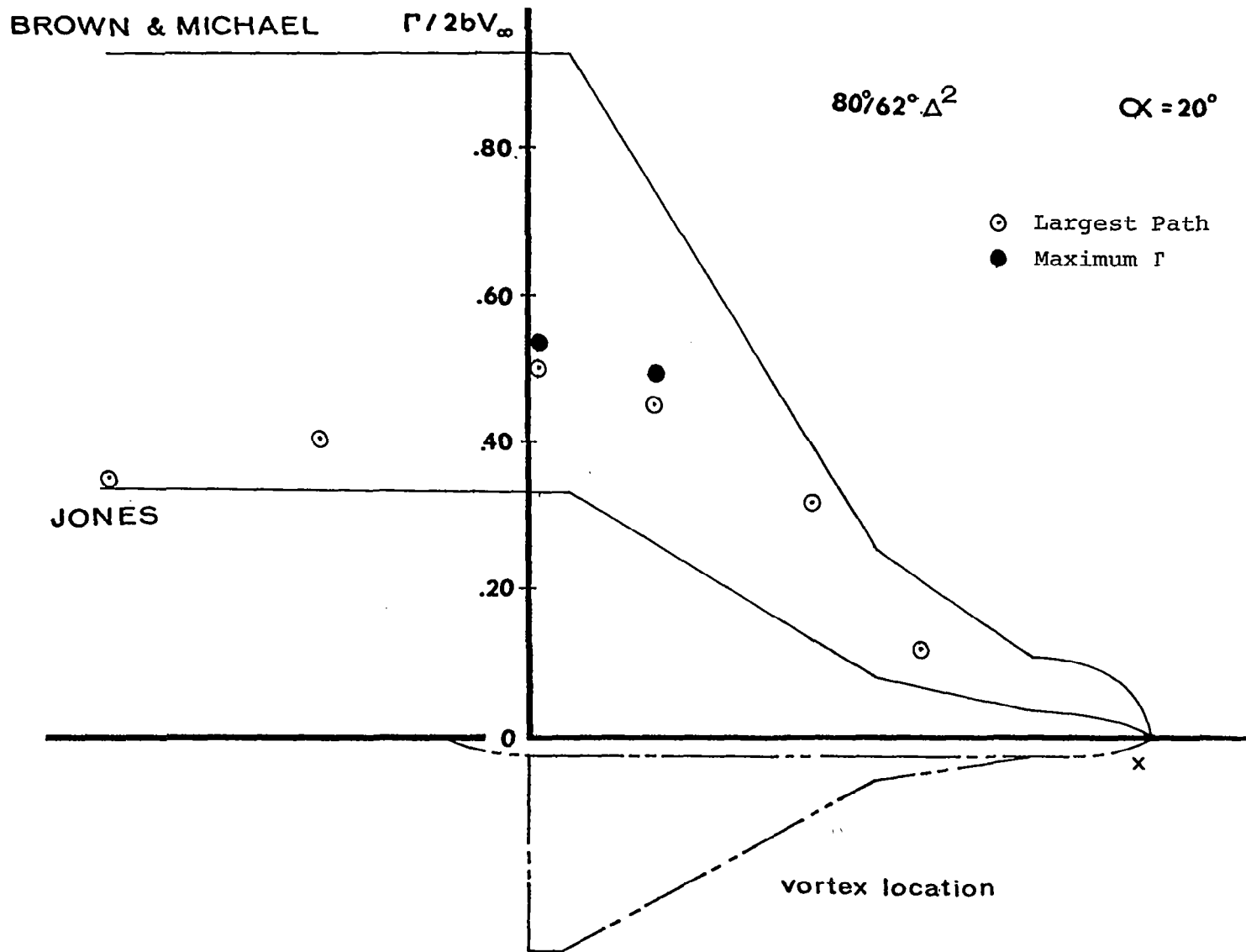


Figure 19e Circulation Integrals 80°/62° Double-Delta Wing, $\alpha = 20^\circ$

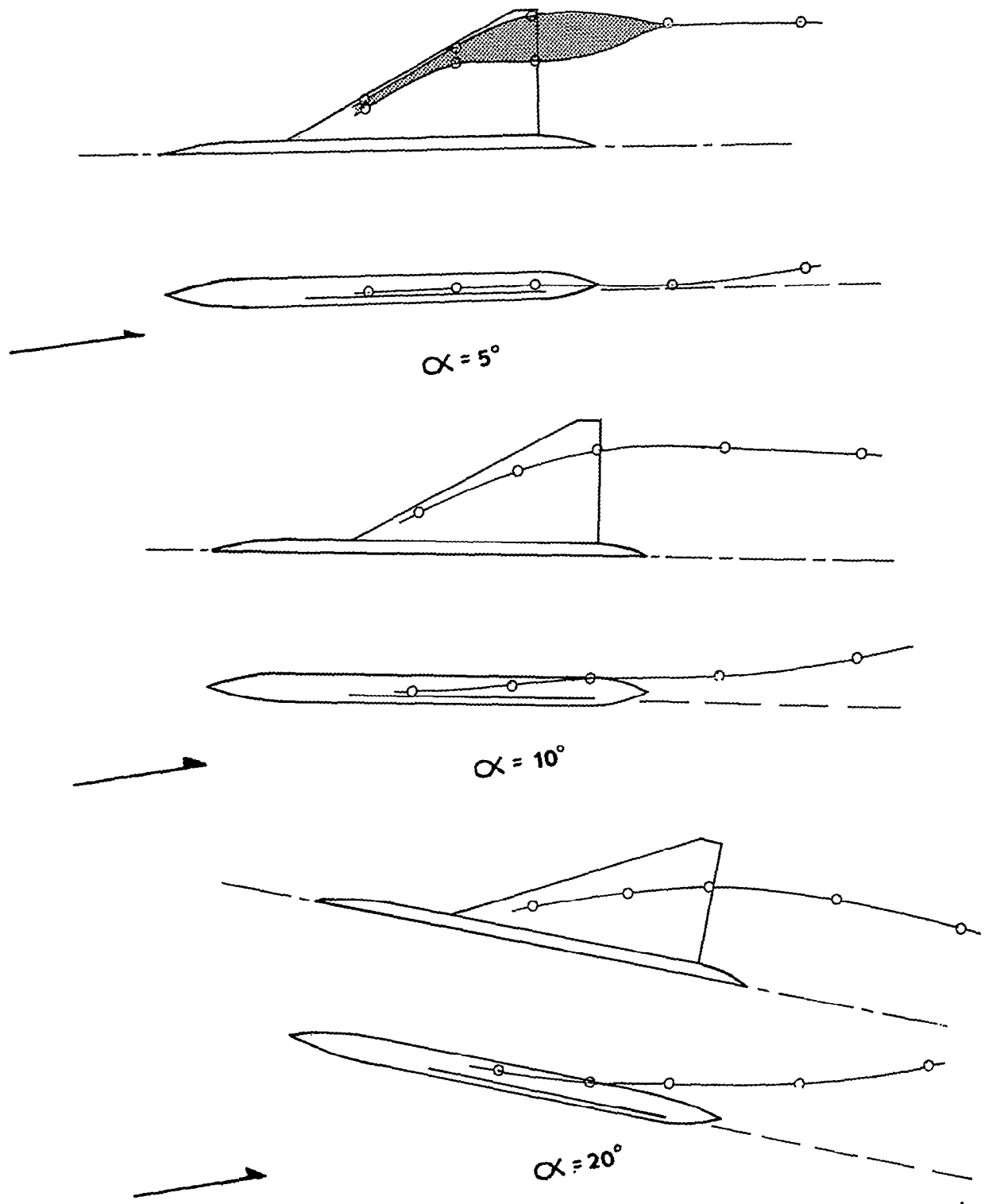


Figure 20a Vortex Core Center Locations 62° Delta Wing

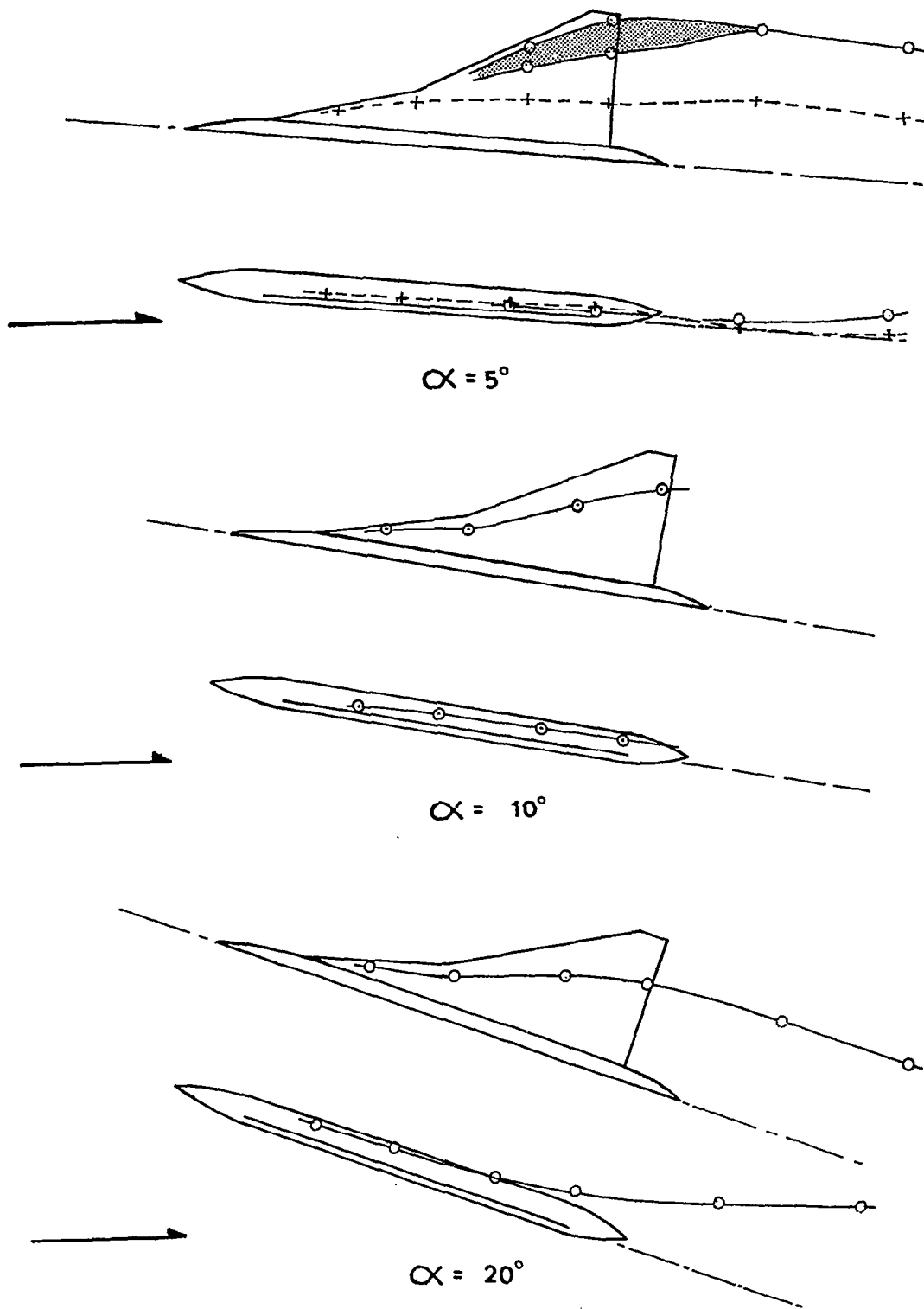


Figure 20b Vortex Core Center Locations 75°/62° Double-Delta Wing

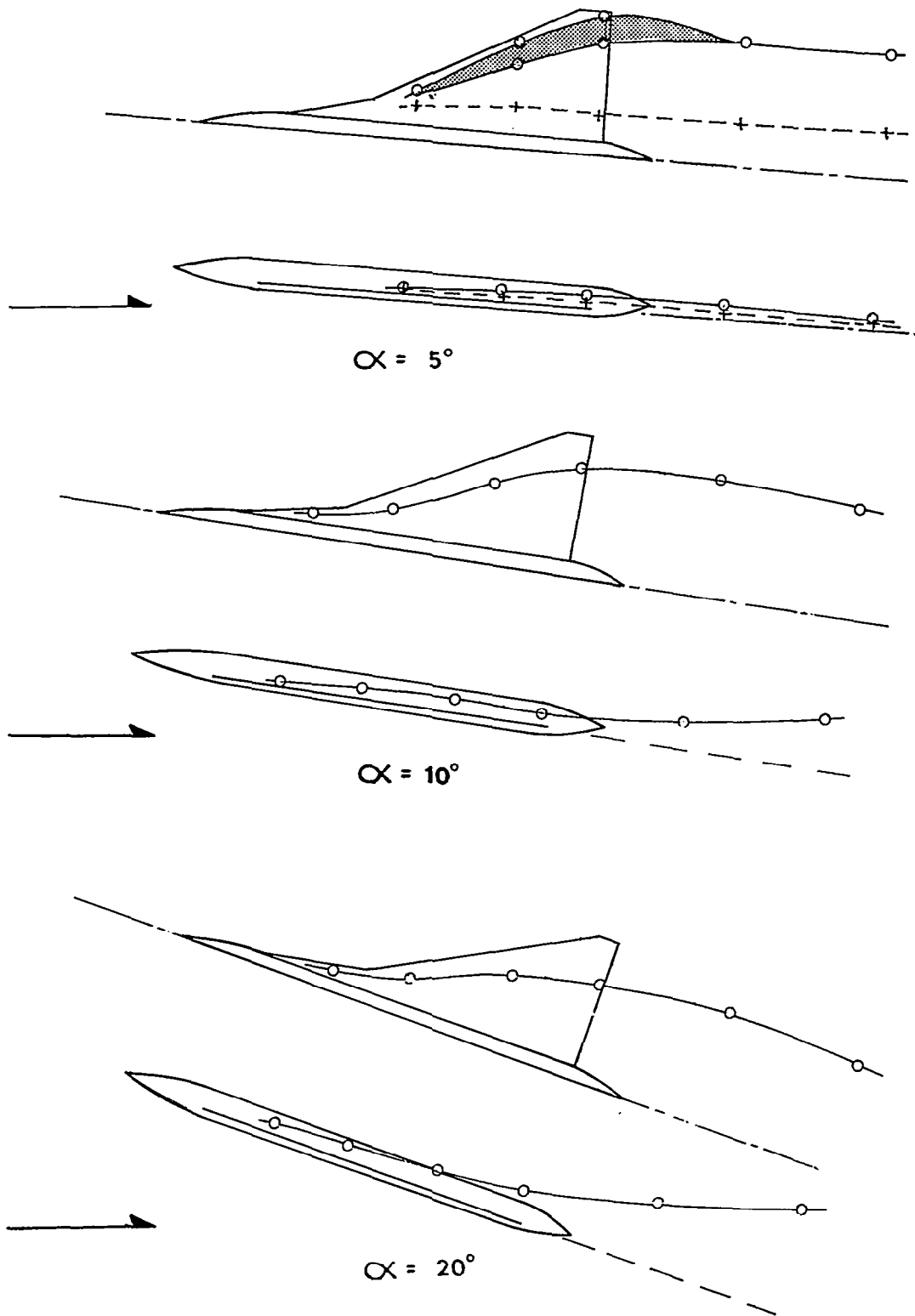


Figure 20c Vortex Core Center Locations 80°/62° Double-Delta Wing

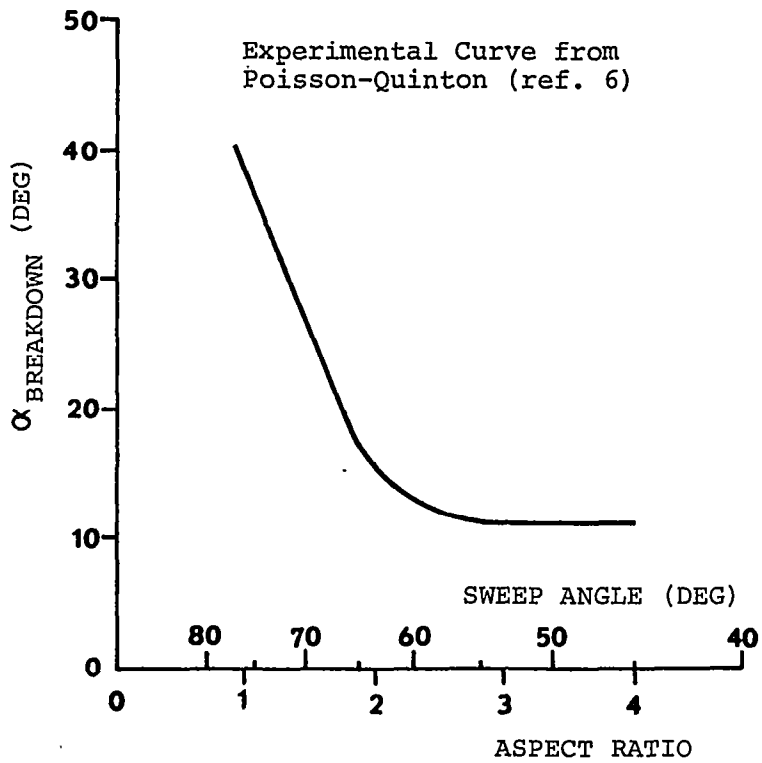


Figure 21 Vortex Core Breakdown Angle

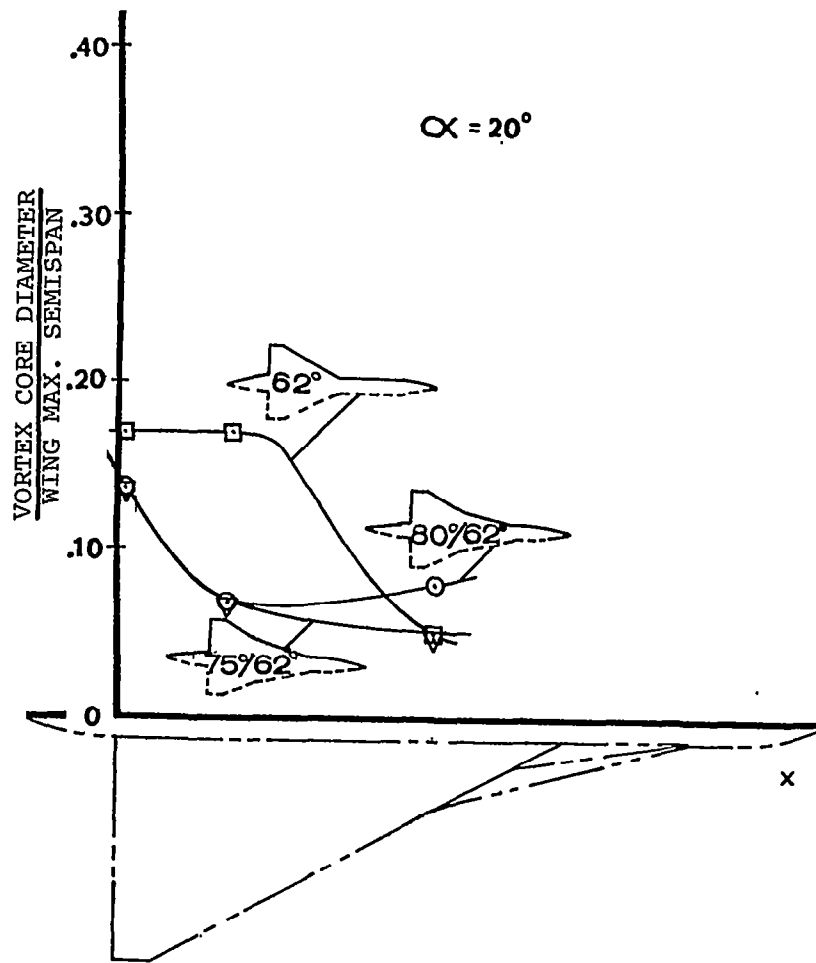


Figure 22 Effect of Strakes on Vortex Core Diameter